Institut für Physikalische und Theoretische Chemie
der Technischen Universität München

Cluster Model Studies of *d*-Metal Species Relevant to Catalysis and of Their Adsorption Complexes

Chan Inntam

Vollständiger Abdruck der von der Fakultät für Chemie der Technischen Universität München zur Erlangung des akademischen Grades eines

Doktors der Naturwissenschaften (Dr. rer. nat.)

genehmigten Dissertation.

Vorsitzende: Univ.-Prof. Dr. Frank H. Köhler

Prüfer der Dissertation:

1. Univ.-Prof. Dr. Notker Rösch
2. Univ.-Prof. Dr. Ulrich K. Heiz

Die Dissertation wurde am 02.11.2005 bei der Technischen Universität München eingereicht und durch die Fakultät für Chemie am 28.11.2005 angenommen.

To my parents and all of my teachers

ฝูงชนกำเนิดคล้าย คลึงกัน
ใหญ่ย่อมเพศผิวพรรณ แผกบ้าง
ความรู้อาจเรียนทัน กันหมด
เว้นแต่ชั่วดีกระด้าง ห่อนแก้ ฤๅไหว

พระราชนิพนธ์ในพระบาทสมเด็จพระจุลจอมเกล้าเจ้าอยู่หัว รัชกาลที่ 5
King Chulalongkorn (RAMA V)

Born men are we all and one,
Brown, black by the sun cultured.
Knowledge can be won alike.
Only the heart differs from man to man.

(Interpretative Translations of Thai Poets
by M.R. Seni Pramoj, 1965)

Acknowledgements

Most of credits in this thesis should justifiably go to my supervisor Prof. Dr. Notker Rösch for giving me an opportunity to study PhD in his group at Technischen Universität München and for his valuable guidance, encouragement and kindness throughout the course of the study. My special thanks are expressed for Dr. Konstantin Neyman and Dr. Sven Krüger who have done massive help during the study here as well as affording a convenient life in Germany.

I also would like to thank Dr. Vladimir Nasluzov, Dr. Ilya Yudanov, Dr. Alexei Shor and Dr. Alexander Voityuk for their valuable advises. I am appreciative to my former supervisors Prof. Dr. S. Hengrasmee, Prof. Dr. J. Limtrakul and Prof. Dr. S. Hannongbua who introduced me into the wonderful field of quantum chemistry.

Particular thanks go to my colleagues; Dr. K. Siriwong, P. Chuichay, A. Genest, F. Schlosser, Dr. A. Woiterski, M. Suzen, M. Girju, Dr. M. Garcia-Hernandez, Dr. L. Moskaleva, Dr. C. Bussai, K.H. Lim, Dr. Z. Chen, Dr. S. Majumder, Dr. R. Deka, A. Deka, S. Bosko, Dr. D. Ganyushin, Dr. A. Matveev, E. Vladimirov, A. Basha, E. Kremleva, S. Ray, E. Shor, H. Alexsandrov, P. Petkov and G. Petrova for the great working atmosphere and for being not only co-worker but also friends. I further wish to thank my friends in Thailand and those who study in Germany for their help and sharing a great time during the study abroad.

I am grateful to the committees who spend their valuable time to evaluate this thesis. Furthermore, the financial support of Deutsche Forschungsgemeinschaft, Volkswagen Foundation, and Fonds der Chemischen Industrie are gratefully acknowledged.

Finally, my absolute acknowledgement is dedicated to my parents, my brothers and sisters for their inspiration and encouragement throughout the entire study.

Contents

List of Abbreviations

AES	Auger electron spectroscopy
AFM	atomic force microscopy
Å	Ångstrom
a.u.	atomic unit
BLYP	Becke-Lee-Yang-Parr
B3LYP	Becke's three-parameter-Lee-Yang-Parr
BP86	Becke-Perdew 1986
BSSE	basis set superposition error
cm^{-1}	wave number
DFT	density functional theory
EPE	elastic polarizable environment
eV	electron Volt
fcc	face-centered cubic
GGA	generalized gradient approximation
HF	Hartree-Fock
HOMO	highest occupied molecular orbital
hcp	hexagonal close-packed
IR(A)S	infrared reflection (absorption) spectroscopy
K	Kelvin
KS	Kohn-Sham

kJ mol^{-1}	kilojoules per mole
LCAO	linear combination of atomice orbitals
LCGTO-FF-DF	linear combination of Gaussian-type orbitals fitting-function density functional
LDA	local density approximation
LEED	low energy electron diffraction
LUMO	lowest unoccupied molecular orbital
MM	molecular mechanics
nm	nanometer
PBEN	Perdew-Burke-Ernzerhof revised by Nørskov *et al*.
PDC	potential derived charges
PES	photoelectron spectroscopy
PW91	Perdew-Wang 1991
pm	picometer
QM	quantum mechanics
RAIRS	reflection absorption infrared spectroscopy
SCF	self-consistent filed
STM	scanning tunneling microscopy
TEM	transmission electron microscopy
TDS	thermal desorption spectroscopy
UHV	ultrahigh vacuum
UPS	ultraviolet photoelectron microscopy
VWN	Vosko-Wilk-Nusair
XPD	X-ray photoelectron diffraction
XPS	X-ray photoelectron spectroscopy
xc	exchange-correlation

Chapter 1

Introduction

Metal/oxide interfaces and oxide-supported metal clusters play an important role in many fields of modern technology. These materials are interesting for diverse reasons, ranging from the beauty of medieval art to industrial applications in heterogeneous catalysis, microelectronics and other technologies [1,2]. In the Middle Ages, beautiful stained glass for the large and colorful windows of Gothic cathedrals has been manufactured based on cluster technology. Their color is caused by finely dispersed silver, copper and gold particles embedded by special fabrication procedures into the glass. Nowadays, oxide-supported metal clusters are widely used in heterogeneous catalysis which is a key phenomenon in many technological fields. Some of the best known examples of applications of metal clusters are in environmental chemistry, energy storage and catalytic conversion of hydrocarbons [3–5]. The catalytic activity and selectivity of oxide-supported metal clusters often depend sensitively on structure parameters, such as particles size and shape, or on chemical parameters, such as the properties of the support or promoter materials. For example, hydrogenation of unsaturated hydrocarbons occurs efficiently on nanoparticles rather than on single-crystals of noble-metal platinum, rhodium and palladium catalysts [6]. A further example is pollution control in the exhaust system of cars, the catalyst of which consists of small metal particles, often platinum or rhodium, deposited on a washcoat made of mainly alumina, ceria and

zirconia [4]. To be active, the metal particles have to be a few nanometers large and also the support has to be prepared properly. Nowadays, one of the important aims of research on oxide surfaces is to develop model catalysts of the next generation including the modified [7] or mixed oxide systems [8] multiple component particles [9,10], poisons [11] and promoters.

Also sensors come to mind as applications of supported metal systems [12–14]; their ability and sensibility to detect chemical species in the gas phase depend largely on the shape and size of the metal particles, the exposure of facets, as well as on the presence of co-adsorbates and contaminates on the oxide support. Magnetic materials used for storing information [15] is another interesting example of technological applications which are based on the fact that in the ferromagnetic state with a given orientation of the magnetic moment the material shows a permanent magnetization if the material exists as nanometer-sized particles. To model new magnetic materials for permanent magnets or high-density recording, one needs to understand the magnetic behavior of nanoparticles. For all these examples, it is clear that, for optimum design of material and processes, one has to understand the microscopic structure of the material and the processes occurring at the surface or the interface between metal particles and their substrate.

From an experimental point of view, the low electrical and thermal conductivity of bulk oxides represent severe problems [16–18]. The insulating character of oxides can restrict or even prevent studies by electron or ion spectroscopy as well as by low-energy electron diffraction (LEED) and scanning tunneling microscopy (STM). However, these difficulties have been overcome by using well ordered ultra-thin oxide films grown on a metallic or semiconducting substrate such as MgO/Mo(100), Al_2O_3/NiAl(110), FeO/Pt(111) and SiO_2/Si(100). These films are thin enough to prevent charging, yet thick enough to exhibit electronic and chemical properties representative for the corresponding bulk oxide. Many recipes have been developed for synthesizing and characterizing ordered oxide films, e.g. MgO, Al_2O_3, SiO_2, NiO, Cr_2O_3, FeO, Fe_3O_4 [18–23]. Most ways of preparation deal with direct oxidation of a metal (or semiconductor) single crystal,

the oxidation of an alloy single crystal or the deposition and oxidation of a metal on an inert substrate single crystal.

Theoretical studies using first principles cluster and periodic slab models allow one to explore the factors that are difficult to control separately under experimental conditions. Such studies provide a complementary means for extending the understanding of metal species supported on oxides [24,25]. Especially small metal clusters on oxides, as elementary building blocks of more extended supported metal systems, are of key importance for unraveling the initial stage of interface formation. Recently, many interesting works have been devoted to the adsorption of single *d*-metal atoms [26–38] and small *d*-metal aggregates M_n (n = 2–4) [27,32,36,39–46]. For instance, theoretical studies of the adsorption of single *d*-metal atoms and their dimers on various defect sites of MgO [29–37] are motivated by experimental evidence for different oxide systems [47–50] that point defects may act as stronger nucleation sites for metal particles. Characterizing the bonding between metal atoms and oxide supports as well as the structure of such surface complexes is a prerequisite for describing larger supported moieties which result form metal nucleation and cluster growth. Particularly important issues are the nature of this interaction and its dependence on the size of the metal particles.

Recently, an advanced computational tool was developed for representing oxide surfaces, e.g. MgO, SiO_2 and Al_2O_3, relying on cluster embedding in an elastic polarizable environment (EPE) [34] or in a covalent elastic polarizable environment (covEPE) [51]. In these sophisticated approaches, the relaxation effect is thoroughly taken into account to afford an accurate description of the adsorption on metal-oxide surfaces. A specially designed quantum mechanical/molecular mechanical (QM/MM) interface ensures a consistent description of the mutual influence of electronic and geometric changes of the QM cluster region and its environment relative to the regular unperturbed surface.

Using this first principles technology, one can successfully elucidate structural and energetic parameters of the interaction of metal moieties on oxide surfaces. To investigate the initial stage of metal clusters supported on oxide surfaces, we studied the adsorption of *d*-metal atoms on terraces of MgO(001). We

also addressed larger clusters (dimers, trimers and tetramers) of Cu, Ag and Au to explore their physical and chemical properties, such as shape, binding energies, dimerization and diffusion properties. We also considered the nature of the metal-support bonding and metal-metal bonding. This is necessary to obtain basic knowledge of how metal particles grow on oxide surfaces. Neutral and singly charged oxygen vacancies (F_s and F_s^+) were modeled to represent defects which have been proposed as preferred adsorption sites on the MgO(001) surface in experimental studies [47–50]. F_s and F_s^+ sites are left on the terraces of the MgO support after removal of an O atom and an O^- anion, respectively.

Oxide-supported metal aggregates in the nanometer range often exhibit high catalytic activity [52,53]. Catalytic reactions such as methanol decomposition on Pd nanoparticles [18,19,54,55] or methanol steam reforming on bimetallic PdZn nanoparticles [56–60] can be mentioned. To elucidate the role of such particles, one needs to employ adequate models. Catalysts of nanometer size have been suggested to be modeled by metal clusters consisting of 55 to 140 metal atoms [55,61,62]. These models have been designed in the form of three-dimensional particles, terminated by low-index surfaces of the bulk metals, and they have been employed to investigate surface properties of transition metal single-crystal and polycrystalline materials. Another important extension of the computational strategy based on nanocluster models has been used in our work for the first time [55], namely reduction of the octahedral symmetry of the model cluster to that of the point group D_{4h}. The demonstrated feasibility of such reduced-symmetry calculations of adsorption complexes on nanosize clusters opens the opportunity to investigate less symmetric adsorbates, more general adsorption sites, and a decreased surface coverage. The capability to treat nanoclusters under reduced symmetry is a crucial prerequisite for modeling chemical reactions on metal catalysts with the present cluster strategy, where in general adsorption complexes have to be modeled without any local symmetry constraint.

The present thesis is organized as follows. Chapter 2 gives a brief overview of the fundamental properties, e.g. structure and morphology, of metal oxide surfaces that have been widely used as supports when preparing metal particles.

Chapter 3 is devoted to the theoretical description of interactions of *d*-metal atoms and small clusters with the MgO(001) surface. This chapter is divided into four sections. Sections 1 and 2 show how 17 metal atoms from groups 6 to 11 of the periodic table (Cr, Mo, W; Mn, Re; Fe, Ru, Os; Co, Rh, Ir; Ni, Pd, Pt; Cu, Ag, Au) interact with regular O^{2-} and oxygen vacancy F_s and F_s^+ sites of MgO(001) terraces. We also characterize core-level energies of adsorbed metal atoms, which can be of help for detecting experimentally M/O^{2-}, M/F_s, and M/F_s^+ structures on MgO(001). Section 3 identifies preferred adsorption sites and adsorption geometries for dimers and trimers of coinage metals Cu, Ag and Au on the defect-free surface MgO(001) and elucidates the role played by the surface defects F_s and F_s^+. Also, the nature of the metal-support bonding is investigated. The results calculated for tetramer species of Cu, Ag and Au, free and supported on regular and defect sites of MgO(001) are reported in Section 4.

Chapter 4 describes adsorption properties of Pd and PdZn nanoparticles and consists of three sections. In Section 1, the results of a theoretical study of C atoms adsorbed on Pd_n (n = 55–146) nanoparticles are discussed. The adsorption energies of C atoms on these cluster models, converged with respect to cluster size, are presented and it is examined which surface sites of these clusters are preferentially occupied by adsorbed C. Afterwards, co-adsorption of CO molecules and C atoms on Pd nanoparticles will be considered. This study is important for understanding the methanol decomposition reaction occurring on well-ordered Pd nanoparticles. Preferred sites of CO molecules in the presence of deposited C atoms are identified. Also, the effect of pre-adsorbed C atoms on geometric and energetic properties of CO molecules is inspected. Section 2 deals with bimetallic cuboctahedral PdZn nanoparticles. Energetic and structural properties of these clusters, such as the cohesive energy and the preferential positions of Zn atoms in PdZn particles, are evaluated. PdZn is an active component of one of the novel efficient catalysts for the steam reforming of methanol and interaction with CO can provide pertinent information on the reactivity of catalyst particles.

Finally, a summary and prospects for future work are presented in Chapter 5.

Chapter 2

Metal Oxide Surfaces as Substrates to Support Metals

Metal particles grown on clean and well-ordered oxide surfaces are widely used as model catalysts. To understand the properties of these catalysts, fundamental knowledge on oxide surfaces and oxide-supported metal particles is required. Therefore, this chapter provides a brief overview of the preparation approaches and characterization techniques applied to metal-oxide substrates and metal particles supported on them. In the following we will focus on oxide substrates in their most relevant forms for the present study, namely single-crystal surfaces and thin films. For studying metal particles deposited on such surfaces, formation of defect sites will be briefly dealt with, as they are commonly considered to play an important role for metal-oxide interactions, especially when the supported metal particles are small, as is the case in the present work. Finally, preparation of deposited metal species and their properties will be discussed.

2.1 Single crystals

This section deals with the preparation and the properties of single-crystal oxide surfaces used as catalyst supports. These substrates have been introduced in the late 1960s with the development of ultrahigh vacuum (UHV) technology. The best

Table 2.1. Single crystal oxide surfaces used as catalyst supports. [a]

Crystal	Preparation	Method	Supported-metal
MgO			
MgO(001)	UHV cleaved	LEED	Ag, Au, Al
MgO(001)	UHV cleaved	RHEED	Cu, Ag, Au, Ni
MgO(001)	UHV cleaved	HAS	Au, Pd
MgO(001), MgO(111)	In situ TEM, Cleavage	TED	Cu, Ag, Au, Pd
MgO(001)	Air cleaved	LEED	Cu
MgO(001)	Air cleaved	LEED	Fe
MgO(001)	Air cleaved	XPS, AES	Ag
MgO(001)	Polished		Pt
ZnO			
ZnO(0001)	UHV cleaved		Au
ZnO(0001)	Air cleaved	LEED	Cu, Pd
$ZnO(10\bar{1}0)$	Air cleaved	LEED	Cu
ZnO(0001)	Polished	LEED	Ni, Pd, Pt
Al_2O_3			
Al_2O_3(0001)	Polished	LEED	Cu
Al_2O_3(0001)	Polished	AES	Pt, Rh
Al_2O_3(0001)	Polished	RHEED, XFD	Rh
TiO_2			
TiO_2(110)	Polished	LEED	Cu, Pd, Fe
TiO_2(110)	Polished	AFM	Ag
TiO_2(110)	Polished	STM	Rh
CeO_2(111)	Polished	RHEED, AES	Rh
ZrO_2(100)	Polished	AES	Rh

[a] Data from Ref. 18 and references therein.

strategy to prepare clean and well-ordered single crystal surfaces is via in situ cleavage [18,63,64] under UHV conditions. Alternatively, cleavage can be performed in air with subsequent cleaning in UHV. However, lower defect densities are achieved if the cleavage is carried out directly under UHV conditions [53].

Generally, the cleavage devices are constituted of a moving chisel in a hard material which is inserted at the corner of a single crystal [65]. This strategy, however, is applicable only to a few oxides, such as MgO, NiO, ZnO and $SrTiO_3$ [66]. Other interesting materials, such as Al_2O_3, SiO_2, TiO_2, etc. are hard to cut properly, as rough surfaces are formed upon cleavage [63]. The preparation and characterization techniques of selected surfaces of conventional metal-oxide substrates are summarized in Table 2.1. There, one can see how the metal oxide surfaces are prepared as well as which methods are used for characterizing such surfaces. Furthermore, some metal species that have been supported on these oxide surfaces are also listed.

One of the most common cleaved surfaces is MgO(001). When it is prepared by the UHV cleavage, low energy electron diffraction (LEED) patterns are very good, with sharp spots [67] but featuring an undesired high reflectivity of 35–40% [68]. In contrast, the same MgO(100) surface cleaved in air shows a reflectivity of only 10–15% after in situ cleaning. Oxide surfaces can be cleaned by outgassing in UHV at 1000 K [68] or under oxygen pressure ($P = 10^{-5}$ Torr) at 1200 K [69]. However, they exhibit surface defects after cleaning, probably vacancies which have been created by reactions with water vapor [70]. Point defects due to the exposure to air, which may act as nucleation centers, could be a serious problem to control the density of supported metal clusters in a model catalyst.

MgO(111) surfaces are prepared with a mechanical cleaver [71]. These surfaces are polar and considerably less stable than MgO(001). Such polar surfaces can be stabilized by reconstruction or hydroxylation [72,73]. At variance, polar ZnO surfaces are apparently stable and not subject to a reconstruction [74,75]. ZnO has been cleaved in UHV or in air along the basal plane (0001) [76,77]. In the case of more covalent oxides where some charge redistribution may take place at the

surfaces [64], that latter can be stabilized differently from the mode observed for more ionic oxides.

Other currently used catalyst supports are alumina, silica and titania. Various oriented surfaces of alumina have been obtained by cutting single crystals of α-Al_2O_3 along different directions, e.g. (0001) [78,79], $(\bar{1}012)$ [80] or $(1\bar{1}02)$ [81]. The cleaved surfaces are chemically polished, i.e. exposed to chemical substances which are able to "repair" damages, and cleaned by annealing in UHV or under oxygen pressure after ion bombardment. Upon annealing at high temperature, alumina surfaces are generally reconstructed, resulting in a very complex surface unit cell. For example, the (0001) surface successively produces $(\sqrt{3}\times\sqrt{3})$R30° and $(3\sqrt{3}\times3\sqrt{3})$R30° structures [82]. Titania surfaces can be obtained by cutting a rutile single crystal along the (110) [83] or (100) [84,85] directions. Similarly to alumina, rutile surfaces are cleaned in UHV by annealing at high temperatures, but they have a tendency to lose oxygen, which leads to reduced surfaces. For instance, the stoichiometric (110) surface, which exhibits a (1×1) structure, in the course of annealing at 1000 K under UHV transforms to the (1×2) structure, which corresponds to the removal of one row of surface oxygen atoms per surface unit cell [86]. However, heating the surface under oxygen pressure restores the stoichiometric surface [85,87].

Table 2.2. Band gaps of bulk single crystal oxide supports.

Crystal	Band gap (eV)	Reference
MgO	7.7	88
Al_2O_3	8.7	89
SiO_2	8.9	89
CaO	6.9	88
SrO	5.3	88
BaO	4.4	88
ZnO	3.4	88
SnO_2	3.6	90

Although cleaved surfaces are widely used, chemical and physical polishing techniques are also employed to prepare single-crystal surfaces of metal oxides, e.g. of MgO and ZnO. To smoothen these surfaces, ion sputtering followed by annealing in UHV or under oxygen pressure at high temperature is applied. However, annealing of MgO surfaces at more than 1200 K causes surface segregation of calcium, which is one of the main impurities in MgO single crystals [91]. From atomic force microscopy (AFM) measurements, a very rough surface with roughness of about 1 nm was reported for the polished and cleaved MgO surfaces after annealing at 1200 K [92]. Also, a better ordered MgO(100) surface with a mean roughness of 0.26 nm was obtained in another AFM experiment performed in UHV at 1273 K [93]. For investigation of ZnO surfaces, scanning tunneling microscopy (STM) is applicable as the band gap of ZnO crystal (3.4 eV) is much smaller than that of MgO crystal (7.7 eV) (see Table 2.2). Polished ZnO(0001) surfaces annealed at 900 K under UHV feature terraces of mean width of 10 nm, separated by steps of atomic height (0.52 nm) [94].

2.2 Thin films

An alternative way to prepare clean well-ordered oxide surfaces is to grow in situ thin epitaxial oxide films in UHV. Such ultra-thin films grown on a metal substrate feature enhanced electron and heat conductivity, and thus have the important advantage that they can be characterized with the standard arsenal of surface science techniques. For instance, thin-film samples allow small heating gradients in the temperature-programmed desorption (TPD) experiments, they can be studied using scanning tunneling microscopy (STM) and simultaneously reflection absorption infrared spectroscopy (RAIRS). Examples of oxides that can be grown epitaxially are presented in Table 2.3.

Thin epitaxial oxide films can be prepared by vacuum evaporation of bulk oxide on clean well-ordered single crystals [95,96]. Evaporation at high temperature with a low deposition rate yields good crystalline and stoichiometric films, such as MgO(111) or ZnO(0001) on cleaved mica [97,98]. However, the films prepared at

Table 2.3. Ordered thin films grown on metal substrates. [a]

System	Preparation	*T* (K)	Thickness (nm)	Supported-metal
MgO				
MgO(001)/LiF/NaCl(100)	Vacuum evap.	573–673	80	Pd
MgO(001)/Fe(100)	Vacuum evap.		0.5–30	
MgO(001)/Mo(100)	Mg + O_2	200–600	0.5–20	Pd, Ni
MgO(111)/Mo(110)	Mg + O_2	300/800	5	Re
MgO(111)/mica(0001)	Vacuum evap.	300–623	0.2–10	Pd
MgO(111)Mg(0001)	Oxidation	300/470	2	
ZnO				
ZnO(0001)/mica(0001)	Vacuum evap.	633	10–60	Pd
ZnO/Au	Sputtering	300	1000	Cu
Al_2O_3				
Al_2O_3/Al(111)	Oxidation	700	0.3–1.2	Ni
Al_2O_3/Al/Pt(111)	Oxidation	300–480	1	Rh
Al_2O_3/Al/Ru(0001)	Oxidation	1000	2	Cu
Al_2O_3/Al/Si(111)	Oxidation	300	3	Pt
Al_2O_3/NiAl(110)	Oxidation	550/1200	0.5	Pd, Pt, Rh
Al_2O_3/Mo(110)	Al + O_2	90–1200	0.8–5	Cu, Ni, Fe
TiO_2				
TiO_2/Ti/Pt(111)	Oxidation	873	0.5–1	
TiO_2/Ti(0001)	Oxidation	400/755	30	Pt, Rh
TiO_2/Mo(100)	Ti + O_2		0.5	Au
SiO_2				
SiO_2/Si(111)	Oxidation	1273	50–100	Pt, Ir, Rh
SiO_2/Mo(110)	Si + O_2	373	5–10	Cu, Pd, Ni
NiO				
NiO(100)/Mo(100)	Ni + O_2	300	4	
NiO(111)/Ni(111)	Oxidation	570–650	1–2	
CeO_2/Al_2O_3(0001)	Pyrolysis	650	10000	Pd, Pt, Rh

[a] Data from Ref. 18 and references therein.

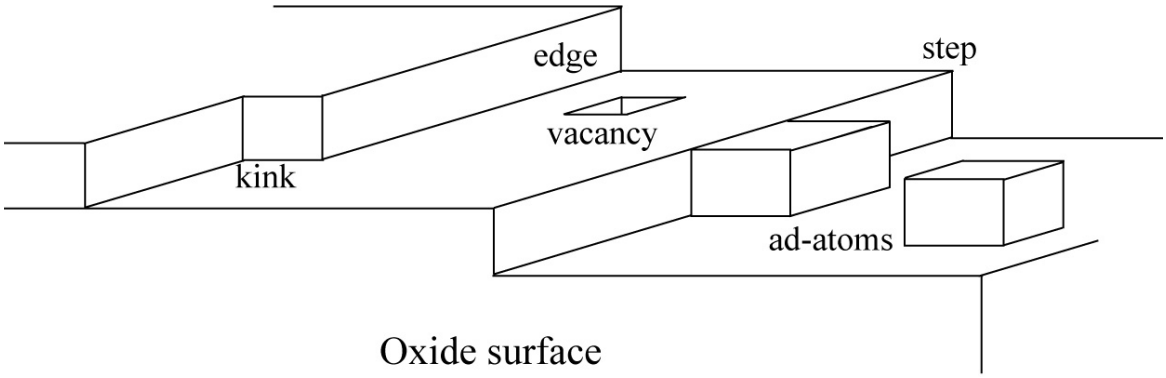

Figure 2.1. Regular sites and various defects on an oxide surface: kink, edge, step, vacancy and ad-atoms.

low temperature are highly non-stoichiometric and unstable upon annealing [99]. The oxide films can be removed from the substrates by interfacial dissolution in water or in acidic solution. These oxide thin films are well ordered, but they exhibit a large number of point defects, as revealed, for instance, by nucleation of noble metals [100].

Another possibility for preparing epitaxial oxide films is to evaporate the metals at a residual pressure of oxygen (10^{-7}–10^{-6} Torr) between 200 and 600 K, followed by annealing at high temperature, 600–1300 K. This method has been applied to various oxides, e.g. MgO(001) [101] and NiO(001) [102]. These films show very good crystallinity and their stoichiometry is nearly perfect, but they often contain a large number of defects. STM investigations of such MgO films grown on Mo(100) have shown a large surface roughness of 6 nm and small (2–6 nm) single-crystal grains [103]. Al_2O_3, TiO_2 and SiO_2 films prepared by this method are less ordered than those of other oxides, such as MgO and NiO.

The third method to produce epitaxial thin films is to oxidize a metal single crystal or alloy. Oxidation of Al(111), NiAl(110), Mg(0001), Ti(0001) and Zn(0001 is performed between 500–700 K under a base pressure of oxygen (10^{-7}-10^{-6} Torr) or by adsorption of oxygen and subsequent annealing under UHV at 600–1200 K. This method has been successfully used for Al_2O_3/Al(111) [104], Al_2O_3/NiAl(110) [105], MgO/Mg(0001) [106], etc. The ultra-thin films of oxides prepared in such a way (up to 10 layers) are well ordered, but not very stable with respect to heating

because of metal diffusion inside the oxide [107]. However, this limitation can be counteracted by increasing the thickness of the oxide films.

2.3 Defects on metal-oxide surfaces

Essentially any real crystal surface contains a large number of defects, no matter how perfect the bulk crystal is, how well it is cleaved or how carefully it is prepared [63]. Several types of the most common surface defects are sketched in Figure 2.1: steps, edges, kinks, ad-atoms and vacancies. For many processes on oxide surfaces, such as chemisorption, catalysis and corrosion, point defects (cation and anion vacancies, ad-atoms) are of particular importance. Among them, oxygen vacancies, which are supposed to be prevalent in many oxides [108], constitute one of the most interesting type of defects. Depending on the material, the structures and properties of oxygen vacancies can differ substantially, so that one even could say that oxygen vacancies may serve as fingerprint of the oxide. For example, on MgO surfaces, which are in the focus of the present work, lack of a neutral O atom results in two trapped electrons, localized in the cavity left behind this O species; it is called an F_s center. In turn, removal of O^- or O^{2-} anions from the surface would result in the formation of F_s^+ or F_s^{2+} centers, respectively. These F_s^{n+} defects in MgO induce low-lying electronic states which give rise to typical excitations in the visible region of the spectrum. This makes MgO samples with such defects colored and is the reason why these centers are labeled by the letter F, from the German word “Farbe” – color.

On polycrystalline MgO surfaces, the formation of oxygen vacancies was proposed to take place by the removal of water molecule at the last stages of dehydroxylation at high temperature [109]. Theoretical studies were performed to investigate the formation energy of oxygen vacancies on MgO surface [110,111]. Removal of a neutral oxygen atom from the surface was calculated to require 7.2–7.7 eV depending on the cluster model used. These energies are of the same order as those obtained for NiO(100) surface, 6.5 eV, by means of complete active space SCF, CASSCF, calculation [112]. The formation energy of F_s^+ centers on

MgO(001) terraces was theoretically estimated at 11–12 eV and that of F_s^{2+} ones at ~23 eV [110]. The defect formation at the edges of MgO was reported to be 1–2 eV lower than at the (001) terraces [110] as low-coordinated O anions are more weakly bound to the crystal than those on the terraces.

Oxygen vacancies are supposed to be the sites crucial for the nucleation of supported metals [18,36,108,113,114] and thus expected to play an important role in tuning the activity of deposited metal particles, especially the smallest among them.

2.4 Nucleation and growth of metal particles

Once the oxide support has been characterized, the next step in the development of a model catalyst is the preparation of active metal particles. In most cases, the latter are metal aggregates in the (sub)nanometer size range. Thus, this section deals with the preparation, structure and morphology of metal particles on thin oxide films.

2.4.1 Deposition of metal particles on metal oxide surfaces

The experimental procedure should provide a maximum control of the preparation conditions and should be applicable to a broad range of materials. However, there is no universal preparation method. The method is chosen by the specific structure feature to be investigated. The most common approach is based on metal vapor deposition. Among the advantages of the physical vapor deposition (PVD) technique [1,18,23], which is a coating process that involves evaporation and deposition of a material, are its applicability to most of materials, the cleanliness of the samples, and the broad range of particle sizes that can be formed. However, the samples prepared in such a way are characterized by a rather broad distribution of particle sizes, instead of a mono-dispersed system which is usually desired [53]. Moreover, the positions of particles on the surface and distances between them can not be controlled externally because they depend on the distribution of surface defects on the support.

To circumvent these problems, chemical vapor deposition (CVD) has been suggested [115,116]. This approach includes the preparation of metal complexes

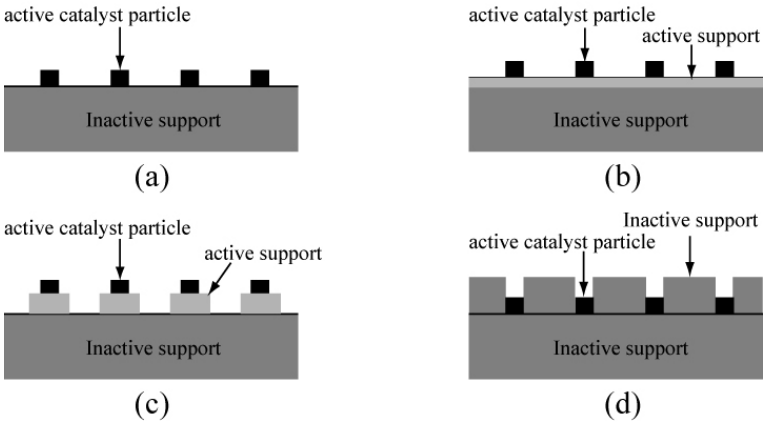

Figure 2.2. Schematic representation of different possible EBL-nanofabricated structures. The active particles can be deposited on: (a) an inactive support; (b) an active support; (c) disks of active support; (d) in wells (to simulate pore diffusion). Adapted from Ref. [121].

(and cluster compounds) with well-defined stoichiometry and sufficiently high vapor pressure, which can be deposited on the surface from the gas phase. One of the disadvantages of CVD is its applicability only to rather limited kinds of materials. Furthermore, the insufficient (and hard to control) stability of the metal framework after stripping of the ligands may cause a problem as well as the lack of control over the distribution of metal particles on the surfaces. Finally, incomplete removal of the ligand shells can result in contaminations.

To avoid contaminations of this nature a method to deposit free metal clusters from the gas phase has been proposed [117,118]. The metal aggregates are mass-selected (of definite size) and subsequently soft-landed on the surface. This allows to control the size of the supported particles in atom-by-atom fashion. The remaining drawback is that the distribution of the particles is probably still governed by the nucleation at defect sites which is difficult to control directly or to tune efficiently. As a result, the distribution of distances between the supported metal particles is usually not well-defined.

Recently, a promising approach aiming at the simultaneous control of the particle sizes and distances between them has been reported [119–121]. Even the individual position of each particle can be controlled by using lithographic preparation methods such as colloidal lithography [119] or electron beam

lithography (EBL) [120,121]. However, the latter method has the tendency to result in contaminated samples which are not prepared under UHV; furthermore, the method is not applicable to very small particles. Possible structures of model catalysts prepared by EBL are shown in Figure 2.2.

2.4.2 Nucleation and growth of metals on oxide surfaces

To study the nucleation and growth of metal particles on metal oxide surfaces, knowledge of processes taking place on the surface is necessary. When the metal atoms from the vapor phase are deposited on the oxide surfaces, they can stick to it, diffuse on the surface or re-evaporate, – depending on the strength of the interaction with the surfaces, of the kinetic energy of the incoming species and of the amount of thermal energy in the system.

In the first stage of adsorption, not all metal atoms stick to the surface. They will be trapped on the surface if they get thermally accommodated to it. A sticking coefficient smaller than one means that desorption takes place and thus the surface is incompletely covered. This situation is more relevant for elevated surface temperatures. At room temperature, however, the sticking coefficient is already close to one for many transition metal atoms and small aggregates on oxide supports [122].

Once adsorption has taken place, diffusion of metal atoms across the surface has to be considered. The rate of this step depends on the diffusion coefficient [122]:

$$D = \frac{1}{4}\left(\nu_0 a^2\right)\exp(-\varepsilon_{Diff} / kT), \tag{2.1}$$

where ε_{Diff} is the activation energy for diffusion, ν_0 is the pre-factor, a is the distance between two adjacent adsorption sites, T is the temperature and k is the Boltzmann constant. If defects sites are present on the surface, ad-atoms may be trapped at these sites. Subsequently, growth processes, such as homogenous nucleation (metal nucleation on a regular site) or heterogeneous nucleation (nucleation at a defect), can occur by adding further ad-atoms [16]. In the case of

homogenous nucleation, the saturation density of nuclei *N* depends on the diffusion coefficient *D* and the vapor flux which describes the deposition rate, *F* [123]:

$$N \sim (F / D)^{i/(i+2)}. \tag{2.2}$$

Here *i* is the critical cluster size [124] which indicates the maximum number of ad-atoms formed on the surface before the island growing. For heterogeneous nucleation, the saturation density is independent of flux, diffusion coefficient and temperature. Saturation in the density, *N*, of the nuclei is reached when the probability for creating new nuclei becomes negligible compared to that for adding to existing nuclei. This occurs when an ad-atom can diffuse to an existing cluster faster than it can find an ad-atom with which to nucleate. This kind of nucleation takes place when the attraction between ad-atoms and defect sites is strong and the density of defects is high, i.e. the distance between defects is less than the distance *L* between islands expected for homogeneous nucleation, $L = (1/N)^{1/2}$ [18,125].

After the saturation density of supported particles has been reached, no further nuclei are formed and all diffusing ad-atoms are captured by existing islands. Thus, only growth processes can take place by forming either two- or three-dimensional shapes. From the point of view of thermodynamics, the equilibrium shape of metal particles can be described with the help of surface free energies of the metal, γ_{Metal}, the oxide, γ_{Oxide}, and the free energy of the metal-oxide interface, $\gamma_{Interface}$, [124,126,127]. When

$$\gamma_{Interface} + \gamma_{Metal} \leq \gamma_{Oxide}, \tag{2.3}$$

the metal wets the oxide at equilibrium, corresponding to a two-dimensional layer-by-layer growth mode, i.e. to *Frank-van-der-Merwe* growth. Alternatively, when the sum of $\gamma_{Interface}$ and γ_{Metal} is larger than γ_{Oxide}, wetting on oxide is thermodynamically forbidden. Three-dimensional islands of metal are supposed to be obtained, i.e. the growth mode is according to either *Stranski-Krastanov* (S-K) or *Volmer-Weber* (V-W).

Stranski-Krastanov growth takes place when several monolayers are grown in layer-by-layer fashion before a three-dimensional island is grown. In *Volmer-*

Weber mode, three-dimensional growth occurs immediately without first forming a monolayer. The surface energies of metals (especially of transition metals) are usually larger than those of oxides [123,128]. Thus, the growth of three-dimensional particles is most likely, which has indeed been reported in the many studies of metals on oxides [18,123,129–131]. In the case of a *Volmer-Weber* growth mode, the equilibrium shape of the aggregates can also be predicted. As shown in Figure 2.3, it is a *Wulff polyhedron* truncated at the interface in accordance with the following equations [18,132]:

$$\Delta h / h_i = E_{adh} / \gamma_{Metal_i}, \tag{2.4}$$

and

$$E_{adh} = \gamma_{Metal_i} + \gamma_{Oxide} - \gamma_{Interface}, \tag{2.5}$$

where γ_{Metal_i} is the surface free energy of the corresponding crystal surface *i* and E_{adh} is the adhesion energy.

From equation (2.4), the particles become flatter when the adhesion energy increases. As one can see from equation (2.5), the adhesion energy depends on the metal-oxide interaction. If this interaction increases, for example by partial oxidation, $\gamma_{Interface}$ will decrease and E_{adh} will increase. Table 2.4 illustrates experimental and theoretical studies of the interaction of metals on single crystal surfaces of metal oxides.

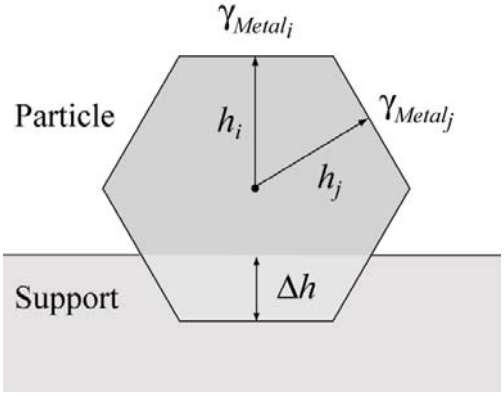

Figure 2.3. Schematic representation of the *Wulff-Kaichew* construction, adapted from Ref. 18.

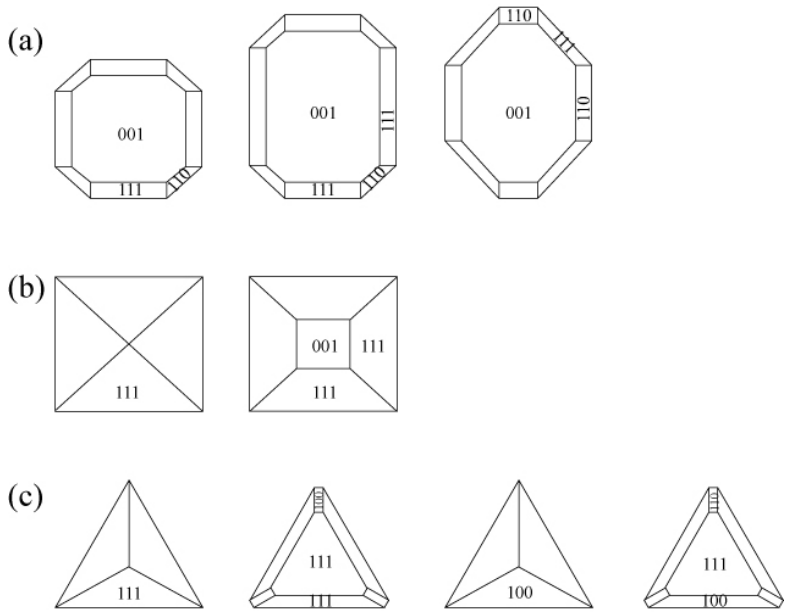

Figure 2.4. Schematic representation of various shapes of fcc metal particles obtained by epitaxial growth: (a) in the (100) orientation at medium temperature; (b) in the (100) orientation at high temperature; (c) in the (111) orientation at medium temperature. Adapted from Ref. [18].

For a particle of nanometer size, the presence of edges and corners can not be neglected. They represent lower atomic coordination modes (i.e. higher local surface energy) and can notably affect the equilibrium shape of the particle. From the temperature evolution of the surface energy anisotropy, therefore, less round shapes of particles are expected. When metal clusters are prepared at high temperature, only regular polyhedra are obtained [133,134].For example, the favored face-centered cubic (fcc) structures, grown at high temperature on oxide or graphite substrate, have polyhedral shapes exposing (111), (100) and (110) facets [135]. Figure 2.4 shows the main shapes of supported metal particles observed on model catalysts.

Table 2.4. Metals on single crystal oxide surfaces. [a]

Oxide	Oxide face	Metal	Sureface Preparation	Growth mode
MgO	001	Ni	Air cleaved and annealed	S-K, epitaxial
	001		Polished and annealed	Epitaxial (100)
	001	Pd	UHV and air cleaved	V-W, epitaxial Pd (100)
	001		Air cleaved and annealed	S-K, epitaxial
	001	Pt	Air cleaved and annealed	S-K, epitaxial
	001	Cu	UHV cleaved	Epitaxial Cu(100)
	001		Polished and annealed	Epitaxial Cu(100), S-K
	111		Polished and annealed	Epitaxial Cu(111), S-K
	001	Ag	UHV cleaved	Epitaxial Ag(100)
			Air cleaved	V-W, random orientation
			Air cleaved and annealed	S-K, epitaxial
	001	Au	UHV cleaved	Epitaxial Au(100), polycrystalline
			Air cleaved	Random crystalline oriented
			Air cleaved and annealed	S-K, epitaxial
Al_2O_3	0001	Rh	Polished and annealed	V-W, weak interaction
	0001	Ni	Polished and annealed	Weak interaction at RT
	Cluster		Theory	Ionic bond, Covalent Ni 3d-nonbonding O 2p bond
	$10\bar{1}2$	Pd	Polished and annealed, high temperature	Diffusion into subsurface, then epitaxial (110) or (111)
	0001	Pt	Polished and annealed	V-W, weak interaction
	0001	Cu	Polished and annealed	S-K, V-W
	Cluster	Ag	Theory	Covalent Ag 4d-nonbonding O 2p bond
ZnO	$10\bar{1}0$	Al	Polished and annealed	Strong interaction, forms Al oxide
	$0001, 000\bar{1}$	Ni	Polished and annealed	Layer, stronger on $000\bar{1}$
	$0001, 000\bar{1}$	Pd	Polished and annealed	Layer, preferential Pd (111)

[a] Data from Ref. 64 and references therein.

Chapter 3

Cluster Model Studies of *d*-Metal Particles Supported on the MgO(001) Surface

3.1 Adsorption of *d*-metal atoms on the regular MgO(001) surface

3.1.1 Introduction

Transition and noble metal particles deposited on oxide ceramics are materials of growing interest due to their technological importance. Among the most obvious present and potential applications of these materials are sensors, photovoltaic cells, magnetic recording and catalysis [1,16,18,136–138]. A detailed understanding of the metal/ceramic interactions at the microscopic level is crucial for elucidating the chemical reactivity of supported metal systems. However, it is usually difficult to obtain comprehensive information on metal/oxide interfaces from experiments alone because their properties are affected by many factors that are difficult to control under experimental conditions. On the other hand, first-principles periodic slab and embedded cluster calculations enable one to separate these factors and

furnish a complementary means for expanding our understanding of metal species supported on oxides [24,25].

Complexes of single metal atoms and subnanoscale clusters with oxide supports are of key importance for unraveling the initial stage of interface formation. Isolated metal adatoms represent elementary building blocks of supported metal systems. Thus, exploring the bonding between metal atoms and oxide supports as well as the structure of such surface complexes is a prerequisite for characterizing larger supported moieties. There is enough experimental evidence that metal nucleation preferentially occurs at defects, rather than at regular sites of well-ordered terraces of oxide surfaces. Nevertheless, structural and energetic details of the interaction of single metal atoms with regular surface sites of oxides are also essential for clarifying the issues of nucleation and growth of supported metal species. Interaction with defects is considered in the subsequent section.

Several years ago in our group a systematic density functional (DF) cluster model investigation of the bonding of single transition metal atoms with the energetically favored O^{2-} site of the touchstone ideal MgO(001) surface it was performed [26]. Using a generalized gradient approximation (GGA) in the form of BLYP exchange-correlation (xc) functional [139-141], surface complexes of nine atoms of three subgroups of the periodic system (Cu, Ag, Au; Ni, Pd, Pt; Cr, Mo and W) were studied. Based on the strength of the bonding with the MgO(001) substrate, the considered metal atom adsorbates were divided into two groups. Cu, Ag, Au, Cr and Mo atoms revealed weak or very weak adsorption bonds; their interaction is mainly due to polarization in the surface electrostatic field with only little mixing with the substrate orbitals. At variance, Ni, Pd, Pt and W atoms were found to form notably stronger bonds with the oxygen anions of MgO(001); these bonds are of covalent polar origin with only limited, if any, charge transfer between metal and oxide, reflecting the low reactivity of the most stable (001) surface of the wide-gap insulating MgO crystal. Subsequently, the interaction of selected single *d*-metal atoms with regular oxygen sites of MgO(001) was computationally addressed by our (e.g., [30,34]) and other groups using cluster models (e.g., [142-146]) as well as periodic slab models [146,147,148].

Recently, an advanced tool for cluster embedding in an elastic polarizable environment (EPE) was implemented [34], which allows one to accurately describe the adsorption on metal-oxide surfaces taking relaxation effects into account. The EPE embedding scheme was used to rationalize the adsorption of isolated Pd atoms on regular and defect sites of MgO [34] and revealed the adsorption-induced relaxation to be noticeable, ~10 % of the adsorption energy, even for regular O^{2-} sites on the rigid MgO(001) surface. Furthermore, compared to the still very frequently cited results of the early study [26], a systematic compilation of observables calculated for M_1/MgO systems should be based on a model that reflects the contemporary level of sophistication. Hence, it seemed desirable to correct deficiencies of cluster embedding merely in point charge array without involving cationic pseudopotentials at the cluster boundary [149]. Finally, in the earlier study [26] the BLYP xc functional was employed, one of the GGA family; nowadays, more modern GGA xc functionals are considered to be more precise. Thus, we decided to carry out a new systematic computational study of single transition metal atom adsorption on the regular O^{2-} site of MgO(001) that (i) relies on one of the most accurate DF model cluster approaches available and (ii) is extended to three further transition metal subgroups, Co, Fe and Mn, compared to the previous work [26]. The current study includes in total 17 different *d*-metal adsorbates [38]; this work constitutes the first part of our broader comparative investigation on metal atoms adsorbed on the oxygen and vacancy sites of MgO(001) [37].

3.1.2 Computational details

Spin-polarized calculations were performed using the linear combination of Gaussian-type orbitals fitting-functions density functional method (LCGTO-FF-DF) method [150] implemented in the parallel computer code PARAGAUSS [151,152]. The GGA functionals BP86 [139,153] and PBEN [154] were used self-consistently. For surface complexes of the second- and third-row metal atoms scalar-relativistic effects were taken into account employing a second-order Douglas-Kroll transformation to decouple electronic and positronic degrees of freedom of the

Dirac-Kohn-Sham equation [155,156]. Flexible orbital basis sets were adopted from our earlier calculations [26] or constructed following the strategy developed there. However, for 5*d*-atoms we presently use a more flexible scheme with *m*+3 contractions for each angular momentum where *m* is the number of occupied shells of a given atom. The final orbital basis sets were as follows: (15*s*11*p*6*d*) → [6*s*5*p*3*d*] for 3*d*-atoms, (18*s*13*p*9*d*) → [7*s*6*p*4*d*] for 4*d*-atoms, (21*s*17*p*12*d*7*f*) → [9*s*8*p*6*d*4*f*] for 5*d*-atoms (for Au (21*s*17*p*11*d*7*f*) → [9*s*8*p*6*d*4*f*]), (15*s*10*p*1*d*) → [6*s*5*p*1*d*] for Mg cations and (13*s*8*p*1*d*) → [6*s*5*p*1*d*] for O anions. All contractions (scalar-relativistic for 4*d*- and 5*d*-atoms) were of the generalized, atomic form. The auxiliary basis set utilized in the LCGTO-FF-DF method was employed to represent the electron charge density for treating the classical Coulomb electron-electron interactions [150]. For every atom, the auxiliary basis was constructed as follows: the exponents of *s* and r^2 fitting functions were generated from all or selected *s* and *p* orbital exponents, respectively, using a standard scaling procedure [150]; five *p* and five *d* "polarization" exponents have been added on each atomic center as geometric series with a factor 2.5, starting with 0.1 for *p* and 0.2 for *d* exponents. The binding energies are computed with respect to the sum of the corresponding spin-polarized ground state energy of the free metal atom and the energy of the relaxed MgO(001) model cluster; the energies are counterpoise corrected for the basis set superposition error.

The EPE cluster embedding follows the procedure described in detail elsewhere [34]. To model the regular O^{2-} adsorption sites of the (001) surface of MgO, we employed as a quantum mechanical (QM) part of the system the stoichiometric cluster O_9Mg_9, with the coordination sphere of each O anion at the cluster boundary saturated by 16 pseudopotential Mg^{2+} centers [157], Mg^{pp*}, entirely without electrons. To generate the crystal environment of the resulting QM cluster $O_9Mg_9(Mg^{pp*})_{16}$ we optimized the structure of a six-layer slab model of the MgO(001) surface with an atomistic simulation at the classical molecular mechanical (MM) level [158]. The environment affects the QM cluster both electrostatically, via the Madelung field, and mechanically, via short-range forces of the classical ions at the cluster boundary. A specially designed QM/MM interface

Table 3.1. Parameters of adsorption complexes of single metal atoms M at the oxygen sites of the regular MgO(001) surface calculated with EPE embedded cluster models $M/O_9Mg_9(Mg^{pp}*)_{16}$. [a]

M	State[b]	z(M-O)[c] pm	z(M-Mg_4) pm	Δz(O) pm	Δr(Mg_4) pm	Δz(Mg_4) pm	ΔE_b(BP86) kJ mol^{-1}	E_b(BP86) kJ mol^{-1}	E_b(PBEN) kJ mol^{-1}
Cu	$^2A_1$	201 (206)	211	8	5	4	14	93	72
Ag	$^2A_1$	229 (229)	238	5	4	3	9	46	25
Au	$^2A_1$	224 (223)	230	5	5	5	14	96	71
Ni	$^1A_1$	179 (180)	187	9	6	7	19	151	124
Pd	$^1A_1$	208 (208)	212	4	4	6	11	137	105
Pt	$^1A_1$	196 (197)	199	4	7	8	26	231	202
Co	$^4B_2$	215 (188)	225	8	4	5	32	74	58
	$^2B_2$	184 (185)	196	13	7	15	20	118	87
Rh	$^4B_2$	229 (231)	238	9	4	6	7	90	69
	$^2B_2$	204 (208)	211	9	6	9	14	125	93
Ir	$^4A_2$	200 (205)	209	11	9	8	37	134	106
	$^2B_2$	200 (200)	206	9	7	10	19	136	112
Fe	$^5B_1$	191 (201)	207	16	8	7	24	136	112
	^3E	194 (197)	210	18	6	8	19	41	16
Ru	$^5B_1$	218 (226)	230	14	7	8	20	86	60
	$^3B_1$	214 (215)	219	8	5	8	27	81	59
Os	$^5B_1$	204 (211)	215	14	9	10	30	162	152
	^3E	196 (198)	203	12	9	12	31	147	120
Mn	$^6A_1$	206 (216)	227	21	7	6	28	96	72
	$^4B_1$	184 (188)	197	16	9	10	32	22	-6
Re	$^6A_1$	217 (226)	234	18	7	7	24	146	125
	$^4B_1$	193 (197)	202	14	11	12	20	111	82
Cr	$^7A_1$	221 (201)	238	16	5	6	13	61	51
	$^5A_1$	192 (200)	214	25	8	9	8	55	32
Mo	$^7A_1$	238 (246)	254	12	5	3	11	52	34
	$^5A_1$	203 (209)	224	22	8	7	8	56	30
W	$^7A_1$	226 (234)	241	13	6	3	15	71	43
	$^5A_1$	203 (208)	221	20	9	8	36	151	121

[a] z(M-O) – M-O bond length, z(M-Mg_4) – height of M above the plane of the four nearest-neighbor Mg atoms, Δr and Δz – adsorption induced displacements of the O and Mg_4 atoms in the directions radial and normal to the surface (a positive sign indicates an outward or upward shift, respectively), E_b – M-MgO binding (adsorption) energy, ΔE_b – energy gain due to the substrate relaxation caused by the presence of the adsorbate.

[b] Assigned state based on the occupation numbers of (high spin) electron configuration from a spin-polarized calculation; assignments are unique in all cases considered.

[c] In parentheses, the M-O bond length computed for the substrate kept frozen at the structure optimized without an adsorbate present.

ensures that also the environment responds to the (electronic and geometric) changes of the cluster region, relative to a cluster which represents the regular unperturbed surface [34]. Both the QM cluster and the MM environment are allowed to relax due to changes caused by an adsorbate so that the structure of the whole system is determined variationally by total energy minimization [34]; thus, except for the imposed C_{4v} point group symmetry, adsorption-induced relaxation was studied free of constraints.

Binding energies were computed with respect to the sum of the spin-polarized ground state energy of a free metal atom and the energy of the relaxed MgO(001) model cluster [38]. Also, these energies were counterpoise corrected [159] for the basis set superposition error in single-point fashion at the equilibrium geometry of the surface complexes.

3.1.3 Results

Calculated observables for the adsorption complexes $M/O_9Mg_9(Mg^{pp*})_{16}$ of all studied atoms M are displayed in Table 3.1. The PBEN adsorption energies are approximated by values computed for geometries optimized with the BP86 GGA. For several complexes exhibiting close lying states, we show results obtained for more than one electron configuration.

Cu subgroup. In line with our earlier findings [26], these adsorbates forms rather weak $M–O^{2–}$ bonds with BP86 energies not exceeding 96 kJ mol^{-1} ($\leq$ 72 kJ mol^{-1} at the PBEN level). The ground state doublet $d^{10}s^1$ electron configuration of the free adatoms is sufficiently stable to determine the $^2A_1$ state of the adsorption complexes unequivocally. Ag/MgO is the most weakly bound system. Relativistic effects notably facilitate *d-s* mixing for the Au atom in Au/MgO and render this complex stronger bound than Cu/MgO. The contribution of the adsorption-induced relaxation to the adsorbate-substrate interaction is rather small, ~10 kJ mol^{-1}; still, it comprises 15–20% of the overall binding. Structurally, this relaxation is manifested by minor alterations of the M-O bond lengths, ≤5 pm. The oxygen anion involved in the adsorption interaction exhibits an upward displacement and its four nearest Mg neighbors in the surface plane are moved upwards/outwards. All these

displacements are well below 10 pm and the substrate distortions die off so rapidly that all other atoms undergo are displaced at most by 1 pm. This last statement holds also for the other complexes of the present study.

Ni subgroup. Experimentally, a free Ni atom is characterized by almost degenerate ground state terms corresponding to the triplet configurations d^8s^2 and d^9s^1 [160]. At both the BP86 and PBEN levels, the latter configuration is calculated 151 kJ mol^{-1} lower and hence taken as reference in this study (see also next section). For Pd and Pt atoms, the lowest energy terms of the electron configurations d^{10} and d^9s^1, respectively, are more clearly favored over the lowest energy states of other electron configurations. Despite the open-shell nature of free Ni and Pt atoms, the ground states of the adsorption complexes of all three atoms of this subgroup on MgO are singlets. These surface moieties show significantly stronger binding, 135–232 kJ mol^{-1} at the BP86 level (106–203 kJ mol^{-1} with PBEN GGA), than complexes of coinage metals. The 5*d*-metal congener Pt is bound most strongly of all atoms considered. This is also reflected in adsorption heights z(Pt-O) (essentially unaffected by relaxation) and z(Pt-Mg$_4$) that are shorter than the corresponding characteristics of the Pd complex. The relaxation energies, although notably increased in absolute value compared to the Cu subgroup complexes, are relatively small, ~10 % of the overall binding only. For this subgroup, displacement size and pattern of the substrate atoms close to the O^{2-} adsorption site are qualitatively the same as for the analogous coinage metals.

Co subgroup. Starting from this subgroup of the metal adatoms we show results for the lowest states belonging to two multiplicities of each adsorption complex (Table 3.1), because most of these high-spin metal atoms (and thus their surface complexes) feature closely-lying electron configurations. Our atomic references for Co is the DF ground state quartet d^8s^1, which is at the BP86 level 61 kJ mol^{-1} (Co) lower than the experimental quartet ground state d^7s^2. In the adsorbed Co, Rh and Ir moieties on MgO, partial spin quenching to doublet states is favored up to 39 kJ mol^{-1} over the corresponding complexes with retained quartet states. The resulting adsorption energies in the most stable doublet complexes are rather high and only slightly smaller than in the corresponding complexes of the Ni

subgroup. Structural parameters and relaxation patterns of Co subgroup complexes are very much reminiscent of their Ni subgroup congeners.

Fe subgroup. These atoms remain in their highest spin quintet states in the most stable adsorption complexes. However, in line with the larger propensity of 3*d*-atoms to form high-spin complexes, only Fe/MgO system exhibits a clear preference for the quintet state. The binding energies of the species Ru/MgO and Os/MgO as triplets and as quintets are close. Given these small energy differences and the various approximations (in particular, of the DF approach used), one is not able to definitely exclude a triplet ground state of the complexes Ru/MgO and Os/MgO. The surface species of Fe and Os fall into the range of rather strongly bound species, E_b > 96 kJ mol^{-1}, whereas the Ru complex is markedly weaker bound. Relaxation energies and structural features of the quintet adsorption complexes of the atoms of the Fe subgroup are in fair agreement with the corresponding parameters of the systems formed by atoms of the Ni and Co subgroups. Only the moiety Ru/MgO features a somewhat longer adsorption bond.

Mn subgroup. Both adsorption complexes studied clearly exhibit highest-spin sextet ground states. Binding energies are intermediate between strongly and weakly bound metal adatoms on the regular MgO(001) sites, 96 and 145 kJ mol^{-1} at the BP86 level or 77 and 125 kJ mol^{-1} a the PBEN level. The M-O bond lengths of both Mn and Re derivatives shrink notably, by 10 pm, due to relaxation. Also, these adsorbates “pull” the nearby oxygen anion vertically out of the substrate by as much as ~20 pm.

Cr subgroup. This set of surface moieties in very high spin states reveals probably the most complicated picture of the structure and bonding, in line with our earlier findings [26]. Indeed, the calculated energetics is clear enough only for the W/MgO system where a quintet ground state is predicted for the adsorption complex. No obvious energy preference could be found for either the septet or the quintet states of the Cr/MgO and Mo/MgO moieties. But no matter in which state these surface complexes of Cr and Mo are formed, their binding energies are expected to feature the weakest values among all 17 metal adsorption systems under study. Interestingly, the states $^7A_1$ of the adsorbed Cr, Mo and W moieties are

characterized by notably steeper M-O potential energy curves (not shown); the energy minima are ~30 pm closer to the surface than their lower-spin $^5A_1$ analogs. A W adatom in the state $^5A_1$ binds as strongly to the surface as the other strongly bound 5*d*-atoms under consideration, except Pt.

3.1.4 Discussion

The calculated binding energies of the M/MgO complexes presented in Table 3.1 show a similar trend as those obtained in the computational study of nine transition metal atoms adsorbed on the regular O^{2-} site of MgO(001) [26]. However, closer inspection reveals notably larger adsorption energies in the present work where we aim at quantitative estimates of the binding in the surface complexes under consideration. Three factors contribute to these differences.

First, the former investigation [26] neglected the surface relaxation of MgO and relied on substrate cluster model with ion positions fixed as determined by the bulk-terminated geometry of the MgO substrate. For ground state configurations of the complexes M/MgO (Table 3.1) the adsorption-induced substrate relaxation increases the BP86 adsorption energy by 10–29 kJ mol^{-1}, with the largest contributions of 39 kJ mol^{-1} for Ir and W systems. Structurally, the relaxation is manifested by modest alterations of the adsorption bond lengths, Δz(M-O) ≤ 10 pm.

The next issue is employment of the notably improved cluster embedding scheme in this work. In particularly, the deficiency of the embedding technique adopted earlier [26], namely an environment model that consists only of a finite array point charges without pseudopotentials has been repaired here by introducing bare pseudopotential centers Mg^{pp*} instead of positive point charges in the vicinity of the outer oxygen anions (see Section 3.1.2). In this way, the artificial distortion of the electron density of diffuse O^{2-} anions at the cluster boundary is avoided [149]. As estimated for the adsorption of Cu, Ni and Pd atoms on MgO(001) [30], this improved embedding increases the calculated binding energies by ~19 kJ mol^{-1}; concomitantly, the bond distances z(M-O) shrink.

Finally, the GGA xc functionals BP86 and PBEN used in the present study furnish calculated observables somewhat different from the values obtained in Ref. 26 with the BLYP GGA. This observation is closely related to the central problem of DF applications: the necessity to work with an approximate xc functional as the exact functional is not known [161]. A case study of adsorbed atomic Cu on MgO(001) thoroughly discussed how calculated observables of supported metal atoms on MgO depend on the xc potential [143]. Very recently, difficulties connected with the definition of the proper reference atomic energy in DF applications were analyzed in detailed for the representative system Ni/MgO(001) [146]. It is shown that for some metal atom references such as Ni the energy variation may cause deviations in calculated adsorption energies exceeding 96 kJ mol^{-1}. Fortunately, this question seems to be important only for a very limited number of (primarily 3*d*-) transition metal atoms; this issue is outside the scope of the present work. More relevant is the evaluation of the effect of various GGA xc functionals on the calculated parameters of the adsorption complexes M/MgO. This effect can be exemplified by the system Pd/MgO [26,30,34] where the adsorption energy obtained with the BP86 xc functional is about 29 kJ mol^{-1} larger than the value of a similar BLYP calculation.

To establish, which of the contemporary xc functionals provides most accurate adsorption energetics for elementary M_1/MgO complexes, unambiguous theoretical or experimental reference data are required. Unfortunately, precise benchmark calculations that treat electron correlation effects with sufficient accuracy in a realistic model do not seem practicable yet. Also, pertinent experimental results are essentially absent. One of the very few examples of experimental estimates of an atomic metal adsorption energy on non-defective sites of MgO(001) has been obtained for the system Pd_1/MgO, 116±19 kJ mol^{-1}, as derived from atomic force microscopy data [47]. Adsorption energies calculated for this system with two different xc functionals (Table 3.1), 137 kJ mol^{-1} (BP86) and 105 kJ mol^{-1} (PBEN), both fit the relatively large range of the "experimental" values. Also, note that the hybrid B3LYP functional yields a binding energy for this surface complex, 93 kJ mol^{-1}, that is slightly smaller than the PBEN value [144].

Based on experience with calculated adsorption energies on metal surfaces [62,154], the PBEN functional furnishes adsorption energetics in close agreement with experiment, whereas the corresponding BP86 binding energies are somewhat larger in a systematic fashion. The GGA xc functional PW91 [162] overestimates binding energies slightly more than the BP86 functional. It remains to be seen whether these findings can be generalized for the energetics of supported metal particles on oxides.

It is also interesting to compare our model cluster results to results obtain with periodic slab models. A comparison for atomic Pd and Pt species on α-Al_2O_3(0001) showed good agreement for both structural parameters and adsorption energies [163].Two periodic slab model computational studies of M_1/MgO(001) complexes are worth noting in this context. Pseudopotential GGA PW91 calculation of Cu atoms on O^{2-} sites of defect-free MgO(001) surface resulted in a Cu-O distance of 204 pm and a binding energy of 96 kJ mol^{-1} [147]. Indeed, agreement with our values of 201 pm and 93 kJ mol^{-1} (Table 3.1), respectively, is almost quantitative if one bears in mind the significant differences in the computational methods and the above mentioned enhanced bond energies at the GGA PW91 level. A recent slab model study with the VASP code using the PW91 xc functional [148] considered single-atom adsorption on MgO(001) for seven metals of the present series. There, fully relaxed plane wave slab model calculations were performed, however without taking spin-polarization effects into account in both the adsorption complexes and the metal atom references. As the latter (atomic) spin-polarization energy contribution usually prevails for the systems under consideration, such a spin-restricted approximation should result in somewhat increased adsorption energy values. For the complex Pd/MgO formed by closed-shell fragments, the slab model results [148] E_b(PW91) = 129 kJ mol^{-1} and z(Pd-O) = 206 pm essentially agree with our data E_b(BP86) = 137 kJ mol^{-1} and z(M-O) = 208 pm (Table 3.1). For the doublet species Ag/MgO and Au/MgO with the atomic references being doublets as well, spin polarization effects are expected to be largely compensated; again, the slab model adsorption energy values, 51 kJ mol^{-1} (Ag/MgO) and 87 kJ mol^{-1} (Au/MgO), are quite close to our BP86 results, 46 and 96 kJ mol^{-1},

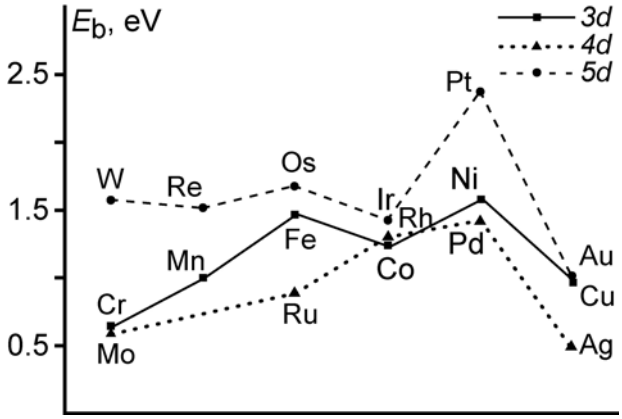

Figure 3.1. Adsorption energies E_b of the most stable complexes of single *d*-metal atoms on O^{2-} sites of the regular MgO(001) surface calculated with BP86 GGA (see also Table 3.1).

respectively, despite a difference of about 10 pm in the adsorption bond length. Already for Pt/MgO, the PW91 binding energy of Ref. 148 exceeds our BP86 value by 29 kJ mol^{-1}, the upper limit of the error estimate due to neglected of spin-polarization, given in Ref. 148 for the whole set of adsorption moieties treated there. Even larger energy differences (in the same direction) are found for the complexes Rh/MgO (58 kJ mol^{-1}), Ir/MgO (174 kJ mol^{-1}) and Ru/MgO (145 kJ mol^{-1}). If we turn off spin-polarization in these species, the differences are reduced to -2, 70 and 14 kJ mol^{-1}, respectively, thus explaining the major part of the discrepancies between the two set of calculated data.

One may wonder whether the altered values of metal-oxide binding energies in this work (Table 3.1) manifest a change in the interaction picture with respect to the earlier studies [26,30] performed without EPE embedding. Particularly interesting is the issue of a possible oxidation of metal atoms by the regular MgO(001) support. The amount of the adsorbate-substrate charge transfer is strictly speaking not an observable value, but this characteristic is still often addressed in qualitative considerations. To quantify the charge transfer we used charges on metal atoms derived from the electrostatic potential generated by the adsorption complexes, so-called potential-derived charges [164].The metal atom charges did not exceed 0.2 e in any of systems considered here; some of these atoms are even assigned slightly negative charge. This finding is a clear argument for a polar

covalent type of adsorption interaction which definitely is not in line with the alternative conceivable binding mechanism relying on metal oxidation on MgO(001). In this sense, the interaction of single *d*-metal atoms with another widely used (inert) oxide support, α-Al_2O_3(0001), is not very different. As exemplified by the EPE embedded BP86 adsorption studies of monatomic Pd and Pt species on α-alumina (furnishing adsorption energies at 110 and 165 kJ mol^{-1}, respectively), the authors were unable to diagnose any propensity of adsorbates to become oxidized [163].

Finally, it is worth commenting on the dependence of the calculated adsorption energies on the metal adatom positions in the periodic table (Figure 3.1). These data exhibit a notably more complicated trend than simply a monotonic increase of the adsorption energy from the noble metals to the left till the middle of the periodic table predicted in Ref. 148, based on results for five 4*d*- and three 5*d*-metal adsorbates (see above). For 4*d*- and 5*d*-metal adsorption complexes, we observe that adsorption energies increase from Au and Ag moieties to Pt and Pd ones, respectively, with a subsequent (almost) monotonous energy reduction in each of the two series till W and Mo congeners. The 3*d*-adatoms show more pronounced oscillation of the adsorption energy and the trend is less systematic. In line with earlier data [26], the atoms Cu, Ag, Au, Cr and Mo as well as the atoms Mn and Ru not calculated before, manifest a rather weak adsorption bond, $\leq$ 1 eV at BP86 level, whereas the other adatoms under study are characterized by a relatively strong interaction with the oxide support. Another interesting conclusion can be drawn from Figure 3.1: for any one group of the periodic table, 5*d*-metal complexes show the strongest binding while the 4*d*-metal analogs form the weakest bonds in all cases but one, Co vs. Rh [165]. Interplay of three main contributions – polarization of the adsorbates at the surface in the electrostatic field, M*s*/*d*-O2*p* orbital overlap and Pauli repulsion of the filled electronic shells – determines the strength of the adsorption bonds.

3.1.5 Summary

An accurate (scalar-relativistic) all-electron DF method with a consistent cluster embedding in an elastic polarizable environment was used to perform a systematic investigation of metal adsorption atom on regular O^{2-} sites of the relaxed surface MgO(001). 17 single *d*-metal adatoms of the third, fourth and fifth rows of the periodic table were included in the study. The embedding method used treats both the central quantum mechanical region of the oxide clusters under study and their classical environment variationally, without artificial constraints for geometry optimization. In general, relaxation effects of the rigid MgO substrate were shown to contribute 10–20% (or even slightly more) to the adsorption energy of the metal atoms in the ground states of the surface complexes. The present, more precise adsorption energies based on the BP86 and PBEN exchange-correlation functionals reflect the same nature of the adsorption bonds as described in the earlier study of this group where a less sophisticated cluster embedding and a different exchange-correlation functional was applied. Namely the adsorption bonds can be described as metal polarization accompanied by (some) orbital mixing, but without noticeable adsorbate-substrate charge transfer. Note that the failure of DF methods to correctly reproduce the ground state of certain metal atom references (e.g., of Ni, Co and Fe) may affect calculated values of the adsorption energy of such atoms.

3.2 Single *d*-metal atoms on F_s and F_s^+ defects of MgO(001)

3.2.1 Introduction

Metal atoms on oxides, as elementary building blocks of more extended supported metal systems, are of key importance for unraveling the initial stage of interface formation. Therefore, characterizing the bonding between metal atoms and oxide supports as well as the structure of such surface complexes is a prerequisite for describing larger supported moieties which result from metal nucleation and cluster growth. There is experimental evidence that metal nucleation often preferentially occurs at defects rather than at regular sites of well-ordered terraces of oxide surfaces [47–49] among these sites, oxygen vacancies or color centers are considered to play a special role [108]. Nevertheless, structural and energetic parameters of the interaction of single *d*-metal atoms even with well-known surface point defects, such as neutral and charged oxygen vacancies (F_s left after removal of an O atom and F_s^+ formed when an O^- anion is missing) on the terraces of the ubiquitous oxide support MgO, have been theoretically quantified only for selected systems [29–31,33–35,41–43,144,145,148,166–168]. Furthermore, most of these data calculated by DF methods are not entirely consistent with each other or with results for regular MgO(001) surface sites for various methodological reasons. Some were obtained with cluster models, others with slab models; also, different xc functionals have been employed, hampering a quantitative comparison. Thus far, DF results for the adsorption of the following *d*-metal atoms on F_s sites of MgO(001) have been communicated: Cu [29,30,43], Ag [29–31,148,168], Au [35,148], Ni [30,145], Pd [30,31,34,41,42,144,148, 166,167,168], Pt [33,148], Rh [148,168], Ir [148], Ru [148] and Nb [148]. Up to now, adsorption on *charged* F_s^+ centers has been challenging for periodic slab-model approaches. Thus, for the adsorption on this defect site only cluster-model data are available and the list of atoms is even shorter: Cu [30,43], Ag [30,31,168], Ni [30,145], Pd [30,31,34,42,144,168], Rh [168]. For some of the latter atoms, DF calculations were

also performed on the doubly-charged F_s^{2+} site (missing O^{2-} anion) of MgO(001) [31,34,145].

Recently developed tools for embedding of cluster models in a so-called elastic polarizable environment (EPE) [34,51] allow one to accurately describe the adsorption on oxide surfaces taking relaxation effects into account. Using this advanced computational technology, we studied the adsorption of single *d*-metal atoms on regular O^{2-} sites of MgO(001) [38] (see Section 3.1) extending earlier work [26] by three metal subgroups (Co, Fe, and Mn). The current study, carried out with exactly the same high-level computational approach as described in the previous section, deals with interactions of 17 different single *d*-metal atoms with surface defects F_s and F_s^+ on MgO(001).

Thus, the present work reports a theoretical quantification of a major part of conceivable complexes, which *d*-metal atoms form on MgO(001) terraces. Together with the results on the M/O^{2-} systems [38] this study provides a comprehensive data base calculated at one and the same level, namely with one of the most accurate cluster model approaches currently available. This data base presents a unique opportunity to analyze and rationalize adsorption parameters of transition metal atoms on MgO(001) across the periodic table, which is one of the main goals of this study. In particular, we demonstrate that (i) at variance with general belief, some *d*-metal atoms do form stronger bound adsorption complexes at regular sites than at F-type surface defects; (ii) metal atoms in M/F_s complexes accumulate considerable amount of electron density provided by the vacancy and the trend of the adsorption energies is governed by this negative charge; and (iii) core level energies of adsorbed metal atoms are characteristic and can be of help for detecting experimentally M/O^{2-}, M/F_s and M/F_s^+ structures on MgO(001).

In Subsection 3.2.2 we describe the cluster models employed to represent F_s and F_s^+ defects on MgO(001) terraces and we provide computational details. In Subsection 3.2.3, we present the calculated structural and energetic parameters of adsorption complexes on the F_s and F_s^+ sites and we characterize their electron distribution. In Subsection 3.2.4 we discuss peculiarities of and trends in the bonding of metal atoms on the oxygen vacancies compared to the regular sites. We

also consider how the structure of adsorption complexes of transition metal atoms at oxides can be characterized with the help of calculated core-level energies. Conclusions are summarized in Subsection 3.2.5.

3.2.2 Computational details and models

Spin-polarized calculations were performed using the LCGTO-FF-DF method [24] as implemented in the parallel computer code PARAGAUSS [151,152,]. Two GGA xc functionals, BP86 [139,153] and PBEN [154] were used self-consistently. For the second- and third-row metal atoms, scalar-relativistic effects were taken into account employing a second-order Douglas-Kroll transformation to decouple electronic and positronic degrees of freedom of the Dirac-Kohn-Sham equation [155,156].

We adopted the same flexible orbital basis sets as described in Subsection 3.1.2: (15*s*11*p*6*d*) → [6*s*5*p*3*d*] for 3*d*-atoms, (18*s*13*p*9*d*) → [7*s*6*p*4*d*] for 4*d*-atoms, (21*s*17*p*12*d*7*f*) → [9*s*8*p*6*d*4*f*] for 5*d*-atoms {for Au (21*s*17*p*11*d*7*f*) → [9*s*8*p*6*d*4*f*]}, (15*s*10*p*1*d*) → [6*s*5*p*1*d*] for Mg cations and (13*s*8*p*1*d*) → [6*s*5*p*1*d*] for O anions. The latter basis set was also used to describe electrons trapped by the oxygen vacancies. All contractions specified in brackets (scalar-relativistic for 4*d*- and 5*d*-atoms) were of generalized, atomic form. Note, that for 5*d*-atoms we used a more flexible scheme than in earlier calculations [26,30] with *m*+3 contractions for each angular momentum where *m* is the number of occupied shells of a given atom. In the LCGTO-FF-DF method, an auxiliary basis set is employed to represent the electron charge density when evaluating the classical Coulomb (Hartree) part of the electron-electron interaction. For every atom, the auxiliary basis was constructed as follows: the exponents of *s* and r^2 fitting functions were generated from all or selected *s* and *p* orbital exponents, respectively, using a standard scaling procedure [150]; five *p* and five *d* "polarization" exponents have been added on each atomic center as geometric series with a factor 2.5, starting with 0.1 for *p* and 0.2 for *d* exponents.

The EPE cluster embedding has been described in detail elsewhere [34]. To be consistent with our model of the regular O^{2-} adsorption sites of the MgO (001) surface [34,38], we employed here the clusters O_8Mg_9, neutral and positively charged, as QM part of the system to mimic the vacancies F_s and F_s^+, respectively. The coordination spheres of O anions at the cluster boundary were saturated by pseudopotential Mg^{2+} centers (Mg^{pp*}) [34,169] entirely without electrons; we employed 16 such centers in total. We used the same six-layer slab model of the MgO(001) surface, optimized previously [34,38] in an atomistic simulation at the classical MM level [158] to generate the crystal environment of the resulting QM clusters. The environment affects the QM cluster both electrostatically, via the Madelung field, and mechanically, via short-range forces of the classical ions at the cluster boundary. Both the QM cluster and its MM environment, optimized to account for the vacancy formation, were allowed to relax in response to changes caused by the adsorbate so that the structure of the whole system was determined variationally by total energy minimization [34]. Except for the imposed C_{4v} point group symmetry, adsorption-induced relaxation was studied free of constraints with the BP86 functional.

Binding energies were computed with respect to the sum of the spin-polarized ground state energy of a free metal atom and the energy of the relaxed MgO(001) model cluster [38]. These energies were counterpoise corrected [159] for the basis set superposition error in single-point fashion at the equilibrium geometry of the surface complexes. Spin contamination was quantified as difference of the expectation value $<\hat{S}^2>$ of the total spin of the Kohn-Sham (KS) determinant and the ideal value, $S(S+1)$, where $S = n/2$ and n is the number of unpaired electrons. Most of the systems studied showed essentially no spin contamination, at most 1% with respect to $S(S+1)$; exceptions will be explicitly mentioned in the following. To characterize charge redistribution in the adsorption systems, we computed potential-derived charges (PDC) [170] which reproduce the electrostatic field in the area above the MgO (001) surface plane of the cluster models.

3.2.3 Results

Table 3.2 displays the lowest-energy electron configurations of free transition metal atoms calculated with the xc functionals BP86 and PBEN. For all atoms but Co and Ni, the KS ground-state configuration agrees with that detected experimentally [160,171]. The problem to define the proper reference energy of transition metal atoms in DF calculations has been thoroughly addressed elsewhere [28,145,146]. Therefore, this issue (pertinent here only to Co and Ni) will not be dealt with in the present work. The energies of the configurations from Table 3.2 (in the highest possible spin state) will be used in the following to determine adsorption energies of metal atoms on MgO which will be corrected for the basis set superposition error with the help of the counterpoise method.

The calculated BP86 observables of the adsorption complexes M/F_s and M/F_s^+ studied are displayed in Table 3.3 and Table 3.4, respectively. For those complexes which exhibit closely lying states, we show results for more than one electron configuration. We will now discuss these observables in more detail, starting with group 11 systems and moving to the left in the periodic system, to group 6.

Group 11: Cu, Ag, Au. The coinage metal atoms exhibit the simplest valence electron configuration, $d^{10}s^1$, among all atoms under scrutiny: a filled n*d*-shell and a singly occupied (n+1)*s* orbital. This electron configuration is energetically well separated from the first excited configuration d^9s^2, especially for Ag [160,171] and thus very stable. At the F_s site of MgO(001), these atoms form a rather strong bond, with BP86 adsorption energies ranging from 180 to 310 kJ mol^{-1} (Table 3.3). Calculated large negative charges, -0.8 to -0.9 *e* on metal atoms, imply a considerable accumulation of electron density there, in line with the very low electronegativity of the F_s site on MgO(001) [30] which makes the two (almost free) electrons, accommodated by the vacancy, easily accessible for binding. Ag/F_s is the most weakly bound system. Relativistic effects facilitate *d-s* mixing notably for the Au atom of the Au/F_s complex and render it stronger bound than Cu/F_s. The contribution of the adsorbate-induced relaxation to the adsorption interaction is very small, both energetically and structurally. This statement holds also for most of the

Table 3.2. Electron configurations of *d*-metal atoms M, used as reference[a] for binding energies of adsorption complexes M/F_s and M/F_s^+ on MgO(001). The configurations correspond to the lowest energies calculated at the all-electron BP86 level.

Cr d^5s^1	Mn d^5s^2	Fe d^6s^2	Co d^8s^1	Ni d^9s^1	Cu $d^{10}s^1$
Mo d^5s^1		Ru d^7s^1	Rh d^8s^1	Pd d^{10}	Ag $d^{10}s^1$
W d^5s^1	Re d^5s^2	Os d^6s^2	Ir d^7s^2	Pt d^9s^1	Au $d^{10}s^1$

[a] All states are of the highest possible spin. The configurations correspond to the lowest energies calculated at the all-electron BP86 level.

adsorption complexes of other atoms under study; the few exceptions will be mentioned in due course. $M\text{-}F_s^+$ bonds of all three coinage metal atoms are stronger than the corresponding $M\text{-}F_s$ bonds, uniformly by ~50 kJ mol^{-1} (cf. Table 3.3 and Table 3.4). This is due to the coupling of the single valence *s* electron of the metal atoms with the single electron of the F_s^+ vacancy, leading to a rather strong covalent interaction. In turn, notably lowered charges on the metal of the M/F_s^+ systems imply a reduced contribution of the *polar* (electrostatic) bonding interaction.

Group 10: Ni, Pd, Pt. Experimentally, free Ni atoms feature almost degenerate low-energy triplet states corresponding to the configurations d^8s^2 and d^9s^1. The latter configuration is calculated 147 kJ mol^{-1} lower and taken as reference in this study (see Table 3.2). For Pd and Pt atoms, the lowest energy terms of the electron configurations d^{10} and d^9s^1, respectively, are more clearly favored over the lowest energy states of other electron configurations. Despite the open-shell nature of free Ni and Pt atoms, the ground states of the adsorption complexes of all three atoms of this group on F_s defects of MgO(001) are singlets. This finding is reminiscent of the configuration change from d^9s^1 to d^{10}, which occurs when Ni species interact with carbonyl ligands [172,173]. The group 10 atoms are considerably stronger bound to the substrate, 278, 387 and 581 kJ mol^{-1} for Ni, Pd and Pt, respectively (Table 3.3), than the coinage metal atoms. In fact, Pt at the F_s site is calculated to be most strongly bound among all atoms under study, both at F_s and F_s^+ MgO defects. This is also reflected by the adsorption height $Pt\text{-}Mg_4$ of Pt/F_s

Table 3.3. Calculated parameters of adsorption complexes formed by single *d*-metal atoms M at surface oxygen vacancies F_s of MgO(001). [a]

M	State [b]	z(M-Mg_4), [c] pm	Δr(Mg_4), pm	Δz(Mg_4), pm	q(M), *e*	$\Delta\varepsilon$(M n*s*), eV	ΔE_b^{BP86}, kJ mol^{-1}	E_b^{BP86}, kJ mol^{-1}
Cu	$^2A_1$	173 (178)	3	0	-0.93	0.63	3	189
Ag	$^2A_1$	196 (193)	3	1	-0.81	0.42	3	178
Au	$^2A_1$	182 (184)	2	0	-0.85	0.48	5	311
Ni	$^1A_1$	137 (143)	4	2	-0.54	1.59	8	278
Pd	$^1A_1$	148 (157)	4	2	-0.60	0.58	14	387
Pt	$^1A_1$	146 (176)	4	4	-0.59	1.43	13	581
Co	$^2B_2$	169 (170)	2	1	-0.65	0.98	4	224
Rh	$^2B_2$	155 (160)	4	2	-0.53	1.03	4	342
Ir	$^2B_2$	152 (183)	5	5	-0.74	1.37	14	465
Fe	$^5A_2$	209 (218)	4	3	-0.37	1.01	7	127
	^3E	177 (193)	5	5	-0.39	1.74	8	123
Ru	$^5A_2$	216 (224)	4	2	-0.32	0.42	6	129
	$^3B_2$	172 (178)	6	6	-0.40	2.32	11	280
Os	$^5B_1$	196 (203)	5	3	-0.52	0.74	5	243
	$^3B_2$	163 (166)	5	6	-0.52	2.21	12	356
Mn	$^6A_1$	240 (242)	2	1	-0.30	1.04	3	74
	$^4B_1$	191 (218)	5	4	-0.38	2.42	15	57
Re	$^6B_1$	201 (204)	7	4	-0.30	1.27	10	85
	$^4B_1$	172 (175)	8	6	-0.30	2.24	15	143
Cr	$^7A_1$	224 (232)	3	0	-0.54	0.21	3	92
	$^5A_1$	218 (217)	5	3	-0.35	0.14	5	46
Mo	$^7A_1$	242 (245)	7	5	-0.60	0.59	9	109
	$^5A_1$	210 (210)	6	4	-0.24	1.04	22	114
W	$^7A_1$	217 (223)	6	3	-0.32	0.71	17	178
	$^5A_1$	207 (223)	5	2	-0.74	0.41	14	184

[a] z(M-Mg_4) – height of M above the plane of the four nearest Mg atoms, Δr and Δz – adsorption induced displacements of the Mg_4 atoms in radial direction and normal to the surface (a positive sign indicates an outward or upward shift, respectively), q(M) – potential-derived charge of atom M, $\Delta\varepsilon$(M n*s*) – spin-averaged shift of the core M n*s* level with respect to the corresponding level of the adsorption complex M/O^{2-} (in the lowest-energy state listed in Table 3.5), E_b^{BP86} – M-MgO binding (adsorption) energy, ΔE_b^{BP86} – energy gain due to the substrate relaxation caused by the presence of the adsorbate.

[b] Assigned state based on the occupation numbers of the (high spin) configuration from a spin-polarized calculation; assignments are unique in all cases considered. Systems with spin contamination > 10%: Co/F_s, $^2B_2$ – 66%; Fe/F_s, ^3E – 30%; Mn/F_s, $^4B_1$ – 19%; Cr/F_s, $^5A_1$ – 14%.

[c] In parentheses, the height computed for the substrate fixed at the structure which was optimized without an adsorbate.

Table 3.4. Calculated parameters of adsorption complexes formed by single *d*-metal atoms M at the surface oxygen vacancy F_s^+ of MgO(001). All notations as in Table 3.3.

M	State	z(M-Mg$_4$), pm	Δr(Mg$_4$), pm	Δz(Mg$_4$), pm	q(M), e	$\Delta\varepsilon$(M ns), eV	ΔE_b^{BP86}, kJ mol^{-1}	E_b^{BP86}, kJ mol^{-1}
Cu	$^1A_1$	160 (155)	1	3	-0.46	-1.97	6	242
Ag	$^1A_1$	186 (183)	2	5	-0.30	-2.25	8	229
Au	$^1A_1$	166 (165)	2	4	-0.42	-2.17	10	358
Ni	$^2A_1$	173 (168)	2	4	-0.21	-2.84	5	223
Pd	$^2A_1$	154 (155)	1	2	-0.30	-1.90	4	255
Pt	$^2B_2$	152 (154)	1	3	-0.19	-2.73	6	376
Co	$^3B_2$	183 (182)	2	4	-0.17	-2.18	5	202
Rh	$^3B_2$	179 (174)	0	2	-0.17	-2.02	3	238
Ir	^3E	165 (166)	2	4	-0.14	-2.55	6	297
Fe	$^4B_1$	190 (190)	2	4	-0.12	-1.19	8	166
	$^2B_2$	188 (188)	2	4	-0.13	-1.30	5	88
Ru	$^4B_1$	197 (198)	3	5	-0.07	-1.84	6	179
	$^2B_2$ [a]	180 (177)	1	3	-0.14	-0.43	2	131
Os	$^4B_1$	175 (178)	4	6	-0.22	-1.62	6	274
	$^2A_1$	170 (172)	3	5	-0.24	-1.80	7	212
Mn	$^5B_1$ [b]	197 (198)	2	4	-0.07	-0.39	5	81
Re	$^5B_1$	190 (191)	4	6	-0.01	-1.08	8	98
	$^3A_2$	201 (186)	2	4	-0.01	-1.54	5	44
Cr	$^6A_1$ [c]	214 (212)	1	3	-0.02	-2.26	3	116
Mo	$^6A_1$ [d]	222 (220)	1	3	0.06	-1.83	3	127
W	$^6A_1$	207 (208)	3	4	0.01	-1.83	5	192
	$^4A_2$	193 (193)	4	5	-0.01	-2.17	4	99

[a] Spin contamination 87%.

[b] $^3A_2$ state calculated to be unbound (negative adsorption energy).

[c] $^4A_2$ state calculated to be unbound (negative adsorption energy).

[d] $^4A_2$ state calculated to be very weakly bound, E_b^{BP86} = 16 kJ mol^{-1}, z(M-Mg$_4$) = 207 pm.

which is drastically reduced, 30 pm, by relaxation from 176 to 146 pm. All three M/F_s species exhibit notably smaller negative metal charges (by absolute value) than their coinage metal analogs, but these charges nevertheless indicate a

significant electron density transfer from the substrate. The particularly strong interaction M-F_s at the neutral defect site can be traced back to the most favorable electron configuration $(a_1)^2(a_1^*)^0$ of these surface species [30] where the bonding orbital a_1 (with a significant contribution of the vacancy) is filled whereas its antibonding counterpart a_1^* is empty. This simple model predicts lower binding energies in the M/F_s^+ species where an electron is removed from the bonding orbital a_1. Our calculations indeed yield lower binding energies for the complexes on the F_s^+ site (Table 3.3 and Table 3.4), by 55 kJ mol^{-1} for Ni and 132 kJ mol^{-1} for Pd. However, such a reduced covalent interaction appears to be not the only mechanism that leads to weaker bonding in the M/F_s^+ complexes of this group relative to the M/F_s species. In the Pt/F_s^+ system, the electron missing compared to the Pt/F_s complex is removed from the essentially nonbonding Pt 5*d* orbital b_2, the HOMO of Pt/F_s, instead of the bonding orbital a_1 which is relatively stabilized in case of Pt. Nevertheless, the Pt-F_s^+ bond is significantly weaker, by 205 kJ mol^{-1}, than the Pt-F_s bond. Therefore, similarly to the coinage metal complexes, other effects are also important for binding, e.g., the electrostatic contribution associated with the transfer of electron density from the substrate to the adsorbate. The negative charges on the metal centers in M/F_s^+ are smaller by factors of 2 or more than in M/F_s, but still remain noticeable, -0.2 to -0.3 *e*.

Group 9: Co, Rh, Ir. Our DF atomic reference for Co is the ground state quartet d^8s^1 (Table 3.2), which at the BP86 level is 61 kJ mol^{-1} lower than the experimentally found quartet ground state d^7s^2 [160,171]. The averaged experimental energy difference between the lowest terms of the configurations d^8s^1 and d^7s^2 is -40 kJ mol^{-1} [171]. In the adsorbed Co, Rh, and Ir moieties on F_s sites of MgO(001), partial spin quenching to doublet states (configurations b_2^1) is favored over the corresponding quartet states. Note, however, that the $^2B_2$ state of Co/F_s is severely spin contaminated, by 66% (Table 3.3); thus, a noncontaminated doublet state should be even more favored. The destabilization of the quartet states of the M/F_s species of this group relative to the doublets is at least in part due to the fact that the antibonding orbital a_1^* is occupied in the quartets, but remains empty in the doublets. The adsorption energies in these doublet state complexes with respect to

the corresponding DF atomic ground state are rather high: 224, 342 and 465 kJ mol^{-1} for Co, Rh and Ir, respectively (Table 3.3). These values are only slightly smaller than those in the corresponding complexes of the Ni group. Negative charges accumulated in these moieties are even somewhat larger than for their group 10 analogs. The marked relaxation-induced reduction of the Ir-Mg_4 adsorption height is comparable to that mentioned above for the Pt/F_s complex. In all three M/F_s^+ complexes of group 9, triplet electron configurations are lowest in energy (Table 3.4): $(a_1)^1(b_2)^1$ (state $^3B_2$) for M = Co, Rh and $(e)^1(b_2)^1$ (state ^3E) for Ir where a *d*-orbital of e character is depleted at variance with the mixed *s*-*d*-orbital a_1 in the Co and Rh analogs. That a_1 level becomes significantly more stable in Ir/F_s, similar to what we have seen for Pt/F_s, relative to Ni/F_s and Pd/F_s. This is a consequence of relativistic stabilization of *s* orbitals. The M/F_s^+ species exhibit somewhat smaller binding energies, about 200–300 kJ mol^{-1}, than the corresponding M/F_s systems. Unlike for the latter complexes, the potential-derived charges on M were calculated to be only slightly negative, at most -0.2 *e*.

Group 8: Fe, Ru, Os. The high-spin metal atoms of this group as well as those in groups to their left in the periodic table often feature closely-lying electron configurations; this statement also holds for the corresponding surface complexes. Therefore, from now in this subsection we will show, when applicable, results for the lowest states belonging to two multiplicities of each adsorption complex (Table 3.3 and 3.4). The binding energies of the species Fe/F_s in the triplet and quintet states are very close in energy, whereas the Fe-Mg_4 heights differ by as much as ~30 pm (Table 3.3). Note, however, the spin contamination of the calculated triplet. In the moieties Ru/F_s and Os/F_s, the triplet states are clearly preferred, in line with the reduced propensity of 4*d*- and 5*d*-atoms to form high-spin complexes. The three most stable systems M/F_s of the group 8 metals interact slightly weaker with the substrate, 130–360 kJ mol^{-1}, than their n*d*-analogs of group 9 and they show a somewhat smaller charge separation. In all complexes of Fe, Ru and Os with the F_s^+ site, quartet states are definitely favored over the doublet states, by 50–80 kJ mol^{-1}, (Table 3.4). The binding energies of the systems Fe/F_s^+, Ru/F_s^+, and Os/F_s^+ are

slightly smaller than the values of their group 9 counterparts. The negative charge values on the adsorbates remain small.

The genealogy of the electron configurations (and states) characterizing the group 8 systems is rather complex. To illustrate this complexity, we start with the species Fe/F_s^+, Ru/F_s^+, and Os/F_s^+, the ground states of which all are $^4B_1$ quartets (Table 3.4), derived from the same electron configuration $(e)^2(b_2)^1$ (only open shells are shown). Addition of one electron to these complexes, formally transforming them into their M/F_s analogs, is accompanied by a distinct rearrangement of the electronic structure that depends on the metal. In Ru/F_s and Os/F_s, this extra electron and an electron depleted from the formerly closed shell $(a_1)^2$, mainly of metal *d* character, now both fill the orbital e, resulting in the triplet electron configuration $(a_1)^1(b_2)^1$, state $^3B_2$ (Table 3.3). In the 3*d* analog Fe/F_s the enhanced propensity to form high-spin states is manifested in a decoupling of the $(b_1)^2$ shell and a concomitant promotion of the spin-flipped electron into the vacant orbital a_1*; see the discussion of group 10. Finally, for Fe/F_s one obtains the quintet state $^5A_2$ with configuration $(b_1)^1(a_1)^1(b_2)^1(a_1)^1$, energetically slightly favored over the lowest triplet state ^3E with configuration $(e)^3(b_2)^1$ (Table 3.3).

Group 7: Mn, Re. The two adsorption complexes M/F_s under discussion feature different spin states in their ground state (Table 3.3). Mn/F_s slightly prefers a sextet ground state over the quartet state which, however, is spin contaminated by 19%. On the other hand, for Re/F_s the quartet configuration is ~60 kJ mol^{-1} lower in energy. These systems, Mn/F_s in particular, are among the most weakly bound M/F_s complexes studied here. The quartet and sextet configurations of the adsorption complex Mn/F_s, although energetically quite comparable, exhibit even more distinct adsorption heights (by 50 pm!) than the triplet and quintet configurations of Fe/F_s (see above). For both M/F_s^+ systems, we found the quintet state $^5B_1$ preferred. The Re complex at F_s^+ is notably less stable than its F_s analog, whereas the Mn/F_s^+ species is almost as weakly bound as Mn/F_s. As a result, also among the M/F_s^+ complexes, the Mn and Re derivatives exhibit essentially the weakest adsorption bonds. The electronic structure of the complexes Mn/F_s^+ and Re/F_s^+ [configuration $(a_1)^1(e)^2(b_2)^1$ and a $^5B_1$ quintet state] correlates with that of their group 8 analogs

which feature one valence electron more [configuration $(a_1)^2(e)^2(b_2)^1$ and a $^4B_1$ quartet state] (Table 3.4). Whereas the ground state valence electron configuration of Re/F_s is the same as that of Os/F_s^+, $(e)^2(b_2)^1$, the configuration of the 3*d*- species Mn/F_s, $(b_1)^1(e)^2(b_2)^1(a_1)^1$, exhibits a higher-spin state than Fe/F_s^+.

Group 6: Cr, Mo, W. This set of surface moieties M/F_s in very high spin states reveals probably the most complicated picture of structure and bonding. Indeed, only for the Cr/F_s system is the calculated energetics definite: a septet ground state is predicted (Table 3.3; the quintet $^5A_1$ features 14% spin contamination). We were not able to identify a clear energy preference for either the septet or the quintet states of Mo/F_s and W/F_s. However, no matter in which state these surface complexes of Cr and Mo are formed, their binding energies are expected to be the lowest among all the M/F_s adsorption systems under scrutiny; only Mn/F_s is likely even weaker bound. Also, a W adatom in either spin state exhibits the second-weakest binding to an F_s site among all other 5*d*-atoms under consideration (undercut only by Re). For the M/F_s^+ systems of group 6 atoms, the situation is somewhat simpler, at least as far as the most stable spin configuration is concerned which is a sextet for all three moieties. These complexes, featuring essentially neutral metal adsorbates, were also calculated to be rather weakly bound.

3.2.4 Discussion

Table 3.5 and Figure 3.2 summarize calculated data to highlight and ascertain trends in the binding energy variation of n*d*-metal atoms in complexes with F_s and F_s^+ defects on the MgO(001) surface. These trends should also be compared with our findings for complexes of the same atoms on regular O^{2-} sites of MgO(001) [38], described in Section 3.1.

From Figure 3.2a (upper panel), one immediately recognizes that most M/F_s complexes are notably stronger bound than their M/O^{2-} analogs (Figure 3.2a, bottom panel). This is in line with *all* previous calculations [29–31,33–35,41–43,144,145,148, 166,167,168]. However, quite unexpectedly, there are some exceptions: Fe, Mn and Re atoms are slightly weaker bound (by ~20 kJ mol^{-1} at most) at F_s defect sites than at regular O^{2-} sites. While all metal atoms exhibit

Table 3.5. Binding energies (kJ mol^{-1}) calculated with the GGA functionals BP86 (E_b^{BP86}) and PBEN (E_b^{PBEN}) for the most stable state of adsorption complexes of single *d*-metal atoms M at F_s and F_s^+ defects of the MgO(001) surface in comparison with complexes at regular O^{2-} sites.

M	M/F_s			M/F_s^+			M/O^{2-} [a]		
	State	E_b^{BP86}	E_b^{PBEN}	State	E_b^{BP86}	E_b^{PBEN}	State	E_b^{BP86}	E_b^{PBEN}
Cu	$^2A_1$	189	167	$^1A_1$	242	218	$^2A_1$	93	72
Ag	$^2A_1$	178	152	$^1A_1$	229	203	$^2A_1$	46	25
Au	$^2A_1$	311	278	$^1A_1$	358	326	$^2A_1$	96	71
Ni	$^1A_1$	278	237	$^2A_1$	223	195	$^1A_1$	151	124
Pd	$^1A_1$	387	346	$^2A_1$	255	218	$^1A_1$	137	105
Pt	$^1A_1$	581	505	$^2B_2$	376	336	$^1A_1$	231	202
Co	$^2B_2$	224	194	$^3B_2$	202	181	$^2B_2$	118	87
Rh	$^2B_2$	342	298	$^3B_2$	238	207	$^2B_2$	125	93
Ir	$^2B_2$	465	390	^3E	297	259	$^2B_2$ [b]	136	112
Fe	$^5A_2$ [c]	127	110	$^4B_1$	166	125	$^5B_1$	136	112
Ru	$^3B_2$	280	257	$^4B_1$	179	154	$^5B_1$ [d]	86	60
Os	$^3B_2$	356	319	$^4B_1$	274	254	$^5B_1$	162	152
Mn	$^6A_1$ [e]	74	57	$^5B_1$	81	62	$^6A_1$	96	72
Re	$^4B_1$	143	110	$^5B_1$	98	71	$^6A_1$	146	125
Cr	$^7A_1$	92	79	$^6A_1$	116	106	$^7A_1$ [f]	61	51
Mo	$^5A_1$ [g]	114	88	$^6A_1$	127	111	$^5A_1$ [h]	56	30
W	$^5A_1$ [i]	184	151	$^6A_1$	192	166	$^5A_1$	151	121

[a] Ref. 38.

[b] $^4A_2$: E_b^{BP86} = 134 kJ mol^{-1}, Ref. 38.

[c] ^3E: E_b^{BP86} = 123 kJ mol^{-1}, Table 3.3.

[d] $^3B_1$: E_b^{BP86} = 81 kJ mol^{-1}, Ref. 38.

[e] $^4B_1$: E_b^{BP86} = 57 kJ mol^{-1}, Table 3.3.

[f] $^5A_1$: E_b^{BP86} = 55 kJ mol^{-1}, Ref. 38.

[g] $^7A_1$: E_b^{BP86} = 109 kJ mol^{-1}, Table 3.3.

[h] $^7A_1$: E_b^{BP86} = 52 kJ mol^{-1}, Ref. 38.

[i] $^7A_1$: E_b^{BP86} = 178 kJ mol^{-1}, Table 3.3.

negative charges, these three systems are also among those M/F_s complexes with the least charge separation (as measured by potential-derived charges; see Table 3.3, Figure 3.2b). A very substantial adsorption-induced increase of the electron density on the adsorbates (along with the subsequent increase of the electrostatic adsorbate-substrate attraction) appears to be an important stabilizing factor of M/F_s moieties. (Note that previously the charge separation analysis of selected M/F_s complexes

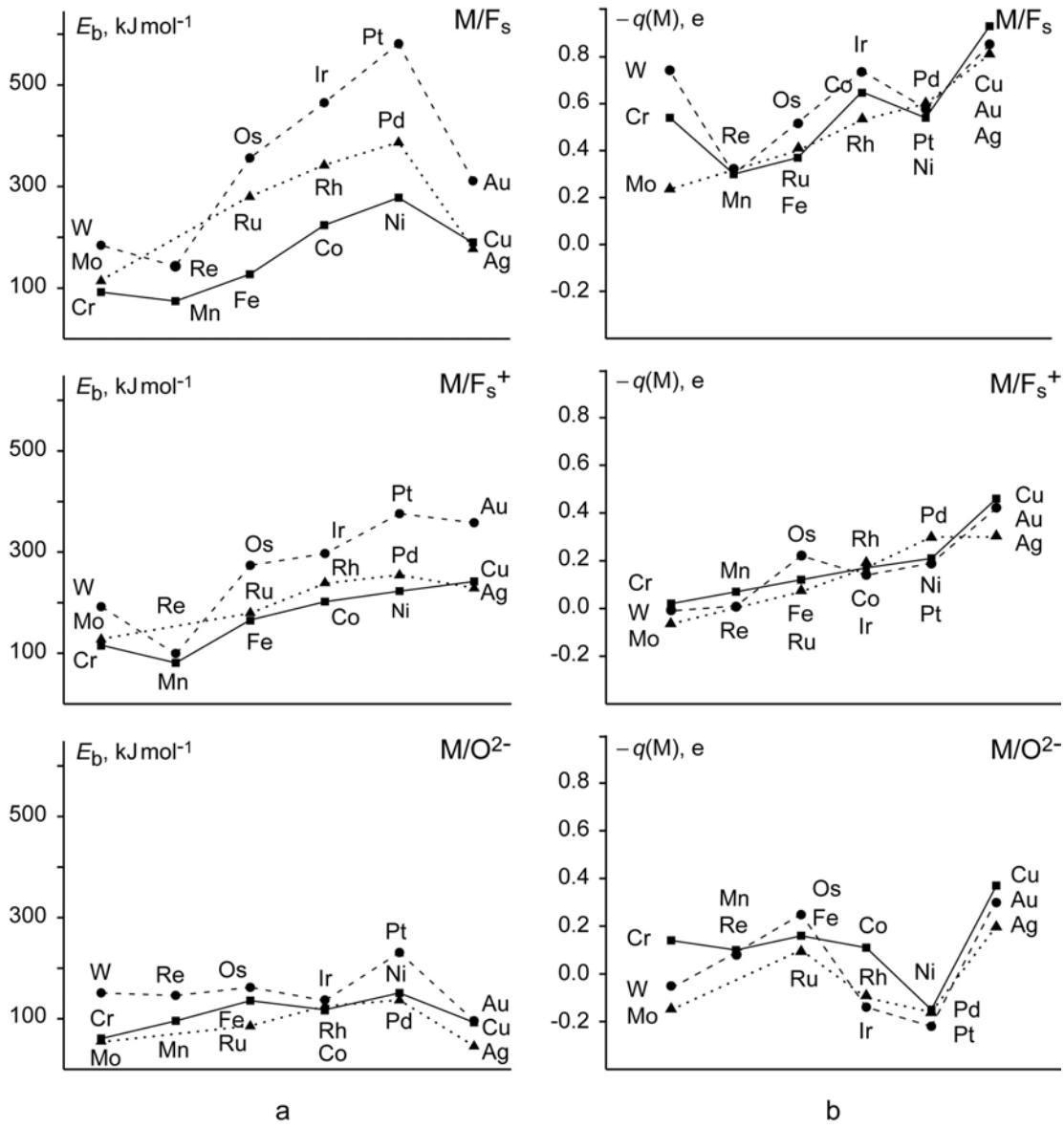

Figure 3.2. Trends in the BP86 binding energies (column a) and potential derived charges (PDC) on adsorbates (column b) of the most stable adsorption complexes of single *d*-metal atoms on oxygen vacancies F_s (upper panels) and F_s^+ (middle panels) of MgO(001) surface in comparison with the energies and PDC values of the metal atoms on the regular O^{2-} sites (bottom panels of columns a and b, respectively; see Section 3.1).

[30] was based on the dynamic dipole moment which indicated a considerably smaller substrate-to-adsorbate electron donation than the present PDC criterion.) M/F_s systems are furthermore stabilized compared to the corresponding M/O^{2-}

analogs as Pauli repulsion with the substrate is reduced when the F_s vacancy is created because the electronic shells of the O center are no longer there.

Finally, as outlined above for adsorbed metal atoms of group 10, covalent effects due to favorable filling of bonding/antibonding orbitals can be much more pronounced for complexes on oxygen vacancies than on regular sites of MgO(001). In fact, all these mechanisms work together and in general result in stronger M-F_s binding compared to M-O^{2-} complexes. This relative strengthening of the adsorption bond for the majority of the metal atoms under scrutiny exceeds 100 kJ mol^{-1} and reaches 350 kJ mol^{-1} for the most strongly bound Pt/F_s species (Table 3.5, Figure 3.2a). Concomitantly, metal-substrate distances (measured by the M-Mg_4 height, Table 3.3) are significantly shorter, by 50–60 pm, for some metals of the right-hand side of the periodic table than the previously computed values for the corresponding M/O^{2-} systems [38].

In each of the examined groups of the periodic table, except for group 11, the 4*d*-atom is calculated to be adsorbed stronger on the F_s site of MgO(001) than the 3*d*-atom, but weaker than the 5*d*-atom, $3d < 4d < 5d$. This is different from the binding energy trend within the group, which we previously established for M/O^{2-} complexes (Figure 3.2a, bottom panel) [38]: $4d < 3d < 5d$. Regarding the energy variation of the M/F_s species along the period (Figure 3.2a, upper panel), atoms of group 7 are slightly destabilized with respect to their group 6 analogs. Moving to the right in each period, the binding energy increases gradually up to species of group 10 and finally it decreases again in group 11. This rather complicated trend reflects the complex character of the interactions experienced by *d*-metal atoms with defect sites of an oxide support, in particular, with F_s sites of MgO(001). Note that these latter sites can be described to good approximation by a very simple model [30] where only two electrons are treated quantum mechanically, moving in the field of the five immediate Mg^{2+} neighbors of the vacancy, represented by bare pseudopotential centers without a basis set, and a set of point charges representing the remaining substrate centers. For each metal, the strength of the resulting bond is determined by the delicate balance of the diverse contributions discussed in the preceding paragraph.

Nevertheless, there is an evident similarity in the general trend of the evolution of binding energies (Figure 3.2a, upper panel) and the alteration of PDC values (Figure 3.2b, upper panel) of the M/F_s complexes along the rows of the periodic table. Both the adsorption energies and the negative charges on the metal atoms exhibit an overall increase from the middle of each row to its right-hand side. There are some exceptions, in particular the complexes of the elements of group 6, which exhibit particularly high spin values, and the complexes of the elements of group 11 complexes; below, we will try to rationalize the values of the latter. This overall similarity implies that the accumulation of electron density on the adsorbates is a factor that governs the adsorption interactions of a series of n*d*-metal atoms with F_s vacancy sites on MgO(001) terraces. Interestingly, the trend in the PDC values is in fair agreement with the trend of the electronegativity values of the metal atoms [174]. However, only very crude adsorption energy estimates are possible on the basis of the electronegativity values; thus, high-level electronic structure calculations will continue to play a crucial role for quantifying this key characteristic.

In the literature, there are hardly reliable experimental data on the adsorption energetics of single *d*-metal atoms at F_s and F_s^+ sites of MgO(001). Moreover, precise benchmark calculations that treat electron correlation effects with sufficient accuracy in a realistic model do not seem practicable yet for the systems under discussion. On the other hand, one of the central problems of DF applications is the necessity to work with an approximate xc functional as the exact functional is not known [161]. Without unambiguous reference data one is unable to definitely establish, which of the contemporary functionals provides the most accurate adsorption energies for elementary M/F_s complexes. However, one can very roughly estimate the general range of DF energies by comparing results obtained with several xc functionals. To this end, we compared binding energies for the M/F_s species from BP86 and PBEN calculations (Table 3.5).

Both sets of energies vary in very similar fashion with the adsorbed metal atoms. PBEN values are uniformly smaller by 10–20% than BP86 results; for the most strongly bound systems, this can amount to energy difference of up to 70–80

kJ mol^{-1}. Importantly, the trend of the uniformly reduced PBEN energies is apparently a systematic one, as it is also manifested for M/F_s^+ and M/O^{2-} complexes (Table 3.5). The hybrid B3LYP functional [140,175] yields binding energies for selected studied complexes M/F_s [168], that are 10–15% smaller than the corresponding PBEN values. The GGA functional PW91 [162] in combination with periodic slab models provides energies for M/F_s species [148] that are in general close to our cluster model BP86 data. As discussed previously [38], some larger deviations are probably due to the neglect of spin-polarization effects [148]. For adsorption on metal surfaces [62,154], the PBEN functional yields energies in close agreement with experiment, whereas the corresponding BP86 binding energies are somewhat larger in a systematic fashion. It remains to be seen whether these findings can be generalized to the energetics of supported metal particles on oxides.

The above considerations on the performance of various GGA and hybrid xc functionals are also valid for M/F_s^+ complexes. Thus, we will discuss only observables calculated for the latter systems at the BP86 level (Table 3.4, Table 3.5 and Figure 3.2).

The F_s^+ site of MgO(001), compared to the F_s site, exhibits two significant differences: (*i*) removal of an electron leaves one unpaired electron in the vacancy which is readily available for covalent bonding with an unpaired electron of a metal atom adsorbate, and (*ii*) concomitantly, the clear propensity of the F_s defects to donate electron density to the metal adsorbates (see above) is drastically reduced for the F_s^+ defects, as indicated, among others, by a strongly enhanced electron affinity of the latter [30]. The first factor is of particular importance for the M/F_s^+ complexes of Cu, Ag, and Au. These complexes feature the most favorable electron configuration $(a_1)^2(a_1^*)^0$ and binding energies which are at least 10% larger that those of their M/F_s analogs with the configuration $(a_1)^2(a_1^*)^1$. At variance, the M/F_s^+ complexes formed by metal atoms of groups 9 and 10 are less stable than their M/F_s counterparts. Complexes of a given metal atom M of groups 6 to 8 at F_s and F_s^+ defects do not show a clear trend in their binding energies. Probably, the energy alteration of M/F_s^+ complexes of elements of groups 6 to 10, relative to their M/F_s congeners, are mainly determined by the combined effect of changes in the

substrate-adsorbate charge transfer and the electron configuration (occupation of bonding/antibonding orbitals, high-/low-spin states). Except for Mn/F_s^+ and Re/F_s^+, all other M/F_s^+ complexes studied were calculated to be more strongly bound than the corresponding complexes M/O^{2-} at regular sites of MgO(001) (Table 3.5, Figure 3.2).

The overall trends in the adsorption energies of single *d*-metals on the F_s^+ sites of MgO(001) over a group of the periodic table are rather similar to those established above for the M/F_s systems. Indeed, in each group, the M/F_s^+ complex of the 5*d*-metal is most strongly bound, whereas that of the 3*d*-atom is least bound, except for the Cu moiety which is ~10 kJ mol^{-1} more stable than the Ag complex. Also, the evolution of the binding energies along a period shows a remarkable similarity for the M/F_s^+ and M/F_s complexes, which implies similarities in the electrostatic (polar) contribution to the bonding, caused by the charge separation between M and F_s^+ subsystems; cf. the trends of the binding energies and potential derived charges as depicted in the middle panels of Figure 3.2a and Figure 3.2b. There are several noticeable differences between the trends of M/F_s and M/F_s^+ complexes: energy variations within one period are smaller for M/F_s^+ systems and the binding energy does not decrease at the end of the period, from Ni/F_s^+ to Cu/F_s^+. Also, the striking disparity of the binding energy and PDC trends when going from group 6 to group 7 complexes M/F_s, which feature a very high spin, does not take place for M/F_s^+ analogs.

Finally, we address opportunities for monitoring the interaction of atomically dispersed metal particles with regular and defect sites of metal oxide supports by means of X-ray photoelectron spectroscopy (XPS). Very recently, the shift of the Au 4*f* XPS peak from 85.8 eV at temperatures below 200 K to 85.4 eV at 300 K has been detected for atomic Au species deposited on TiO_2(110) [176] and attributed to the migration of some Au atoms from a variety of regular surface sites to oxygen vacancies that are a characteristic of the vacuum-annealed TiO_2(110) surface [177]. Although, to the best of our knowledge, analogous experimental data are not yet available for metal atoms on MgO(001), it nevertheless seems worthwhile to study how core-level energies of metal atoms change with the sites of deposition on

MgO(001) and whether similarities exist between adsorption complexes at oxygen vacancies of TiO_2(110) and MgO(001).

As first approximation, we focus on initial-state effects. For this purpose, we listed calculated spin-averaged shifts, $\Delta\varepsilon$(M n*s*), of Kohn-Sham core levels M n*s* for the complexes M/F_s (Table 3.3) and M/F_s^+ (Table 3.4) on MgO(001) relative to corresponding values of the M/O^{2-} adsorption complexes. Very interestingly, the shift $\Delta\varepsilon$(Au 5*s*) = 0.48 eV for Au/F_s [along with $\Delta\varepsilon$(Au 4*f*) = 0.44 eV, not shown in Table 3.3] is close to the value of 0.4 eV measured on TiO_2(110) [176]. The fact that core-level shifts of *all* metal atoms under study on F_s sites (including Au, Table 3.3) are positive, i.e. to lower binding energies, partly reflects the negative charge on the adsorbates. On the other hand, the adsorption complex Au/F_s^+ on MgO(001) features a very different shift $\Delta\varepsilon$(Au 5*s*), -2.22 eV (Table 3.4). This allows one to exclude the analog of this species on TiO_2(110) from being a suitable candidate for rationalizing the experimental $\Delta\varepsilon$(Au 4*f*) signature, all the more as all calculated values $\Delta\varepsilon$(M n*s*) for M/F_s^+ complexes on MgO(001) are *negative* with respect to their reference M/O^{2-} (Table 3.4). The main negative contribution, -1.7 to -1.8 eV (as estimated by Kohn-Sham core-level shifts of a Mg cation used as internal reference in Au, Ag and Cu complexes) is due to the overall elementary positive charge of the M/F_s^+ systems. Thus, core-level shifts of M/F_s and M/F_s^+ complexes relative to the corresponding energies of M/O^{2-} species appear to be characteristic for the type of oxygen vacancy that forms the adsorption site. In addition, calculated $\Delta\varepsilon$ values are expected to help significantly in the structural assignment.

Based on calculated adsorption energies and core-level energies (Table 3.1–3.5) for complexes of various metal atoms, one can predict results of experiments on MgO(001) terraces, which are similar to those reported in Ref. 176 for Au/TiO_2(110). For instance, comparing the deposition of the coinage atoms Au, Ag and Cu, one expects that diffusion of Ag to oxygen vacancy sites will take place at lower temperatures than for Cu and Au because Ag interacts weaker on O^{2-} sites than Cu or Au. Also, the characteristic temperatures at which diffusion starts for Cu and Au should be rather similar. Assuming final-state effects (relaxation in the

presence of a core-level hole at M) to be similar for M/O^{2-}, M/F_s^+, and M/F_s, complexes of the same metal, diffusion resulting in M/F_s species should be accompanied by a moderate positive M core-level shift of 0.4–0.6 eV. On the other hand, formation of M/F_s^+ moieties is expected to be manifested by a negative shift $\Delta\varepsilon$ relative to M/O^{2-}. Many predictions like these, regarding the structure and properties of the complexes M/O^{2-}, M/F_s^+, and M/F_s, can be derived from the present calculated results and these predictions will help in structural assignments of pertinent spectroscopic experiments that are expected to be carried out in the near future.

3.2.5 Conclusions

An accurate (scalar-relativistic) all-electron DF method with a consistent cluster embedding in an elastic polarizable environment was used to study systematically metal atom adsorption on F_s and F_s^+ defects of the relaxed surface MgO(001) in comparison to the previously addressed adsorption on regular O^{2-} sites. Seventeen single *d*-metal adatoms of the third, fourth, and fifth rows of the periodic table were considered. The embedding method used treats both the central quantum mechanical region of the oxide clusters under study and their classical environment variationally, without artificial constraints for geometry optimization.

The adsorption energies presented, obtained with the BP86 and PBEN exchange-correlation functionals, corroborate the general picture of the interactions with oxygen vacancies on MgO terraces derived from studies of selected metal atoms. With few exceptions, these interactions with oxygen vacancies are significantly stronger than with the regular sites and they are accompanied by a notable transfer of electron density from the F_s site to the *d*-metal adsorbate. In most groups, 4*d*-atoms are adsorbed stronger than 3*d*-atoms, but weaker than 5*d*-atoms, on both kinds of the defects studied. This is at variance with the trend in binding energies within each group, $4d < 3d < 5d$, which we previously established for M/O^{2-} complexes. As for the energy variation along the period, in both F_s and F_s^+ complexes, atoms of group 7 are slightly destabilized with respect to their group 6 analogs. Then, within a period, the binding energy increases gradually up to group

10 species and finally it decreases again for group 11, most prominently on the F_s site. These trends appear to be governed by the negative charge on adsorbed atoms and their concomitant electrostatic interactions with the vacancy sites of MgO(001) terraces. The failure of DF methods to properly describe the ground state electron configuration of Ni and Co atomic references may affect calculated values of the adsorption energy of these atoms.

Metal-substrate bonding in general is notably weaker in M/F_s^+ complexes than in their M/F_s analogues. We attribute this difference mainly to electrostatic stabilization of the latter species as a consequence of significant accumulation of electron density on the adsorbed atoms M, donated by the F_s vacancy. Covalent interactions may counteract this electrostatic stabilization and even alter the trend, making some M/F_s^+ complexes favored over their M/F_s congeners, as is the case for the Cu, Ag and Au systems.

XPS core-level shifts of adsorbed metal atoms on MgO(001), approximated as differences of Kohn-Sham eigenvalues, revealed a characteristic dependence on the adsorption site. In combination with experimental XPS data, these calculated data open a way to distinguish between the M/F_s and M/F_s^+ structures on (001) terraces of MgO.

Although single adsorbed metal atoms represent *elementary* building blocks of more extended metal species supported on oxides, precise calculations on these systems and their rigorous analysis are complicated because usually several almost degenerate (magnetic) configurations are involved in the interaction with the substrate. One might invoke the constraint space orbital variation (CSOV) [178,179] method to separate and quantify various contributions to the adsorption energy. However, this approach does not appear promising for most of the systems under study due to their complex open-shell electronic structure.

An obvious extension of the present work will be a systematic study of interactions of single metal atoms with neutral and positively charged oxygen vacancies at lower coordinated surface sites of MgO, e.g. at steps, edges and corners, where their formation is more justified thermodynamically [180]. Likely,

these low-coordinated color centers are even stronger traps for single metal atoms than terrace vacancies [181].

3.3 Adsorption of dimers and trimers of Cu, Ag, Au on regular sites and oxygen vacancies of the MgO(001) surface

3.3.1 Introduction

Deposition of size-selected atomic clusters onto well-defined substrates represents a new method for preparing nanostructured surfaces or highly-ordered thin films with lateral features in the range of 1–100 nm as demanded by current trends in semiconductor industry [182]. A major challenge for the stability of such nanostructures is diffusion and aggregation of deposited particles, which have to be prevented. Equally important is the issue of metal particle mobility on the support in catalytic systems, where supported metal particles are used on a large scale as efficient catalysts [24,25,183]. Thermal aging of catalysts has been attributed to sintering [184], a process whereby small metal species form larger clusters and thus reduce their effective surface area. Therefore, central to progress in these technological fields is understanding at the atomic level of how metal species interact with an oxide support. Particularly important issues are the nature of this interaction and its dependence on the size of the metal particle.

Most theoretical studies of these topics, beyond the adsorption of single *d*-metal atoms [26–35,37,38,148], addressed the adsorption of small *d*-metal aggregates M_n (n = 2–4) [27,32,40–46,148]. Hereby, the defect-free (001) surface of MgO often served as a model surface because of its simplicity, non-polarity, and low reactivity; also, computational studies are simplified by the fact that this surface exhibits only a small degree of relaxation with respect to the truncated bulk. Theoretical studies of the adsorption of very small metal moieties on various defect sites of MgO [29,31–33,35,37,41] were motivated by experimental evidence for different oxide systems [47–50] that point defects may act as stronger nucleation sites for metal particles.

In this section we systematically investigate the adsorption of coinage metal aggregates M_n (M = Cu, Ag, Au; n = 2, 3) on the ideal MgO(001) as well as on oxygen vacancies, F_s and F_s^+ on this surface. These three metals are congeners and exhibit the same valence-shell configuration, $d^{10}s^1$, in the ground state. Previously, Musolino et al. studied the adsorption of Cu_n ($n \leq 13$) on the regular MgO(001) surface using a periodic supercell approach [45,46]. Ferrari et al. investigated how dimers Cu_2 and Ag_2 adsorb on defect-free MgO(001) using an embedded-cluster method [40]. Bogicevic and Jennison reported a comparative plane-wave study of selected 4*d*- and 5*d*-metal atoms and dimers, including those of Ag and Au, adsorbed on regular and neutral O-vacancy sites of MgO(001) terraces [148]. Very recently, the adsorption of Cu_1, Cu_2 and Cu_4 moieties on various sites of MgO was addressed by cluster-model studies focusing on alteration of the optical properties caused by interactions with the support [43].

Adsorption on localized charged defects has so far been a challenge for periodic computational approaches. At variance, our cluster method is well suited for describing the adsorption on charged vacancy sites (which may exhibit a particularly strong structure relaxation) due to a consistent embedding in an EPE [34]. One obtains a more accurate description of heavy metals, especially of Au, if one treats relativistic effects at an all-electron level, which is not feasible with a plane-wave method.

The goals of our study described in this section are: (i) to identify preferred adsorption sites and adsorption geometries for coinage metal dimers and trimers on the defect-free MgO(001); (ii) to explore the nature of the metal-support bonding and to quantify the adsorption energy; (iii) to elucidate the role played by surface defects by comparing dimer adsorption on regular, F_s and F_s^+ sites of MgO(001).

3.3.2 Computational methods and models

The calculations were carried out at the all-electron level using the LCGTO-FF-DF method [150] implemented in the parallel computer code PARAGAUSS [151,152]. We employed the gradient-corrected xc density functional BP86 [139,153]. In

calculations involving Ag and Au, we used the scalar relativistic variant of the LCGTO-FF-DF method which employs a second-order Douglas-Kroll transformation to decouple electronic and positronic degrees of freedom of the Dirac-Kohn-Sham equation [155,156,185]. The Kohn-Sham orbitals were represented by flexible Gaussian-type basis sets, contracted in generalized fashion. We adopted orbital basis sets from our calculations of adsorbed atoms [37,38]: (15*s*11*p*6*d*) → [6*s*5*p*3*d*] for Cu, (18*s*13*p*9*d*) → [7*s*6*p*4*d*] for Ag, (21*s*17*p*11*d*7*f*) → [9*s*8*p*6*d*4*f*] for Au, (15*s*10*p*1*d*) → [6*s*5*p*1*d*] for Mg cations and (13*s*8*p*1*d*) → [6*s*5*p*1*d*] for O anions. The auxiliary basis set utilized in the LCGTO-FF-DF method to represent the electron charge density for treating the Hartree part of the electron-electron interaction was constructed by properly scaling the *s* and *p* exponents of the orbital basis sets using a standard procedure [150]; "polarization exponents" were added as geometric series with factors 2.5, starting with 0.1 for *p* and 0.2 for *d* exponents [150]. The resulting auxiliary basis sets were of the type (15*s*,10r^2,5*p*,5*d*) for Mg, (13*s*,4r^2,5*p*,5*d*) for O, (15*s*,11r^2,5*p*,5*d*) for Cu, (18*s*,13r^2,5*p*,5*d*) for Ag, and (20*s*,17r^2,5*p*,5*d*) for Au.

We employed two clusters $Mg_{10}O_{10}(Mg^{pp*})_{12}$ and $Mg_9O_8(Mg^{pp*})_{12}$ (Figure 3.3 and 3.5) to model the regular O^{2-} adsorption sites of the (001) surface of MgO and oxygen vacancy, F_s and F_s^+, on that surface. Here, the symbol Mg^{pp*} indicates a pseudopotential center Mg^{2+} entirely without electrons [169]. The first cluster was used to model adsorption on regular surface sites and the second one for adsorption on vacancy sites. These models feature C_s symmetry, which was exploited in the calculations. Embedding in an EPE is a sophisticated method, which, by taking relaxation effects into account, affords an accurate description of the adsorption on metal-oxide surfaces [34,38]. A specially designed QM/MM interface ensures a consistent description of the mutual influence of electronic and geometric changes of the QM cluster region and its environment relative to the regular unperturbed surface [34].

In the EPE cluster embedding, we employed the $Mg_{10}O_{10}$ and Mg_9O_8 clusters as the QM part of the system with the coordination sphere of each O anion at the cluster boundary saturated by 12 pseudopotential Mg^{pp*}. To generate the crystal

environment of the resulting QM part, we optimized a two-layer slab model of the MgO(001) surface at the classical MM level [158]. Test calculations produced small differences of only 1 pm for metal-MgO distances and 2 kJ mol^{-1} for metal-substrate binding energies compared to the results of a six-layer slab model used in our studies of deposited single atoms on MgO(001) [37,38].

In line with the prescription for the EPE approach [34], we then carried out an embedded cluster calculation of the unperturbed surface, i.e. without any adsorbate, but possibly with a point defect. When adsorption on vacancies was considered, an F_s or F_s^+ center was represented by "ghost" basis set of oxygen (without the nucleus). At this step, only the QM cluster was relaxed, while the environment was kept fixed at the lattice positions determined in the preceding step. Subsequently, the energy of the resulting structure served as reference of a clean surface.

The adsorption energies, $E_{ad}(n)$, presented this study are per metal atom (n = 2 or 3) and are calculated with respect to the sum of the corresponding spin-polarized ground-state energy of a free metal species, M_n, and the energy of the relaxed MgO(001) model cluster as follows:

$$E_{ad}(n) = [E(\mathrm{MgO}) + E(\mathrm{M_n}, \mathrm{free}) - E(\mathrm{M_n/MgO}) + \Delta E(\mathrm{BSSE})]/n, \qquad (3.1)$$

where E(MgO) is the energy of the relaxed cluster model of either regular or defect site, $E(\mathrm{M_n}, \mathrm{free})$ is the ground-state energy of an M_n species in the gas phase and in its equilibrium geometry, $E(\mathrm{M_n/MgO})$ is the energy of the adsorbate-substrate system, and ΔE(BSSE) is a correction for the basis set superposition error (BSSE), estimated with the counterpoise method [159]. The BSSE corrections were smaller than 20 kJ mol^{-1} per atom.

3.3.3 Results and discussion

A. Adsorption of dimers and trimers on a regular MgO(001)

Dimers. Free dimers Cu_2, Ag_2, Au_2 are characterized by a singlet ground state, $^1\Sigma_g^+$. Their experimental bond lengths [186] are 222, 248 (253 [187,188]),

Table 3.6. Equilibrium geometries (bond lengths in pm, angles in degree), dissociation energies per atom D_e/n (kJ mol^{-1}/atom), and vibrational frequencies ω_i (cm^{-1}) of the free dimers and trimers of Cu, Ag, and Au. Also shown are experimental values where available.

M_n	n	Symmetry	Ground	r_e(M-M)		M-M-M [a]	D_e/n		ω_i
			state	calc.	exp.		calc.	exp.	
Cu_n	2	$D_{\infty h}$	$^1\Sigma_{g+}$	223.1	222 [b]		102	97 [b]	270
	3	C_{2v}	$^2B_2$	229.2		66.8	112	98 [c]	65; 121; 188
	3	C_{2v}	$^2A_1$	240.6		55.9	111		252*i*; 40, 199
	3	$D_{\infty h}$	$^2\Sigma_u^+$	229.9		180.0	104		
Ag_n	2	$D_{\infty h}$	$^1\Sigma_{g+}$	256.9	248 [b], 253 [d]		81	80 [b]	185
	3	C_{2v}	$^2B_2$	263.9		69.6	81	84 [c]	37; 97; 121
		C_{2v}	$^2B_2$	263.3		118.8	81		
	3	C_{2v}	$^2A_1$	278.7		55.6	80		465*i*; 34; 112
	3	$D_{\infty h}$	$^2\Sigma_u^+$	264.1		180.0	81		
Au_n	2	$D_{\infty h}$	$^1\Sigma_{g+}$	252.1	247 [b]		110	111 [b]	175
	3	C_{2v}	$^2B_2$	255.8		134.2	116	123 [c]	18; 107; 111
	3	C_{2v}	$^2A_1$	272.2		56.6	111		125*i*; 58; 126
	3	$D_{\infty h}$	$^2\Sigma_u^+$	257.8		180.0	113		

[a] Angle between the two equal sides. [b] Ref.186. [c] Ref. 196. [d] Refs. 187, 188.

247 pm, respectively; experimental dissociation energies (D_e) [186] amount to 194, 159, 221 kJ mol^{-1}. Our calculated BSSE-corrected dissociation energies (Table 3.6) are in very good agreement with the above values. The calculated bond lengths of Ag_2 and Au_2 somewhat overestimate the experimental values as is typical for BP86 geometries, especially for bonds involving heavy elements [189].

In a recent paper [38], (see Section 3.1), we systematically studied the adsorption of single *d*-metal atoms on regular O^{2-} sites of MgO(001), using a very similar computational approach. Cu, Ag, and Au atoms revealed relatively weak to moderately strong adsorption bonds, 93, 46, 96 kJ mol^{-1}, respectively, at the BP86 level. The interaction of these atoms with the substrate was attributed mainly to polarization in the surface electrostatic field and to Pauli repulsion of the filled electronic shells [38]. The same nature of interaction with the defect-free surface is envisioned for the metal aggregates. If one compares the adhesion energies of single

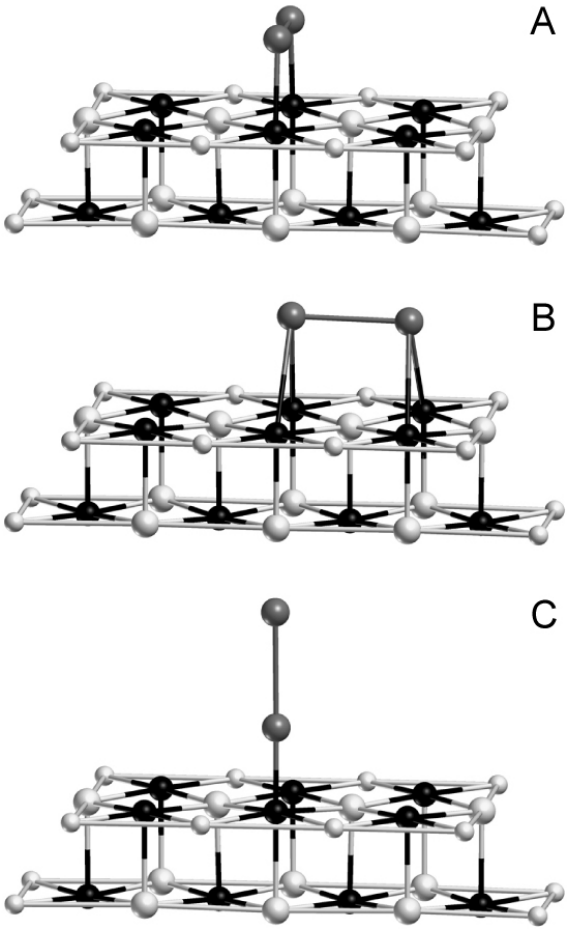

Figure 3.3. Cluster model and three modes for M_2 adsorption on a regular MgO(001) surface. Black, large white, small white, and gray spheres indicate O, Mg, Mg^{pp*}, and M (M = Cu, Ag, or Au) atoms, respectively. For geometries A and B, the symmetry plane is parallel to the plane of paper; for mode C, the symmetry plane coincides with the viewing direction.

atoms at MgO (001) with the binding energies per atom in the free M_2 and M_3 species (Table 3.6), it becomes clear that the M-M bonding is competitive with the bonding to the surface. Particularly small is the adhesion energy of atomic silver, 46 kJ mol^{-1}, whereas the dissociation energy D_e/n is 81 kJ mol^{-1}/atom for both the dimer and the trimer, about two times more than the energy gain due to adsorption of one Ag atom. This is consistent with the lowest adsorption energies found for silver dimers and consistent with the lowest adsorption energies found for silver dimers and trimers in trimers in comparison to their copper and gold analogs, as will be shown below in this subsection.

Not surprisingly, for all three coinage metals the closed-shell nature of M_2 is conserved upon adsorption. In previous studies on Cu_2/MgO(001) [45,46] with the PW91 functional [162] and Ag_2/MgO(001) [40] with the BP86 functional, the vertical "on-top" adsorption mode, where M_2 is standing perpendicular to the surface (mode C in Figure 3.3), was found to be preferred energetically by more than 20 kJ mol^{-1} over any arrangement with the dimer axis parallel to the surface. Recent slab-model calculations on Ag_2/MgO(001) [148] reported a slight tilting of the dimer by 16º from the surface normal. The second-most favorable adsorption complex of Cu_2 was on top of nearest-neighbor O atoms with the dimer axis parallel to the surface [45,46] (mode A in Figure 3.3). In an earlier study by our group on the adsorption of Ag_2, employing simple point-charge embedding, a fixed substrate, and the BP86 functional [40], modes A and B have been found to exhibit almost equal adsorption energies, 16 and 17 kJ mol^{-1}/atom, whereas in geometry C, the binding energy to the surface was 28 kJ mol^{-1}/atom. Therefore, we considered three representative adsorption geometries shown in Figure 3.3 for the whole series of the coinage metal dimers. Although the QM cluster of our model (Figure 3.3) features C_{2v} symmetry, the symmetry constraint in the adsorption complexes was reduced to C_s. Either a symmetry plane passing through nearest-neighbor O centers (modes A and C) or a plane across Mg atoms (mode B) was preserved.

Adsorption energies and optimized geometries for Cu_2, Ag_2, and Au_2 are summarized in Table 3.7. In the present work, we found somewhat stronger bonding of Ag_2 in mode C, 40 kJ mol^{-1}/atom, compared to that of an earlier study [40] and a weaker interaction in mode B, 2 kJ mol^{-1}/atom (Table 3.7). These energy differences of the order of 10 kJ mol^{-1} for the weakly bound Ag_2 adsorbate can in part be attributed to the (small) substrate relaxation effect, not taken into account previously [40]. For all three dimers, Cu_2, Ag_2, and Au_2, the order of preference of adsorption geometries is the same: C > A > B, while the energy difference between A and C increases from Cu_2 to Ag_2 to Au_2 from 34 to 103 kJ mol^{-1}. The current binding energies for Cu_2/MgO(001) (Table 3.7) practically coincide with those obtained in a periodic slab model study [45,46]; they also agree quantitatively with a recent embedded-cluster study [43]. Our calculated bond lengths are generally

Table 3.7. Equilibrium geometries (pm), vibrational frequencies ω_i (cm^{-1}), and adsorption energies per atom (kJ mol^{-1}/atom) for M_2 adsorption on regular sites of the MgO(001) surface. [a]

	Metal M	Mode A	Mode B	Mode C
r(M–M)	Cu	229.4 *225* [b]	228.0	225.6 *220* [b], *229* [c]
	Ag	261.7 *260* [d]	262.2 *262* [d]	257.3 *257* [d], *258* [e]
	Au	259.6	257.7	251.5 *253* [e]
r(M–O)	Cu	209.5 *199* [b]	280.8, 286.8	191.7 *187* [b]
	Ag	239.3 *262* [d]	279.4, 289.6 *273, 273* [d]	224.2 *230* [d], *237* [e]
	Au	234.0	282.0, 288.6	213.6 *218* [e]
r(M–Mg)	Cu	285.4	269.1, 274.5	294.5
	Ag	317.6	275.2, 286.1	313.6
	Au	311.6	283.0, 274.8	307.8
ω_i	Cu	-	-	199
	Ag	-	-	154
	Au	-	-	136
E_{ad} [f]	Cu	48 *56* [b]	16	66 (59) [g] *69* [b], *65* [c]
	Ag	15 *16* [d]	2 *17* [d]	40 (36) [g] *28* [d], *58* [h]
	Au	29	12	82 (74) [g] *82* [h]

[a] See Figure 3.3 for the definition of the adsorption modes. Values from the literature in italics.

[b] Refs. 45, 46. [c] Ref. 43. [d] Ref. 40. [e] Ref. 148.

[f] $E_{ad} = [E(MgO) + E(M_2, free) - E(M_2/MgO) + \Delta E(BSSE)] / 2$.

[g] From calculations where only adsorbate-related degrees of freedom were optimized.

[h] Inferred from Ref. 148, using D_e(Ag-Ag)/2 = 81 kJ $mol^{-1}$and D_e(Au-Au)/2 = 110 kJ mol^{-1} from the present work (Table 3.6).

slightly longer compared to the former work in agreement with the well-known trend of GGA functionals to often overestimate bond lengths, whereas the LDA functional employed for the geometry optimizations in Refs. 45 and 46 often yields

shorter bonds. Comparison with another slab-model study on Ag_2 and Au_2 adsorption [148] shows close agreement for M-M and M-O distances.

Although the M_2 adsorption energies $E_{ad}(M_2)$ are not explicitly given in Ref. 148, they can be inferred from the dimer binding energy on the surface, E_b, and monomer adsorption energy, $E_{ad}(M_1)$, reported therein, using gas-phase dissociation energies of M_2 from our calculations $D_e(\text{Ag-Ag})/2 = 81$ and $D_e(\text{Au-Au}) = 110$ kJ mol^{-1}/atom. The inferred adsorption energy for Au_2, 82 kJ mol^{-1}/atom, agrees quantitatively with our result, whereas the energy of Ag_2 adsorption, 58 kJ mol^{-1}/atom, is 19 kJ mol^{-1}/atom larger than our value. These authors emphasized [148] that tilting by 16º towards a Mg^{2+} cation resulted in a "strengthening of the dimer bond". Although in our calculations such tilting was not allowed by symmetry constraints, we examined the bending potential towards a neighboring Mg^{2+} using the same cluster model as for M_2 on the F_s and F_s^+ vacancy sites (see below), varying only the bending angle. However, we confirmed our former minimum which corresponds to an exactly upright position of a dimer. The resulting potential curve was quite shallow, and tilting by up to 30º resulted in an energy increase of less than 10 kJ mol^{-1}.

Pauli repulsion, which constitutes a significant part of the total energy balance for these relatively weakly bound species, is minimized in a vertical arrangement; hence, the preference of the vertical adsorption mode is not surprising. On the other hand, the energy of M-M interaction is concomitantly maximized because the perturbation of the gas-phase structure is minimized. The vibrational frequencies for the M-M stretching mode are notably reduced compared to gas-phase species, by 17–26% (Table 3.6 and Table 3.7). The adsorption energies E_{ad} decrease in the order $Au_2 > Cu_2 > Ag_2$, just as was found for isolated atoms [37,38]. Yet, whereas for Au_2 and Ag_2 the adsorption energy per atom is about 85% of the values for isolated atoms, $E_{ad}(Cu_2)$ is only about 70% of $E_{ad}(Cu_1)$. Also, the Cu-Cu bond length is elongated by 3 pm in the adsorbed dimer, whereas the geometries of Ag_2 and Au_2 remain practically unchanged upon adsorption. The less efficient binding of the copper dimer may be a result of some loss of the intra-dimer cohesion energy in adsorbed Cu_2 due to bond stretching.

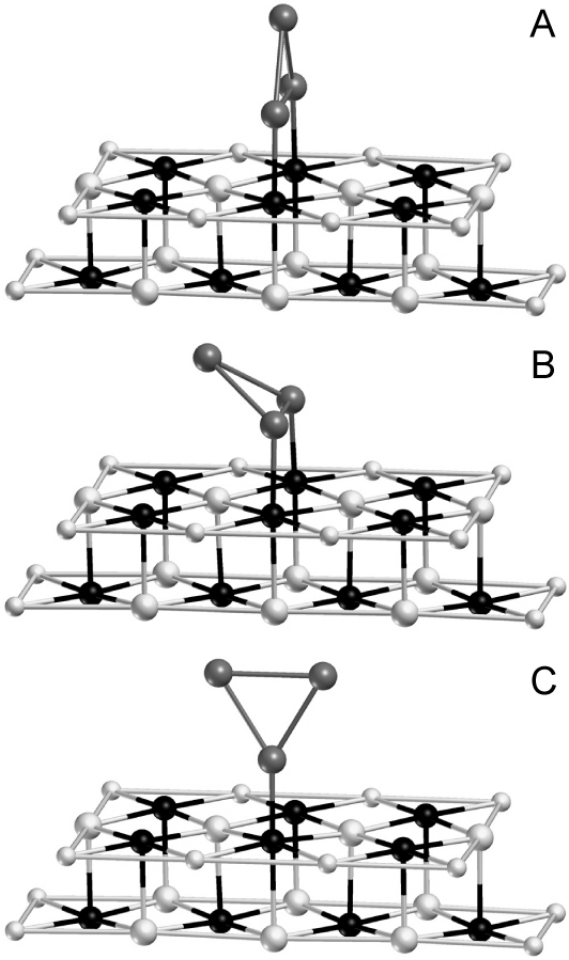

Figure 3.4. Cluster model and three modes for M_3 adsorption on a regular MgO(001) surface. Lay-out of the various atomic spheres as in Figure 3.3. For geometries A and B, the symmetry plane is parallel to the plane of the paper; for mode C, the symmetry plane coincides with the viewing direction.

Trimers. For gas-phase trimers of all three metals, triangular and linear shapes are found to lie energetically rather close (Table 3.6). Most theoretical studies predicted for Cu_3 and Ag_3 an isosceles triangle with two short sides and one long one ($^2B_2$ state) to be 3-40 kJ mol^{-1} lower than the linear structure [190–193]. The other component of the Jahn-Teller distorted doubly degenerate ($^2E'$) state, $^2A_1$, features an isosceles triangle with two long sides and one short one as minimum structure; for Ag_3, it lies less than 3 kJ mol^{-1} above the $^2B_2$ state [193]. This second minimum in C_{2v} symmetry is actually a saddle point connecting two adjacent $^2B_2$ minima [191, 192]. Our calculations corroborate these results, rendering state $^2B_2$ with triangular geometry the global minimum for Cu_3 as well as for Ag_3 and Au_3,

while the state $^2A_1$ with triangular shape and linear species lie slightly higher in energy. In the case of Au_3, several studies predicted the linear chain to be a few kJ mol^{-1} lower than the triangle structures [194,195]. We found the bent-chain geometry ($^2B_2$ electronic state), which can be considered an extremely obtuse triangle (angle 134°), to be favored by 10 kJ mol^{-1} over the ideally linear isomer, whereas the truly triangular $^2A_1$ state is 13 kJ mol^{-1} above the global minimum. Interestingly, for Ag_3 we also obtained an obtuse triangle (angle 119°) as minimum on the $^2B_2$ potential energy surface, only 0.2 kJ mol^{-1} above the global minimum. There is strong experimental evidence that both Cu_3 and Ag_3 are obtuse triangles [196], but no information about Au_3 is available to the best of our knowledge. In any case, the bending potential appears to be rather flat for all three trimers, which makes definitive conclusions on the preferred structures of these energetically closely-lying isomers difficult. Therefore, it is hard, if not impossible, to anticipate preferred adsorbed structures based on favorable gas-phase structures.

When adsorbed on a regular MgO(001) surface, M_3 species of coinage metals assume a vertical orientation, in which two M atoms are bound to two nearest neighbor surface oxygen atoms (mode A in Figure 3.4). In case of Cu_3, the adsorption energy is 61 kJ mol^{-1}/atom (Table 3.8), slightly less than the dimer adsorption energy per atom. The triangle retains two short sides and one longer one and the $^2B_2$ state is preserved, but all bonds elongate slightly. A very similar adsorption geometry has previously been found to be most favorable for Cu_3 adsorbed on MgO(001) (E_{ad} = 63 kJ mol^{-1}/atom) [45,46]. We also identified two other adsorption complexes with close adsorption energies 53 and 51 kJ mol^{-1}/atom, corresponding to modes B and C in Figure 3.4. Geometry B is somewhat tilted with respect to the strictly upright orientation displayed by complex A, the Cu_3 triangle having two long and one short side. This topology correlates with the $^2A_1$ state of the free trimer. In geometry C, only one Cu atom is bound to the surface: the triangle is almost equilateral with the two vertical bonds slightly elongated relative to the geometry of the free cluster. For Ag_3 and Au_3, adsorption geometry A was also found to have the largest adsorption energy (E_{ad} = 35 and 64 kJ mol^{-1}/atom, respectively), closely followed by mode C, where the metal triangle is bound to the

Table 3.8. Equilibrium geometries (bond lengths in pm, angles in degree) and adsorption energies per atom (kJ mol^{-1}/atom) for M_3 adsorption on regular sites of the MgO(001) surface. [a]

	Metal M	Mode A	Mode B	Mode C
r(M–M)	Cu	230.9,[b] 255.9	239.6,[b] 232.9	233.0,[b] 240.1
	Ag	265.1,[b] 288.0	276.9,[b] 264.6	266.7,[b] 280.6
	Au	261.6,[b] 286.5	276.6,[b] 264.8	265.1,[b] 269.3
r(M–O)	Cu	202.7	203.6	189.3
	Ag	230.3	233.4	222.8
	Au	223.8	229.4	211.8
r(M-Mg)	Cu	290.4, 290.4	283.3, 283.6	293.0, 297.8
	Ag	319.0, 319.1	315.1, 314.1	313.2, 322.9
	Au	311.6, 311.5	309.7, 309.9	307.1, 310.7
M-M-M [c]	Cu	67.3	58.2	62.0
	Ag	65.8	57.1	63.5
	Au	66.4	57.2	61.0
E_{ad} [d]	Cu	61, *63* [e]	53	51
	Ag	35	19	30
	Au	64	35	56

[a] See Figure 3.4 for the definition of the adsorption modes. Values from the literature in italics.

[b] Edge length occurring twice. [c] Angle between the two equal sides.

[d] $E_{ad} = [E(\text{MgO}) + E(M_3, \text{free}) - E(M_3/\text{MgO}) + \Delta E(\text{BSSE})] / 3$.

[e] Refs. 45, 46.

surface, by one vertex only (E_{ad} = 30 and 56 kJ mol^{-1}/atom, respectively). The adsorption energies of Ag_3 and Au_3 in geometry B are about half as large as those of the minimum-energy structures A (Table 3.8). The corresponding geometrical parameters summarized in Table 3.8 are similar to those of gas-phase species; again, modes A and C correlate with the $^2B_2$ state and mode B with the $^2A_1$ state. The adsorption energies per atom in the most favorable mode A are somewhat less than those for the corresponding M_2 species adsorbed on regular MgO(001): 5% for Cu_3, 13% for Ag_3, and 22% Au_3.

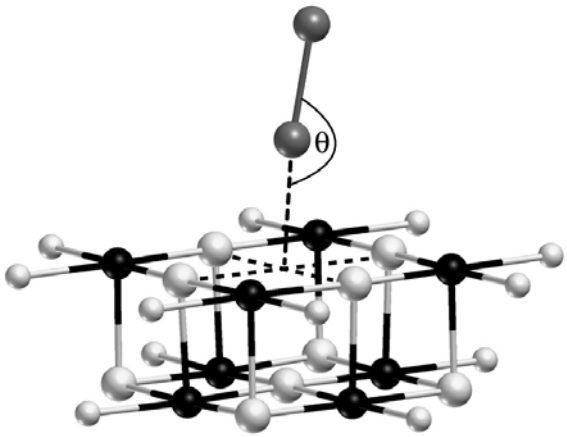

Figure 3.5. Cluster model for M_2 adsorption on F_s or F_s^+ vacancies of a MgO(001) surface. Lay-out of the various atomic spheres as in Figure 3.3. The symmetry plane is parallel to the plane of paper.

B. Adsorption of dimers on F_s and F_s^+ defect sites of MgO(001)

The so-called F_s or F_s^+ centers are point defects on a surface that correspond to oxygen vacancies with one or two free electrons, respectively, trapped in a cavity previously occupied by a missing O atom. The local electronic structure of a neutral F_s center resembles that of a regular O^{2-} site: the surface is formally saturated and exhibits vanishing electron affinity [30]. However, due to the missing oxygen core, Pauli repulsion between the surface and the adsorbate is reduced and the electron density of both the vacancy and the adsorbate is easier to polarize.

Bonding of M_2 to the F_s center can be envisioned as interaction of the doubly occupied vacancy level [in our calculations lying about 2 eV above the valence band of MgO(001)] and the σ* LUMO of the dimer. As can be seen from Table 3.7 and 3.9, binding energies at F_s sites are 1.6–2.7 times larger than those at regular O^{2-} sites. The magnitudes directly correlate with the (relative) LUMO energy of a dimer. The LUMOs of Cu_2 and Ag_2 lie only slightly below the vacancy level, whereas the LUMO of Au_2 is about 2 eV lower. The lower energy of the LUMO of Au_2 is consistent with its higher electron affinity compared to Cu_2 and Ag_2; this, in turn, can be traced back to the strong relativistic stabilization of the Au 6*s* orbital. Thus, Cu_2 and Ag_2 have adsorption energies of the same magnitude, 107 kJ mol^{-1}/atom, and Au_2 adsorbs notably stronger, with 196 kJ mol^{-1}/atom

Table 3.9. Equilibrium geometries (distances in pm, angles in degree), vibrational frequencies ω_i (cm^{-1}), and adsorption energies per atom (kJ mol^{-1}/atom) for M_2 (M = Cu, Ag and Au) adsorption on neutral oxygen vacancies (F_s) of the MgO (001) surface. [a]

	Cu_2	Ag_2	Au_2
M–M	232.6 *239* [b]	266.9 *271* [c]	263.2 *272* [c]
M–M (free dimer)	223.1 *226* [b]	256.9	252.1
z(MgO–M) [d]	169.9	182.4 *174* [c]	162.1 *153* [c]
M–Mg	274.3, 281.6	286.3, 286.4	274.5, 274.6
O*-M-M [e]	172.0	179.9	179.9
ω_i	179	126	121
E_{ad} [f]	107 *111* [b]	107 *122* [g]	196 *191* [g]

[a] Values from the literature in italics. [b] Ref. 43. [c] Ref. 148.

[d] z(MgO-M) is the height of the binding atom of adsorbate above the surface plane defined by four nearest Mg atoms.

[e] O* indicates the position of the missing oxygen atom.

[f] $E_{ad} = [E(MgO\_F_s) + E(M_2, free) - E(M_2/ MgO\_F_s) + \Delta E(BSSE)] / 2$.

[g] Inferred from Ref. 148, using $D_e(Ag\text{-}Ag)/2 = 81$ kJ mol^{-1} and $D_e(Au\text{-}Au)/2 = 110$ kJ mol^{-1} from the present work (Table 3.6).

(Table 3.9). The binding energy of Cu_2 to an F_s center agrees closely with the value of 111 kJ mol^{-1}/atom obtained in a recent embedded-cluster B3LYP calculation [43], although that latter value was not corrected for the BSSE. The shorter distance of Au_2 to the surface, 162 pm, compared to Cu_2, 169 pm, and Ag_2, 182 pm (Table 3.9), is consistent with stronger bonding of the former. Overall, the M-M bond lengths increase notably, by 10–13 pm with respect to gas-phase structures, and the vibrational frequencies decrease by about 30%. We note that the orientation of the dimer with respect to the surface was not restricted to a perpendicular one, but the minimum energy structure for all three dimers corresponds to an almost upright orientation (Table 3.9).

Table 3.10. Equilibrium geometries (distances in pm, angles in degree), vibrational frequencies ω_i (cm^{-1}), and adsorption energies per atom (kJ mol^{-1}/atom) for M_2 (M = Cu, Ag and Au) adsorption on charged oxygen vacancies (F_s^+) of MgO (001) surface.

	Cu_2	Ag_2	Au_2
M–M	230.2	265.6	260.2
M–M (free dimer)	223.1	256.9	252.1
z(MgO–M) [a]	169.6	182.4	162.0
M–Mg	281.6, 285.8	290.6, 293.0	279.4, 280.7
O*-M-M [b]	170.5	150.9	179.5
ω_i	179	117	117
E_{ad} [c]	66	64	116

[a] z(MgO-M) is the height of the binding atom of adsorbate above the surface plane defined by four nearest Mg atoms.

[b] O* indicates the position of the missing oxygen atom.

[c] $E_{ad} = [E(MgO\_F_s^+) + E(M_2, \text{free}) - E(M_2/ MgO\_F_s^+) + \Delta E(BSSE)] / 2$.

Bogicevic and Jennison [148] found both Ag_2 and Au_2 on F_s sites to be tilted significantly, by about 56º from the surface normal towards surface cations. At variance, our prescreening of the bending potential in the plane passing through the vacancy site and the two nearest Mg^{2+} cations, varying only the bending angle, did not confirm their finding and rendered a minimum corresponding to an upright orientation for Ag_2 as well as for Au_2. The adsorption energies of Ag_2 and Au_2 on F_s sites inferred from the data of Ref. 148 are nevertheless in good agreement with our values (Table 3.9). Bogicevic and Jennison [148] used the PW91 functional, which often gives stronger binding. They interpreted the observed tilting towards positively charged cations as an indication of sufficient negative charge transfer from the vacancy to the dimer, particularly to its more distant atom. We also found a notable transfer of electron density to the metal dimers adsorbed on F_s centers, as deduced from computed potential-derived charges (PDC) [170] -0.80, -0.83, and -0.73 *e*, on Cu_2, Ag_2, and Au_2, respectively. The corresponding Mulliken charges were -0.55, -0.47, and -1.30 *e*, respectively. The PDC values are close to those obtained by us for single atoms Cu, Ag and Au adsorbed on F_s sites, -0.93, -0.81 and -0.85 *e*, respectively [37] (Section 3.2). In the case of dimers, the PDC charge is

Table 3.11. Comparison of adsorption energies E_{ad} (kJ mol^{-1}/atom) of single atoms and dimers on regular and defect sites of MgO(001) as well as dissocation energy E_b of adsorbed dimers. [a]

Site	Metal M	D_e(M-M)/2	$E_{ad}(M_1)$	$E_{ad}(M_2)$[b]	$E_b(M_2)$[c]
Regular, O^{2-}	Cu	102	93 [d]	66	75
			102 [e]	*74* [e]	*65* [e]
			85 [f]	*69* [f]	*93* [f]
	Ag	81	46 [d]	40	74
			51 [g]	*58* [h]	*88* [g]
	Au	110	96 [d]	82	96
			87 [g]	*82* [h]	*105* [g]
F_s	Cu	102	189 [i]	107	69
			182 [e]	*111* [e]	*66* [e]
	Ag	81	178 [i]	107	76
			174 [g]	*122* [h]	*90* [g]
	Au	110	311 [i]	196	102
			301 [g]	*191* [h]	*107* [g]
F_s^+	Cu	102	242 [i]	66	1
	Ag	81	229 [i]	64	8
	Au	110	358 [i]	116	–2

[a] EPE results given by plain numbers; values from the literature in italics.

[b] $E_{ad}(M_2) = [E(MgO_{site}) + E(M_2, \text{free}) - E(M_2/MgO_{site}) + \Delta E(\text{BSSE})] / 2$

$= E_{ad}(M_2) + D_e(\text{M-M})/2 - [E_{ad}(M_1/MgO_{reg}) + E_{ad}(M_1/MgO_{site})] / 2.$

[c] Dissociation energy with one atom adsorbed at a regular surface site. $E_b = [E(M_1/MgO_{reg}) + E(M_1/MgO_{site}) - E(M_2/MgO_{site}) - E(MgO_{site}) + \Delta E'(\text{BSSE})] / 2.$

[d] Ref. 38. [e] Ref. 43. [f] Refs. 45, 46. [g] Ref 148. [h] Inferred from Ref. 148, using D_e(Ag-Ag)/2 = 81 kJ mol^{-1} and D_e(Au-Au)/2 = 110 kJ mol^{-1} (present work, Table 3.6).

[i] Ref. 37.

distributed more or less uniformly over both atoms with the charge on the closest to the substrate metal atom being -0.51, -0.52 and -0.36 *e* for Cu_2, Ag_2, and Au_2, respectively.

Adsorption on a charged vacancy, F_s^+, is described by the same type of electron interaction as discussed for the F_s site. However, the stabilization energy is smaller because the vacancy orbital is now occupied by only one electron instead of two. Binding energies collected in Table 3.10 are uniformly 60% of those at the neutral F_s site, so that for Cu_2, the adsorption energy becomes essentially equal to

that on a regular O^{2-} site. Concomitantly, the bond lengths M-M decrease slightly, by 1–3 pm, and M-Mg distances increase by 4–6 pm, compared to adsorption complexes on F_s centers (Table 3.9 and Table 3.10). Cu_2 and Au_2 adsorbed on an F_s^+ site assume essentially an upright position with respect to the surface plane whereas Ag_2 is noticeably tilted, 29° with respect to the surface normal. Partial charge delocalization of the vacancy electron density towards the metal species also takes place in adsorption complexes at F_s^+ sites. The net PDC charges on adsorbed dimers are -0.47, -0.37, and -0.37 *e* on Cu_2, Ag_2, and Au_2, respectively. This is about half as much as calculated for adsorption on neutral vacancies. (The corresponding Mulliken charges are -0.27, -0.17, and -0.66 *e* on Cu_2, Ag_2, and Au_2, respectively.). Furthermore, the charge is now mostly localized on the metal atom closest to the substrate.

Finally, we comment on the question whether indeed oxygen vacancies are stronger attractors for nucleation than regular sites. Previous studies [43,45,46,148] indicated that Cu_2 adsorbed on regular and various defect sites of MgO is stable with respect to dissociation on the surface. In addition, it has been demonstrated that the propensity for dimerization on neutral F_s sites is virtually the same as on regular O^{2-} sites [43,148]. The stability of a dimer M_2 adsorbed at any (defect or regular) *site* under scrutiny (M_2/MgO_{site}) with respect to two adatoms M, one of them bound to this site (M_1/MgO_{site}) and the other attached to a *regular* terrace O^{2-} site (M_1/MgO_{reg}), is characterized by the following *dimer dissociation energy on a surface site* (per atom) [43]:

$$E_b = [E_{(M1/MgOreg)} + E_{(M1/MgOsite)} - E_{(M2/MgOsite)} - E_{(MgOsite)} + \Delta E'(BSSE)] / 2. \qquad (3.2)$$

From Table 3.11, one sees that on regular surface sites E_b is 74–96 kJ mol^{-1}/atom, slightly larger for Au_2 than for Ag_2 and Cu_2. These values are not much below the gas phase values, D_e(M-M)/2. The dimer dissociation energies on F_s sites are very close to those on regular sites. Literature values for Cu_2 [43] as well as Ag_2 and Au_2 [148] on regular and F_s sites differ by at most 19 kJ mol^{-1}/atom from our results. Moreover, on charged vacancies, F_s^+, the tendency to dimerize is virtually negligible, because open-shell F_s^+ sites interact significantly stronger with open-

shell monatomic Cu, Ag, and Au than with the corresponding closed-shell dimers. Thus, one may speculate that initial cluster growth could occur via migration of dimers to monatomic species nucleated at F_s^+ centers.

3.3.4 Conclusions

We have studied in this section the adsorption of homo-atomic dimers and trimers of all three coinage metals on a defect-free MgO(001). We have identified most favorable adsorption geometries and compared the three congeners of the Cu subgroup. The interaction of dimers and trimers with regular O^{2-} surface sites is mainly due to weak atomic polarization (somewhat stronger in the case of Au_2), counteracted by Pauli repulsion, just as concluded earlier for adsorption of single atoms [26,30]. The most stable geometries were found to be similar to those in the gas phase with the metal particle in upright orientation with respect to the surface. The effective adsorption energy per atom decreases from dimers to trimers by 7, 12, and 22% for Cu, Ag, and Au, respectively. Our results for adsorbed Cu_2 and Cu_3 essentially agree with the results of the periodic slab model calculations, where a different gradient-corrected exchange-correlation functional had been used. For the adsorption of Cu_3, we found two additional low-lying minima with energies about 10 kJ mol^{-1} higher than the lowest-energy complex; one of these additional complexes corresponds to the $^2A_1$ excited state of gas-phase Cu_3.

Binding to oxygen vacancies, to F_s sites in particular, is notably stronger than to regular O^{2-} sites, for two reasons. Pauli repulsion is reduced and the electron density of the adsorbate as well as that of a vacancy are easier to polarize. Furthermore, at neutral defect sites, a notable transfer of electron density from the vacancy to the adsorbed metal species contributes to stronger binding. The frequencies of the M-M stretching vibrations are significantly reduced in the adsorbed species on F_s and F_s^+ sites, compared to gas-phase values, by 31–37%, and by 10–24% compared to dimers adsorbed on regular sites. The adsorption energies of Ag_2 and Au_2 are about 50% larger on an F_s^+ site than on a regular O^{2-} site, whereas for Cu_2, adsorption on F_s^+ and O^{2-} sites is almost isoenergetic. Adsorption

on a neutral F_s site is 60–70% stronger for all three dimers than on a charged defect site F_s^+.

Based on calculated interaction energies, we conclude (in qualitative agreement with previous findings) that dimerization of adsorbed coinage atoms on F_s sites is not particularly favored compared to dimerization on flat terraces. Dimerization on F_s^+ sites, which has not been considered theoretically before, is clearly unfavorable. In general, cluster growth is a complicated phenomenon; it is significantly affected by the type of metal as well as of the type of sites on the oxide surface involved in the very first stage of the metal nucleation on supports. Therefore, high-level electronic structure calculations of adequate models are of special importance for providing and unraveling (often unique) information on the surface-mediated metal dimerization and trimerziation processes.

3.4 Adsorption of Cu_4, Ag_4 and Au_4 particles on the regular MgO(001) surface

3.4.1 Introduction

In this section we theoretically quantify parameters of coinage metal aggregates M_4 (M = Cu, Ag, Au) adsorbed on regular sites of the MgO(001) surface. This study aims to identify preferred adsorption sites and geometries of deposited metal tetramers, to explore the nature of the metal-support bonding, and to quantify adsorption energies. The present section complements our study of coinage metal dimers and trimers on Mg(001) [39] (see Section 3.3).

3.4.2 Computational details

Calculations were performed at the all-electron level using the LCGTO-FF-DF method [150] implemented in the parallel computer code *ParaGauss* [151,152]. We employed the gradient-corrected exchange-correlation functional BP86 [139,153]. In calculations involving 4*d*- (Ag) and 5*d*-atoms (Au), we used a scalar relativistic variant based on a second-order Douglas-Kroll transformation to decouple electronic and positronic degrees of freedom of the Dirac-Kohn-Sham equation [156,185]. The Gaussian-type atomic orbital basis sets, contracted in generalized fashion – Cu $(15s11p6d) \rightarrow [6s5p3d]$, Ag $(18s13p9d) \rightarrow [7s6p4d]$, Au $(21s17p11d7f) \rightarrow [9s8p6d4f]$, Mg $(15s10p1d) \rightarrow [6s5p1d]$, O $(13s8p1d) \rightarrow [6s5p1d]$ – were the same as in our previous work [37–39]. The auxiliary basis set utilized in the LCGTO-FF-DF method to represent the electron charge density for treating the Hartree part of the electron-electron interaction was constructed by properly scaling the s and p exponents of the orbital basis sets [150]; "polarization exponents" were added as geometric series with factors 2.5, starting with 0.1 for p and 0.2 for d exponents [150]. The resulting auxiliary basis sets were: Mg(15*s*,10r^2,5*p*,5*d*), O(13*s*,4r^2,5*p*,5*d*), Cu(15*s*,11r^2,5*p*,5*d*), Ag(18*s*,13r^2,5*p*,5*d*), Au(20*s*,17r^2,5*p*,5*d*).

Cluster models of the MgO substrate were embedded in an elastic polarizable environment (EPE) [34]. A specially designed QM/MM interface ensures a consistent description of the mutual influence of electronic and geometric changes of the QM cluster region and its environment relative to the regular unperturbed surface [34]. We employed a $Mg_9O_9(Mg^{pp*})_{12}$ cluster as QM part of the system, modeling the regular MgO(001) surface. Here, Mg^{pp*} labels pseudopotential centers Mg^{2+}, entirely without electrons, which saturate the coordination spheres of O anions at the cluster boundaries [149]. To generate the environment of the QM part, we optimized a two-layer slab model of the MgO(001) surface at the classical MM level. Our tests showed differences of only 1 pm for metal-MgO distances and 2 kJ mol^{-1} for the binding energies [39] compared to the results of our six-layer slab model [37,38].

Adsorption energies, E_{ad}, were calculated with respect to the sum of the corresponding spin-polarized ground-state energy of a free metal species M_4 in its equilibrium geometry, and the energy of the relaxed MgO(001) model cluster. The E_{ad} values were corrected for the basis set superposition error (BSSE) by invoking the counterpoise method [159].

3.4.3 Results and discussion

A. Free coinage metal tetramers

The geometries of the tetramers Cu_4, Ag_4 and Au_4 in the gas phase were optimized in either tetrahedral (T_d) or planar rhombus (C_{2v}) arrangement. In all cases, the latter structure was found favorable (Table 3.12), in agreement with earlier calculations, e.g. [43,45,46,194,195,197–200]. The T_d conformations of free Cu_4, Ag_4 and Au_4 species are less stable by 101, 92 and 110 kJ mol^{-1}, respectively, than the corresponding C_{2v} structures. For both the C_{2v} and T_d tetramers, close-shell ground states are stabilized with respect to the corresponding triplet states by ~60 kJ mol^{-1} (C_{2v}) and 90–110 kJ mol^{-1} (T_d). In the most stable configurations of the M_4 moieties, the M-M distances along the edges of the rhombus are very similar to those of the short diagonal; hence, the M_3 units are almost equilateral.

Table 3.12. Calculated bond lengths r_e(M–M) [a] and dissociation energies per atom $D_e/4$ of gas phase tetramers M_4 (M = Cu, Ag, Au) in the most stable rhombic structure.

M_4	State	Study	r_e(M–M), pm	$D_e/4$, kJ mol^{-1}
Cu_4	$^1A_1$	this work	239 (228)	146
		literature	232 [b], 230 [c], 245 [e]	148 [b], 147 [c], 153 [d], 126 [e]
	$^3A_2$	this work	234 (261)	131
Ag_4	$^1A_1$	this work	274 (262)	107
		literature	258 [f]	128 [f]
	$^3A_2$	this work	269 (309)	92
Au_4	$^1A_1$	this work	268 (263)	146
		literature	270 [g]	168 [h]
	$^3A_2$	this work	264 (311)	130

[a] The short diagonal interatomic distance of the rhombus is shown in parentheses.

[b] Ref. [45]. [c] Ref. [200]. [d] Ref. [191]. [e] Ref. [43]. [f] Ref. [195]. [g] Ref. [194].

The calculated dissociation energy of Cu_4 species per atom, 146 kJ mol^{-1}, is higher than the corresponding energies for the Cu dimer, 102 kJ mol^{-1}, and trimer, 112 kJ mol^{-1} [39], in accordance with other calculations [43]; the same trend is also found for Ag and Au analogs. The dissociation energy of Ag_4 is calculated at 107 kJ mol^{-1}/atom; the corresponding edge length, 274 pm, is somewhat longer than in a previous study [197]. There, the dissociation energy is also higher, by 21 kJ mol^{-1}/atom. The dissociation energy of Au_4 is essentially the same as of Cu_4 (Table 3.12) and 39 kJ mol^{-1}/atom larger than that for Ag_4. Thus, the first- (Cu) and third-row (Au) elements exhibit substantially stronger binding in the tetramers than the second-row element Ag. This trend, also noticed for coinage atom dimers and trimers [39], can be rationalized as follows. The M-M interactions in the Ag_4 moiety are weaker than in Cu_4 because of the larger size of the silver atoms and a destabilization of the Ag 5s compared to the Cu 4s orbital; the relativistic contraction of the Au 6s shell restores stronger M-M interactions between the gold atoms.

B. Adsorption of tetramers on a regular MgO(001)

We considered three different orientations of the coinage metal tetramers with respect to the MgO(001) surface: two upright geometries, where the rhombus is attached to the substrate by two (Figure 3.6, mode A) or one atom M (mode B) and a moiety lying parallel to the surface (mode C). Throughout, C_s point group symmetry constraints were imposed. The calculated observables for the optimized adsorption complexes are collected in Table 3.13.

An upright geometry of supported Cu_4 species, with two Cu atoms coordinated to two O anions (mode A), is most stable. The rhombus Cu_4 is slightly distorted, with edges of 257, 232, 235 and 243 pm; the short diagonal is 234 pm. The largest distortion compared to the gas phase (from 239 to 257 pm, Table 3.12 and 3.13) occurs on the edge which directly contacts the surface anions. This elongation of the Cu–Cu bond can be attributed to the significant lattice mismatch between the MgO surface and Cu (Ag, Au) particles: the nearest O–O distance in the substrate, 299 pm (optimized with EPE approach compared to the experimental distance of 298 pm for the bulk), is notably longer than M–M distances in any of the coinage metal tetramers under scrutiny. Two bonds formed by Cu_4 with the O anions are 196 pm (central O in the Mg_9O_9 cluster) and 205 pm (the nearby O anion). The adsorption energy of this complex is calculated at 191 kJ mol^{-1}. These data are very close to those of Musolino *et al.* [46], obtained with the Car-Parrinello approach and the PW91 xc functional for adsorption mode A: edge lengths of 257, 234, 237, and 242 pm, Cu–O distances of 201 and 207 pm, and an adsorption energy of 184 kJ mol^{-1}. Recently, Del Vitto *et al.* [43] reported similar geometries for Cu_4 adsorbed on MgO using the hybrid B3LYP functional: 264 and 235 pm for edges and 230 pm for the short diagonal. The corresponding adsorption energy, 220 kJ mol^{-1}, is somewhat larger than the present BP86 value, probably because no BSSE correction was applied [43].

Adsorption mode B, where Cu_4 is attached to the surface via a single metal atom, is 44 kJ mol^{-1} less stable than mode A. The Cu–O bond length is 190 pm and the Cu–Cu distance in the upright direction is 229 pm. This structure is very similar to the upright orientation of the Cu_2 moiety on MgO(001) [39], which featured 192

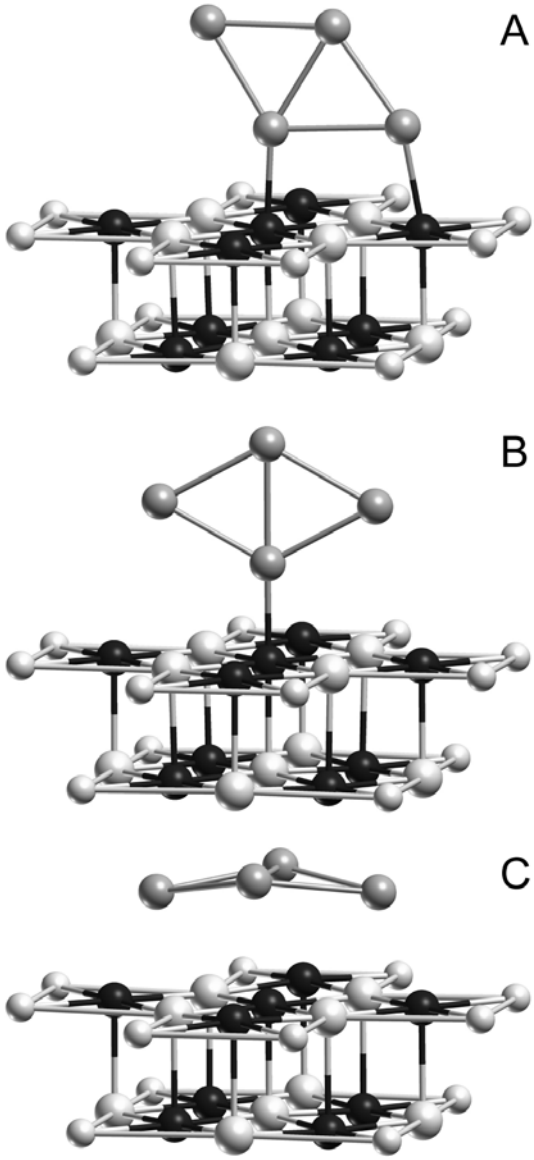

Figure 3.6. Sketches of three modes of M_4 (M = Cu, Ag, or Au) species adsorbed on the regular MgO(001) surface. Black, large white, small white, and light gray spheres indicate O, Mg, Mg^{pp*}, and M atoms, respectively.

pm for Cu–O and 226 pm for Cu–Cu. Earlier calculations [46] yielded a shape of adsorbed Cu_4 similar to our mode B.

In mode C, Cu_4 is oriented parallel to the MgO(001) surface with an average height of 212 pm. As shown in Figure 3.6, mode C, the planarity of the adsorbate is slightly distorted due to interactions with the oxide substrate. This structure exhibits significantly longer Cu–O distances than modes A and B: two Cu atoms are bound to the central O anion (279 pm) and the other two Cu atoms form pair-wise contacts

Table 3.13. Calculated properties [a] of the adsorption complexes M_4/MgO(001), M = Cu, Ag, Au.

	M	Mode A	Mode B	Mode C
r(M–M)	Cu	232, 235, 243, 257 234 [b]	239 (×4) 229 [b]	247 (×2), 248 (×2) 227 [b]
	Ag	264, 268, 281, 288 268 [b]	272 (×2), 276 (×2) 264 [b]	276 (×4) 269 [b]
	Au	256, 260, 272, 301 278 [b]	265 (×2), 277 (×2) 260 [b]	271 (×4) 269 [b]
∠M-M-M	Cu	57, 58, 119, 126	57 (×2), 123 (×2)	56 (×2), 124 (×2)
	Ag	58 (×2), 120, 124	58 (×2), 121, 124	58 (×2), 122 (×2)
	Au	59, 63, 113, 125	57 (×2), 118, 128	60 (×2), 120 (×2)
r(M–O)	Cu	196, 205	190, 316, 317	279 (×2), 306, 312
	Ag	227, 232	225, 364 (×2)	275, 276 (×3), 297 (×2)
	Au	220, 222	216, 362 (×2)	277, 280, 294 (×2), 296 (×2)
r(M–Mg)	Cu	282 (×2), 289 (×2), 297 (×2)	289 (×4)	273 (×2), 277 (×2)
	Ag	307 (×2), 308(×2), 319 (×2), 326 (×2)	312 (×4)	304 (×2), 305 (×2), 320 (×4)
	Au	294 (×2), 297 (×2)	307 (×2), 310 (×2)	303 (×4), 319 (×2), 320 (×2)
E_{ad}	Cu	191	147	84
	Ag	112	96	58
	Au	216	158	66

[a] Interatomic distances in pm, angles in degree, adsorption energies in kJ mol^{-1}.

[b] The fifth M-M distance is the short diagonal of the (distorted) rhombus M_4.

with the next-nearest neighboring anions, at 306 and 312 pm. All these distances are too long to be referred to as real "bonds". Apparently, mode C is not optimal for efficient interactions with surface anions, which is consistent with the rather low computed adsorption energy, 84 kJ mol^{-1} only. The latter value is about twice larger than a previously reported value, 44 kJ mol^{-1} [201], where C_{4v} symmetry was

imposed (implying a "lying" square rather than an upright rhombic geometry) in combination with embedding in a mere array of point charges. After lowering the symmetry and employing an advanced EPE embedding [34] in the present work, the cluster gained ~40 kJ mol^{-1} in adsorption energy. Note that in Ref. 201 the complex reminiscent of mode C exhibited a triplet electronic state, whereas a closed-shell complex is presently found. According to periodic calculations [45], not perfectly planar Cu_4 lies ~214 pm above the MgO(001) surface and the adsorption energy 88 kJ mol^{-1} almost coincides with the value obtained here.

The adsorption complexes of Ag_4 and Au_4 (Table 3.13) are quite similar to the Cu_4 complex considered above in detail. Mode A is most stable, closely followed by mode B, whereas mode C clearly exhibits the weakest binding to the surface. Ag and Au atoms are larger than Cu, but not large enough to compensate the considerable mismatch between the nearest-neighbor distance of the MgO(001) surface and optimum M–M distances in supported Ag_n and Au_n species.

Similar to single metal atoms [26,30,38] as well as dimers and trimers [39], Ag_4 tetramers form the weakest bond with the MgO(001) surface among the coinage metal analogs. For the most stable adsorption mode A, the edge Ag–Ag distances are 268, 264, 281, 288 pm and the short diagonal of the (distorted) Ag_4 rhombus is 268 pm, deviating only slightly from the gas phase value. Ag_4 binds via its two Ag atoms to the central and nearby O anions, with bond lengths of 227 and 232 pm, respectively. The calculated adsorption energy is 112 kJ mol^{-1}. For mode B, with an Ag_4 rhombus attached to the surface via a single Ag atom, the adsorption energy is smaller, but only by 16 kJ mol^{-1}; the Ag–O distance is 225 pm. In the same way as for Cu, mode C is again least stable, with a binding energy of 58 kJ mol^{-1}. In the previous study [40], where only modes B and C were considered, cluster models of the substrate were embedded in a large array of point charges. This resulted in calculated adsorption energies of 76 and 48 kJ mol^{-1}, respectively. Thus, application of the EPE approach [34] to the Ag_4/MgO(001) system, which represents a very weakly bound case, increases the adsorption energy by 10–20 kJ mol^{-1}.

For adsorption of a Au_4 moiety on MgO(001), no previous information was available neither from theoretical nor experimental studies. Similarly to the Cu_4 and Ag_4 systems, mode A is most stable, with an adsorption energy of 216 kJ mol^{-1}, while modes B and C are less stable by 58 and 150 kJ mol^{-1}, respectively (Table 3.13). For mode A, the edge Au–Au distances are 301, 256, 260, and 272 pm, with a short diagonal distance of 278 pm. The Au–O distances to the central and nearby surface O anions are 220 and 222 pm, respectively.

Comparing the adsorption energies of the three tetramers, we find that the Au_4 species in the most favorable configuration binds to the oxide surface stronger than the Cu_4 and Ag_4 analogs do, in agreement with our findings for dimers and trimers of these elements supported on MgO(001) [39]. We also conclude that for all three elements the adsorption energy per atom decreases when increasing the size of metal particles (in kJ mol^{-1}): Cu (66 dimer, 61 trimer, 48 tetramer), Ag (40, 35, 28) and Au (82, 64, 54). This is not surprising since only two atoms of M_4 particles actually participate in bonding to the surface while the adsorption energy per atom is divided by four. If we compare the consistent adsorption modes, where the dimer, trimer and tetramer are bound to the surface via a single atom M (mode C for dimers and trimers of Ref. 39 and mode B for tetramers of the present study), we see that the total adsorption energies for species with different number of metal atoms are rather similar (in kJ mol^{-1}): Cu (132 dimer, 153 trimer, 147 tetramer), Ag (80, 90, 96), Au (162, 168, 158). The most stable adsorption complex of trimers (mode B [39]) also binds to the MgO(001) surface by two metal atoms and therefore it is comparable to the mode A of tetramers if the adsorption energy is calculated per *interacting* metal atom, i.e. per two atoms in this case (in kJ mol^{-1}): Cu (92 trimer, 96 tetramer), Ag (53, 56), Au (96, 108). This analysis shows that similar adsorption modes of dimers, trimers and tetramers yield similar adsorption energies.

By combining the present results with those of the previous systematic studies on metal atoms, dimers, and trimers on MgO [37–39] (see Section 3.1–3.3), we can estimate the propensity of small deposited aggregates to coalesce to tetramers. The reactions $2M_2(ad) \rightarrow M_4(ad)$ are accompanied by energy gains of

103 (Cu), 56 (Ag), and 32 kJ mol^{-1} (Au). These values are notably smaller than the reaction energies for the corresponding metal particles in the gas phase, 172, 103, and 143 kJ mol^{-1}. Thus, the substrate counteracts sintering in a significant fashion, despite that two adsorbed dimers together have the same number of M–O bonds (two) as an adsorbed tetramer. The reactions $M_3(ad) + M_1(ad) \rightarrow M_4(ad)$, resulting in a change from two open-shell "reactants" to a closed-shell "product", are more favorable than the dimerization of adsorbed dimers, despite that one relatively strong M–O bond is lost. The energy gains are 163, 146, and 164 kJ mol^{-1}, for Cu, Ag and Au respectively. The recombination of trimers with single atoms in the gas phase again in even higher energy gains of 246 (Cu), 186 (Ag) and 235 kJ mol^{-1} (Au), because pairing of electrons yields a strong bond between the two moieties without the expense of destabilizing a moderately strong bond with the support.

Concerning the character of the metal-oxide bond, it was shown already for single coinage metal atoms that the driving force of their interaction with the regular MgO(001) is polarization of electronic shells of metal species by the electrostatic field of ionic substrate [26,30]. The upright orientation of the coinage dimers, trimers and tetramers adsorbed on MgO(001) also indicates that the interaction is dominated by polarization contributions. Evidently, the upright orientation enhances polarization of cluster orbitals compared to the structure where metal species is parallel to the surface. As polarization effects are weak, the structure of the coinage metal tetramers is only slightly affected by adsorption. Indeed, for each element under study, the energy per adsorption bond (~100 kJ mol^{-1} for Cu_4 and Au_4, and 56 kJ mol^{-1} for Ag_4) is about 40–50 kJ mol^{-1} smaller than the binding energy of a metal atom in the corresponding tetramer in the gas phase (146 kJ mol^{-1} for Cu and Au, 107 kJ mol^{-1} for Ag). Taking into account the significant lattice mismatch between MgO(001) and coinage metals (not only different interatomic distance, but different lattice symmetries as well), one can hardly expect any ordering of adsorbed coinage metal species on MgO(001). The above trends are clearly manifested already for particles of 3–4 atoms and one can expect that consideration of larger deposited coinage species will not bring much new information regarding the adsorption peculiarities on the *regular* (defect free) terraces of the MgO support. However,

point or extended defects, resulting in considerably enhanced interactions with the oxide support [37], will be particularly important for parameters of small deposited metal particles.

3.4.4 Conclusions

In the present section, the adsorption properties of Cu_4, Ag_4 and Au_4 clusters deposited at the regular MgO(001) surface were characterized by means of density functional approach using accurately embedded cluster models. In the gas phase, all three tetramers were calculated to exhibit a planar rhombic structure with a closed electronic shell. Geometries of the supported tetramers were found to be similar to those in the gas phase, i.e. the rhombus structure experiences only minor distortions due to interactions with the surface. All three tetramers favor the same adsorption mode, namely an upright orientation of the metal particle, perpendicular to the surface, with two metal centers attached to the surface oxygen anions. Such an upright adsorption mode has already been obtained for coinage dimers and trimers on MgO(001) [39] (Section 3.3) and rationalized by the fact that the interaction of coinage metal particles on regular sites of the ionic oxide is primarily of polarization character. Our results for adsorbed Cu_4 essentially agree with the results of periodic slab model DF calculations [45,46]. Similarly to the dimer and trimer complexes, Au_4 exhibits the strongest adsorption on MgO(001), followed by Cu_4 and Ag_4. The significant lattice mismatch between the MgO(001) surface and the metal particles appears to be an important factor for governing the adsorption mode (and orientation) of the latter. Because interaction with the surface is weaker than interatomic interactions within the metal species, the morphology of the coinage metal particle remains unchanged under adsorption at a defect-free MgO(001) surface. The propensity of small supported metal particles to dimerize, giving adsorbed tetramers, has been quantified and rationalized.

Chapter 4

Studies of Metal Nanoparticles Relevant to Catalysis

4.1 Adsorption of carbon on Pd clusters of nanometer size

4.1.1 Introduction

During the catalytic conversion of organic molecules, often atomic carbon moieties are generated and deposited on transition metal particles as impurities, affecting the performance of a catalyst or even poisoning it. For instance, the decomposition of methanol via the C–O bond breaking channel on an oxygen precovered Pd(110) single-crystal surface [202] and on supported ordered palladium nanoparticles [54] leads to the formation of adsorbed carbon. Recently, it was concluded that carbon (and accompanying hydrocarbon CH_x) species preferentially block defect sites, such as particle edges and steps [54], of ordered Pd crystallites which had been grown on alumina films and exhibited a well-faceted truncated *fcc* structure with a large fraction of (111) facets [203–205].These findings imply a propensity of C (and/or

CH_x) to form stronger bonds with sites located in the vicinity of edges than at regular sites of interior terrace regions of Pd nanoparticles.

Atoms of light elements, e.g., C, O, and H, appear to be sufficiently small so that, under certain experimental conditions, they even are able to penetrate into the subsurface region of transition metal samples and preferentially occupy interstitial positions, e.g., between the two outmost layers of metal atoms. Previously, the problem of subsurface light-element atoms on Pd had been addressed in a computational study [206]; there it was found that migration of surface H and C atoms located on threefold hollow sites of Pd nanoparticles into the underlying interstitial subsurface positions is thermodynamically and kinetically feasible, whereas O or N atoms prefer sites at the surface. For carbon this trend to occupy subsurface sites is even somewhat stronger than for atomic hydrogen, when octahedral interstitial sites are considered, but hydrogen may also occupy tetrahedral sites. Therefore, higher impurity concentrations can be obtained for H/Pd than for C/Pd [206].

To the best of our knowledge, up to recently there was no high-level theoretical investigations reported on details of the adsorption bonding of atomic C on various sites exposed by Pd nanoparticles representing so-called “model catalysts” [1,16] (see Chapter 2). These particles are prepared in the form of ordered well-characterized nanosize clusters on thin-film alumina (and other oxide) supports in a controlled fashion [1,16]. In this way, the complexity of such model catalysts is significantly reduced compared to real (industrially used) catalysts, but the diversity of the exposed active surface sites remains essentially unchanged.

Our present first-principles DF study aimed at quantifying computationally various observables of adsorption complexes of atomic carbon on a broad range of surface sites which are featured by well-ordered Pd nanoparticles that contain about 50–150 metal atoms and have diameters of 1–2 nm [55]. We characterized for the first time C–Pd interactions for a series of conceivable adsorption sites structurally, energetically, and with regard to the adsorbate-substrate charge rearrangement. In the following, we report these results and we discuss implications for the diffusion properties of C species on Pd nanoclusters as well as for the above mentioned

experimental results on blocked active sites in the catalytic reaction of methanol decomposition [54]. Furthermore, we also outline here the consequences of the deposition of C atoms on the adsorption properties and reactivity of the metal nanoparticles. This was probed by co-adsorption of CO molecules.

A central aspect of the work described in this section is that it is based on the recently proposed strategy to model both extended metal surfaces [62] and surface irregularities such as edge, step and kink sites [61] in the frameworks of a cluster approach, relying on three-dimensional symmetric nanoparticles which are terminated by low-index surfaces. It was demonstrated that in the case of a moderately strongly bound CO probe such cluster models of already ~80 Pd atoms describe various adsorption properties of the Pd(111) surface (including the adsorption energy) in quantitative fashion [62]. With this strategy, it was possible to unravel bonding and vibrations of CO molecules adsorbed at Pd [61,62] and PdZn [56] nanoclusters and to clarify the location of light atom elements in the subsurface region of Pd nanoparticles [206]. It remained to be validated that Pd nanoclusters of that shape and nuclearity range also allow one to reach size convergence for all calculated adsorption parameters, including such a delicate observable as the adsorption energy, even for very strongly adsorbed C species. This will be successfully shown in the following, thus extending the application area of the novel computational strategy to investigate surface properties of transition metal single-crystal and polycrystalline materials by employing three-dimensional cluster models.

Another important extension of the computational strategy based on nanocluster models is used here for the first time, namely, a reduction of the cluster symmetry from O_h to that of the point group D_{4h}. The demonstrated feasibility of such reduced-symmetry calculations of adsorption complexes on the nanosize clusters opens the opportunity to investigate less symmetric adsorbates, more general adsorption sites, and a decreased surface coverage. The capability to treat nanoclusters under reduced symmetry is a crucial prerequisite for modeling chemical reactions on metal catalysts with the present cluster strategy, where in

general adsorption complexes have to be modeled without any *local* symmetry constraint.

The section is organized as follows. In Subsection 4.1.2 we outline (4.1.2 A) our computational procedure and describe (4.1.2 B) the cluster models employed. The results are presented in Subsection 4.1.3. We discuss (4.1.3 A) cluster size effects on adsorption properties of the Pd(111) surface, calculated for strongly bound C species on models with bulk-terminated and relaxed geometry. We describe (4.1.3 B) the site dependence of the structure, chemical bonding, and energetics for C adsorbates on the high-symmetry O_h substrate cluster Pd_{140}. Furthermore, we present (4.1.3 C) the same adsorption parameters of C, but calculated on the D_{4h} cluster Pd_{116}; with these data, we delineate the most favorable adsorption positions of atomic carbon moieties on Pd nanoparticles and we discuss the experimentally derived models for C blocking of particular sites on Pd model catalyst particles. Subsection 4.1.4 is devoted to the influence of C deposits on octahedral Pd_{140} moiety on the co-adsorption of probe CO molecules [225]. Finally, in Subsection 4.1.5, we summarize our results and give a brief outlook on modeling the reactivity of supported transition metal catalysts.

4.1.2 Computational details and models

A. Method of calculations

The calculations were performed at the all-electron level using the LCGTO-FF-DF method [150] as implemented in the parallel code PARAGAUSS [151,152]. We used the scalar relativistic variant of the LCGTO-FF-DF method which employs a second-order Douglas–Kroll transformation to decouple electronic and positronic degrees of freedom of the Dirac–Kohn–Sham equation [155,156]. Self-consistent solutions of the Kohn–Sham equations were obtained within the local density approximation (LDA; Vosko-Wilk-Nusair (VWN) parametrization [207]). Adsorption energies were determined by evaluating in a generalized-gradient approximation (GGA, using the Becke-Perdew 1986 (BP86) exchange-correlation functional [139,153]) for the self-consistent LDA electron density; this combined

computationally strategy is economic, yet sufficiently accurate [208]. In some cases, we also used the Perdue-Wang 1991 (PW91) [162] GGA functional for comparison.

As previously in calculations of our group [56,61,62,206], a (17*s*,11*p*,8*d*) Gaussian-type orbital basis set [209] for Pd was extended by one *s* (0.0135), two *p* (0.0904 and 0.0214), and one *d* (0.097) exponents; the final primitive basis set was contracted to [7*s*,6*p*,4*d*] using generalized contractions, based on relativistic VWN atomic eigenvectors. In the LCGTO-FF-DF method, the classical Coulomb contribution to the electron-electron interaction is evaluated by representing the electron density with the help of an auxiliary basis set [150]. The exponents for *s* and r^2 type functions of this "fit basis" were generated from the orbital basis by a standard procedure [150], we added five *p*- and *d*-type "polarization" exponents each which were chosen as geometric series with factor 2.5, starting at 0.1 and 0.2 a.u., respectively. For Pd, the auxiliary basis set was of the size (17*s*,6r^2,5*p*,5*d*). C and O atoms were described by the orbital basis set (14*s*,9*p*,4*d*) [210] using the original generalized contraction [6*s*,5*p*,2*d*] and by an auxiliary charge density basis set of the form (14*s*,9r^2,5*p*,5*d*) with the same polarization exponents as for Pd.

Spin averaging introduces only marginal errors for the structure and energetics of palladium nanosize clusters [211]. Already for Pd_{85}, this holds also for the cohesive energy, which is altered by merely 0.5 kJ mol^{-1} when spin-polarization is accounted for [211]. We found that spin polarization affects the adsorption energy of C on threefold hollow sites of a Pd_{85} cluster by less than 1 kJ mol^{-1}; an even smaller effect is expected for the adsorption on larger Pd clusters. Therefore, in the following, we will discuss only results for Pd_n and Pd_nC_m systems obtained in spin-restricted fashion. The C references in calculations of adsorption energies were always treated in spin-polarized fashion invoking the mean-field approximation where the two unpaired electrons are evenly distributed over the 2*p* shell; the same configuration has been also used in the comparative periodic calculations. The technique of fractional occupation numbers [150] (with a Gaussian level broadening of 0.1 eV) was applied for Pd_n and Pd_nC_m systems to ensure convergence of the self-consistent field process. In nanosize *d*-metal clusters such as those studied here, the Kohn–Sham levels commonly are so dense near the Fermi level that the typical

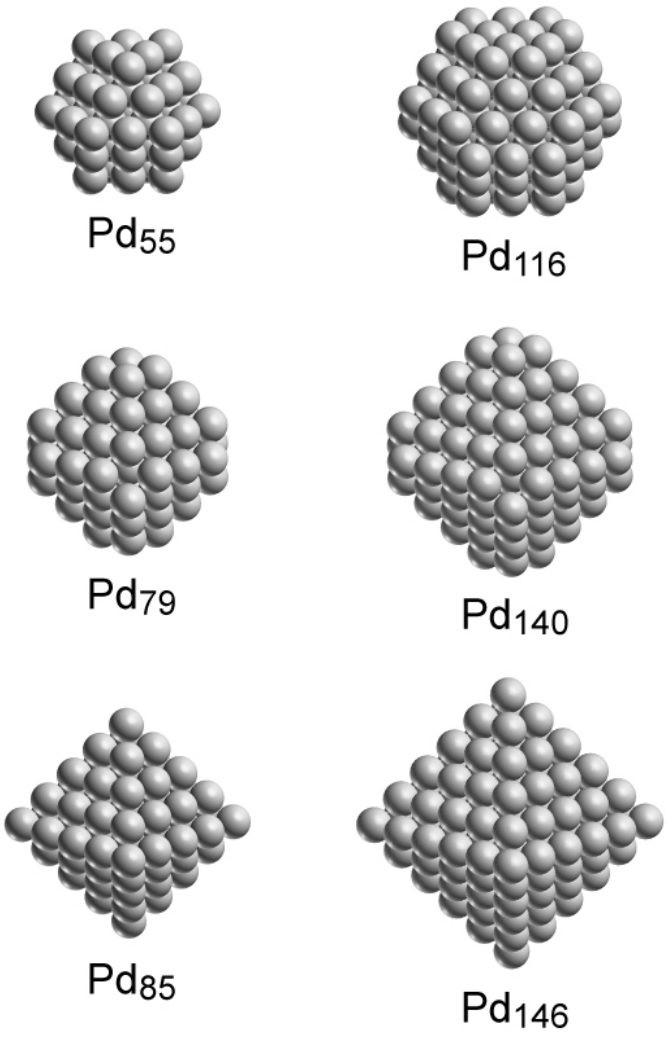

Figure 4.1. Sketches of the octahedral clusters Pd_{55}, Pd_{79}, Pd_{85}, Pd_{116}, Pd_{140}, and Pd_{146} selected to study the size sensitivity with respect to single C adsorption complexes at threefold hollow sites in the center of the (111) facets.

energy splitting is as small as 0.01 eV, less than the value of kT at room temperature. Thus, locating the proper ground state, defined by integer occupation numbers, becomes a formidable, if not futile task.

For nonoptimized Pd clusters, we used a bulk-terminated geometry with the experimental Pd–Pd distance of 275 pm [212]. When explicitly mentioned, geometry optimization of a bare Pd cluster (subject to O_h symmetry constraints) was performed at the LDA level, invoking a quasi-Newton algorithm and analytical forces [213,214]. While LDA yields realistic geometric (and vibrational spectroscopy) parameters, GGA in general is considered to improve energy values [189,215–217]. When probing adsorption properties, we kept the geometry of

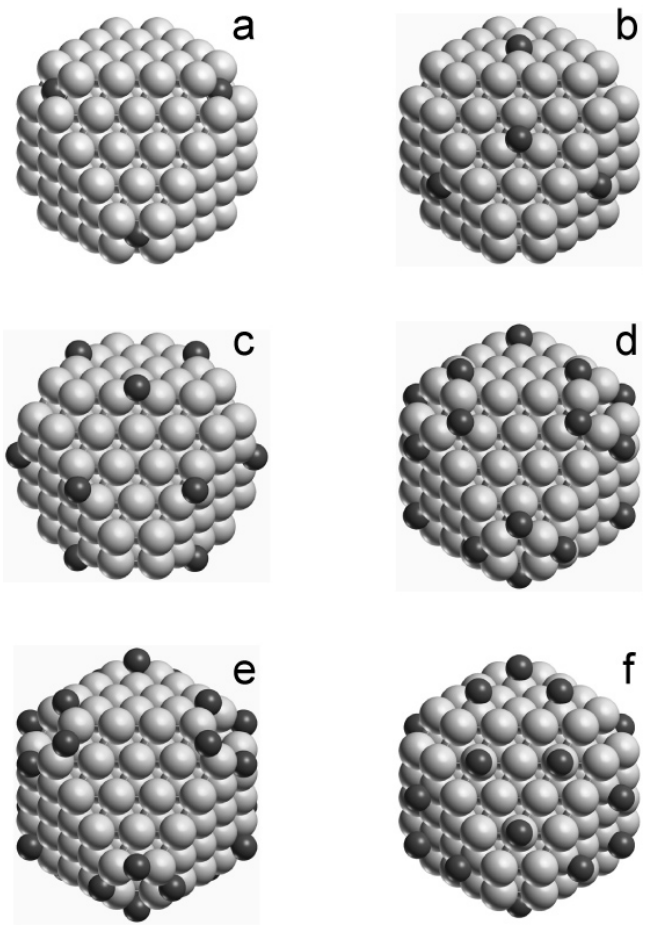

Figure 4.2. Sketches of the cluster Pd_{140} (O_h) with C atoms adsorbed in various positions (see Table 4.2): *a*, μ_4-C_6 on Pd(100) facets; *b*, μ_3-C_8 on Pd(111) facets; *c*, μ_2-C_{12} on Pd edge sites; *d*, μ_3-C_{24} on Pd(111) facets; *e*, μ_2-C_{24} on Pd(111) facets; *f*, on-top-C_{24} on Pd(111) facets.

Pd_n clusters fixed (with one exception, see below) and optimized only the height of adsorbed C atoms, positioned according to the symmetry groups O_h or D_{4h}. For that, Pd–C distances were varied until the changes were below 0.5 pm, using VWN energies. In a similar fashion, variation of Pd–C and C–O bond lengths of CO molecules, co-adsorbed with C atoms on Pd_{140} cluster have been performed in these calculations. The geometry of the C_n–Pd_{140} fragments was kept frozen, as optimized without the presence of CO (More details on calculations of adsorption complexes with CO can be found elsewhere [61,62]. We corrected the adsorption energy for the basis set superposition error (BSSE) via the counterpoise technique [159]. The BSSE corrections for the atomic C reference due to the presence of the basis set of the Pd substrate cluster ranged from 1.0 to 1.7 kJ mol^{-1}, depending on the method

(individual atom or symmetrized C_8 cluster); we approximated this correction by an average value of 1.5 kJ mol^{-1}. BSSE corrections to the energies of the Pd clusters brought by the flexible orbital basis sets of C adsorbates are more significant, of the order 20 kJ mol^{-1} per C atom. They were calculated for each C_m/Pd_n system in a straightforward symmetrized way, taking individual positions of the adsorbed C_m species into account. To characterize chemical bonding in the adsorption systems studied, we computed potential-derived charges that reproduce the electrostatic field outside the clusters [170]. Only the charges of adsorbates and Pd atoms constituting the outer two layers of the nanoclusters were used to fit the electrostatic potential that is determined essentially by the charge distribution of the surface part of the systems; the charges of the remaining atoms in the cluster core were set to zero.

B. Cluster models

A series of substrate clusters – Pd_{55}, Pd_{79}, Pd_{85}, Pd_{116}, Pd_{140}, and Pd_{146} (Figure 4.1) – , cut out from the *fcc* structure of bulk Pd by low-index planes, has been chosen to analyze the cluster-size sensitivity of the calculated observables. These nanoscale metal particles expose (111) and (100) facets along with the corresponding edge sites and exhibit diameters ranging from ~1.1 nm (Pd_{55}) to ~1.9 nm (Pd_{146}). In the electronic structure calculations of these highly symmetric (O_h) clusters, one has to deal with a rather moderate number of symmetry-nonequivalent Pd centers. Such three-dimensional clusters contain a significantly larger fraction of metal atoms with high coordination numbers compared to "planar" cluster models, commonly used in chemisorption studies [218,219]. Boundary metal atoms of such conventional cluster models (featuring artificially low coordination) are the source of inaccuracy in calculations of chemisorption complexes, whereas boundary atoms of the clusters studied in this work are described much more realistically [62].

The clusters Pd_{55}, Pd_{79}, and Pd_{85} exhibit a *fcc* adsorption site in the center of each of their eight (111) facets. Similarly, the clusters Pd_{116}, Pd_{140}, and Pd_{146} expose a *hcp* site in the center of their (111) facets. In the cluster-size convergence studies (Subsection 4.1.3 A), adsorbed C moieties were positioned over these central sites. This and other conceivable adsorption sites of atomic C were compared using the

substrate model Pd_{140} (Figure 4.2, Subsection 4.1.3 B). Finally, to scrutinize more general adsorption positions and to reduce the repulsion between coadsorbed C (which may occur if positions close to cluster edges are considered; Figure 4.3), we studied complexes on the substrate cluster Pd_{116}, relaxing the symmetry constraints according to point group D_{4h} (Subsection 4.1.3 C).

4.1.3 Clusters with deposited atomic carbon species

A. Cluster-size sensitivity of adsorption parameters

As already mentioned in Section 4.1.1, it has been demonstrated in CO adsorption studies on threefold hollow sites of Pd nanoclusters that "three-dimensional" models enable rather fast convergence of various adsorption parameters, including also the adsorption energy which has long escaped a reliable representation with cluster models. (Incidentally, the adsorption energy was calculated essentially equal for *fcc* and *hcp* surface CO species on Pd [62].) Moreover, those "converged" values accurately represent the corresponding properties of adsorption complexes on threefold hollow single-crystal Pd(111) sites of both *fcc* and *hcp* types as determined in periodic slab-model calculations [62]. Atomic C adsorbates are bound much stronger on Pd nanoclusters [206] than CO probes and they cause a more pronounced adsorbate-substrate rearrangement of the electron density [62]. The present subsection is mainly devoted to examining whether, as previously assumed [206], C adsorbates exhibit a similarly rapid cluster-size convergence as CO probes.

Table 4.1 presents the calculated results for adsorption complexes of C moieties, over the center of each of the eight (111) facets of the O_h clusters Pd_{55}, Pd_{79}, Pd_{85}, Pd_{116}, Pd_{140}, and Pd_{146}, considered in Pd bulk-terminated geometry.

One can immediately see that the optimized nearest-neighbor Pd–C distances are very stable for all adsorption complexes, 185.5±1.0 pm. [Note that on the basis of covalent radii (according to Pauling) of Pd, 128 pm, and of C, 77 pm, one estimates a much longer distance, r(Pd–C) = 205 pm.] The deviations induced by the cluster-size alteration are even a bit smaller than those previously calculated for CO molecules adsorbed on the same cluster surface sites [62]; this is in line with the

Table 4.1. Cluster-size dependence of calculated observables for complexes of eight C atoms adsorbed on three-fold hollow *fcc* or *hcp* sites (μ_3-C_8) in the center of the (111) facets of O_h Pd_n clusters with Pd–Pd distances fixed at the experimental value 275 pm for Pd bulk. r(Pd-C) – interatomic distances to the nearest neighbor Pd atoms optimized at the LDA-VWN level, z(C) – height of the atom C over the (111) facet, D_e – adsorption energy per C atom, evaluated for a GGA (BP86 or PW91) exchange-correlation functional with the VWN self-consistent electron density and corrected for the basis set superposition error (~10 kJ mol^{-1}).

	fcc			*hcp*		
	Pd_{55}	Pd_{79}	Pd_{85}	Pd_{116}	Pd_{140}	Pd_{146}
r(Pd-C), pm	184.7	186.5	185.5	185.0	185.5	185.5
z(C), pm	94.4	97.8	95.9	95.0	96.0	95.9
D_e(BP86), kJ mol^{-1}	624	639	635	657	636	632
D_e(PW91),[a] kJ mol^{-1}	643	658	655	677	657	651

[a] For comparison, PW91 adsorption energies of atomic C on a four-layer slab-model at 1/9 coverage were calculated in single-point fashion with r(Pd–C) = 185.5 pm and r(Pd–Pd) = 275 pm: 641 kJ mol^{-1} (*fcc*) and 648 kJ mol^{-1} (*hcp*). The corresponding values at 1/4 coverage were about 20 kJ mol^{-1} lower.

weaker Pd_n–CO bonding. Thus, calculated bond distances yield a first indication for the fast size convergence of adsorption parameters.

Most critical with regard to cluster-size convergence, however, is the behavior of computed binding (adsorption) energies. The adsorption energies per C atom for the most extended, thus likely most realistic, models *fcc* μ_3-C_8–Pd_{85} and *hcp* μ_3-C_8–Pd_{146} were calculated essentially equal (Table 4.1): 635 and 632 kJ mol^{-1} (BP86), 655 and 651 kJ mol^{-1} (PW91), respectively. The differences among the sites are 3–4 kJ mol^{-1}, i.e., less than chemical accuracy, often assumed to be 5 kJ mol^{-1}. Not unexpectedly [62,220], the PW91 adsorption energies are larger than the corresponding BP86 values. The next smaller members of the benchmark cluster series, *fcc* μ_3-C_8–Pd_{79} and *hcp* μ_3-C_8–Pd_{140}, exhibit adsorption energies that differ only insignificantly from the values of the former systems.

For CO, the complex on the central *fcc* site of the cluster model Pd_{55} was calculated to be considerably weaker bound (by more than 15%) compared to larger

models studied, indicating that the model Pd_{55} is not large enough to furnish reliably converged adsorption energies; the smallest model reaching convergence for *fcc* sites was Pd_{79} [62]. Similarly, we calculated a somewhat smaller adsorption energy for the *fcc* μ_3-C_8–Pd_{55} complex than for the Pd_{79} and Pd_{85} analog (Table 4.1). However, this energy decrease, only 10–15 kJ mol^{-1} or 2%, is much less (in relative terms) than it was for the CO complexes [62]. The C adsorption energy of the smallest model of *hcp* complexes, μ_3-C_8–Pd_{116}, is ~25 kJ mol^{-1} (or 4%) larger than that of the larger *hcp* models; this deviation is comparable with the corresponding energy increase for adsorbed CO on Pd_{116}, ~5 kJ mol^{-1} (or 3%) [62]. In general, the range of calculated adsorption energies for C species in Table 4.1, 640±17 kJ mol^{-1} (BP86) and ~660±17 kJ mol^{-1} (PW91), is sufficiently narrow to consider any of the substrate models as essentially converged, also regarding the adsorption energetics. Only when a particularly accurate energy values are required (anyhow a very difficult problem for various technical reasons of DF calculations, see, Ref.221), one may need to switch to larger models, Pd_{79} and Pd_{140}.

The next important question is, how accurate adsorption energies of C species on such converged cluster models (treated at bulk-terminated geometry) represent the adsorption energetics on regular sites of Pd single crystals, in our case *fcc* and *hcp* sites on Pd(111). For an answer, one may resort to results of periodic slab-model DF calculations of the C/Pd(111) system as reference [222,223]. For this comparison, we invoke results obtained with the xc functional PW91. (It is crucial to compare results obtained with the same xc functional [143].) For a coverage θ= 1/9, the adsorption energy on 3-fold sites was calculated (with *k*-points 5×5×1) to be almost equal: 641 kJ mol^{-1} (*fcc*) and 648 kJ mol^{-1} (*hcp*). (Note that at θ= 1/4 the lateral repulsion between adsorbed species reduces the calculated adsorption energy by ~20 kJ mol^{-1}.) Apparently, the adsorption energies of the present model cluster calculations are in good agreement with results of the slab-model calculations. This holds despite the fundamental methodological differences between the cluster code PARAGAUSS and codes imposing periodic boundary conditions; we mention in particular the all-electron scalar relativistic description based on localized basis functions in our method [155,156] and the plane-wave representation of orbitals in

the slab model calculations. Regarding predictions of experimental adsorption energies, which are unfortunately not yet available from the literature, one should note that the xc functional BP86 is also known to overestimate binding energies (although, in general to a smaller degree than the PW91 functional), whereas adsorption energies calculated with the more recently developed functional (PBEN) by Perdew-Becke-Ernzerhof, revised by Nørskov *et al.*, [154] are often more accurate [62,220].

When aiming at a precise comparison of the calculated adsorption parameters with experiment, one needs to address additionally the issue of substrate relaxation: (i) without an adsorbate and (*ii*) in the presence of surface C species. However, when doing so, one should keep in mind that Pd clusters of sizes considered in the present study and completely structurally optimized with O_h symmetry constraints are characterized by average nearest-neighbor distances $\bar{r}$(Pd–Pd) = 267–268 pm which are notably shorter than the value 273 pm, obtained by extrapolating to infinite cluster radius [62]. Thus, when accounting for substrate cluster relaxation, one would actually model adsorption interactions with *clusters* of a particular (moderately large) size instead of single-crystal surfaces or extended terraces of those metal particles that are commonly studied by experimentalists [1,16,54,203–205], but are notably larger, comprising 10^3–10^4 atoms. Nevertheless, it is useful to investigate cluster relaxation effects, to understand more comprehensively the accuracy of our cluster model approach.

For instance, on the cluster Pd_{85} with its geometry fixed after relaxation, we calculated the adsorption energy of μ_3-C moieties at 605 kJ mol^{-1} (BP86), i.e., 30 kJ mol^{-1} (5%) lower than on the unrelaxed (bulk-terminated) cluster (Table 4.1). This optimized Pd_{85} cluster features an average metal-metal distance $\bar{r}$(Pd–Pd) = 267.2 pm; the Pd–Pd distance determining the adsorption sites Pd_3 is r_{Pd3}(Pd–Pd) = 270.4 pm [62]. The cluster-size effect is somewhat reduced for the larger relaxed cluster Pd_{140}: D_e(BP86) = 611 kJ mol^{-1} or 25 kJ mol^{-1} (4%) smaller than for the corresponding unrelaxed cluster geometry. The relaxed structure of Pd_{140} is characterized by $\bar{r}$(Pd–Pd) = 268.3 pm and r_{Pd3}(Pd–Pd) = 273.9 pm [62]. Qualitatively, adsorption energies on relaxed clusters are lower because the Pd

atoms affecting the bonding with C adsorbates exhibit more valence saturation due to shorter Pd–Pd contacts. The concomitant relaxation-induced elongation of Pd–C bond lengths in both systems is minor, only ~1 pm.

The effects of relaxing all degrees of freedom of C_m/Pd_n moieties (subject to O_h constraints), both intrasubstrate as well as adsorbate-substrate, can be evaluated for the systems μ_3-C_8–Pd_{79} and μ_3-C_8–Pd_{116}. Pertinent calculated characteristics are $\bar{r}$(Pd–Pd) = 269.8 pm, r(Pd–C) = 187.1 pm, r_{Pd3}(Pd–Pd) = 274.8 pm, and D_e(BP86) = 658 kJ mol^{-1} for Pd_{79} and $\bar{r}$(Pd–Pd) = 270.0 pm, r(Pd–C) = 185.8 pm, r_{Pd3}(Pd–Pd) = 277.3 pm, and D_e(BP86) = 670 kJ mol^{-1} for Pd_{116}. In these cases, the adsorption energy (the most sensitive observable under investigation) is larger than the results obtained at bulk-terminated cluster geometries, but only by 15–20 kJ mol^{-1} (3%).

To conclude, the relaxation contributions to the *absolute* values of the adsorption energies of μ_3-C species on Pd clusters are found to be rather small. For practical applications, the *relative* adsorption energies, computed on various sites, are more important. Relaxation is not expected to notably affect the relative stability of the adsorption complexes at the various sites. The site aspect of C adsorption will be examined in the following.

B. C adsorbates on various sites of the cluster Pd_{140}

Results for adsorption complexes of atoms C on various sites of bulk-terminated and relaxed cluster models Pd_{140}, computed at O_h symmetry, are collected in Table 4.2. The systems under scrutiny include those featuring the lowest possible (symmetry-allowed) coverage of C adsorbates (a) at fourfold hollow sites of (very small) (100) facets – μ_4-C_6, (b) over threefold hollow sites in the centers of each of the eight (111) facets – μ_3-C_8, (c) at the bridge sites in the middle of all 12 cluster edges – μ_2-C_{12}. Furthermore, we also considered higher-coverage adsorption systems with 24 C atoms each, where the following three out-of-center sites on each (111) facet are occupied: (d) outermost threefold hollows – μ_3-C_{24}, (e) bridges – μ_2-C_{24}, and (f) on-top-C_{24} sites (see Figure 4.2).

Let us first consider data calculated for relatively low-coverage adsorption complexes on Pd_{140} – with 6, 8, and 12 carbon atoms. The models with bulk-

Table 4.2. Observables calculated for the adsorption complexes of C atoms on various sites of unrelaxed and relaxed octahedral clusters Pd_{140} (see Figure 4.2). r(Pd–C) – distance between C and the nearest-neighbor Pd atoms optimized at the VWN level, z(C) – height of the C atom over the plane defined by the nearest-neighbor Pd atoms, D_e – adsorption energy per C atom, evaluated with the BP86 exchange-correlation functional and corrected for the BSSE (~20±10 kJ mol^{-1}), q(C) and q(Pd) – potential-derived charges of adsorbed C and the nearest-neighbor Pd atoms, respectively. The nearest-neighbor Pd–Pd distances were fixed at the experimental value for Pd bulk, 275 pm. The values for the adsorption of C on the structurally relaxed cluster Pd_{140} (and fixed at that geometry) are given in italics; the Pd–Pd distances between the atoms that define the adsorption sites of the relaxed Pd_{140} cluster are 262.7 pm (μ_4), 273.2 pm (μ_3), 271.3 pm (μ_2). For easy reference, the reference letters to the subpanels of Figure 4.2 are given in the table header.

	μ_4-C_6 Pd(100)	μ_3-C_8 Pd(111)	μ_2-C_{12} Pd edge	μ_3-C_{24} Pd(111)	μ_2-C_{24} Pd(111)	On-top-C_{24} Pd(111)
	a	*b*	*c*	*d*	*e*	*f*
r(Pd–C) (pm)	194.6 *195.2*	185.5 *186.4*	179.2 *179.9*	186.6	185.3	169.7
z(C) (pm)	6.3 *59.7*	96.0 *98.7*	114.9 *118.4*	98.1	124.2	169.7
D_e(BP86) (kJ mol^{-1})	714 *640*	636 *612*	590 *569*	516	419	398
q(Pd)[a] (a.u.)	0.10 *0.34*	0.53 *0.57*	0.46 *0.44*	0.64 (×2) 0.33 (×1)	0.62	0.33
q(C) (a.u.)	–1.08 *–1.14*	–1.60 *–1.52*	–1.00 *–0.94*	–0.97	–0.67	–0.54

[a] Charges of Pd atoms that define the adsorption sites on the bare Pd_{140} cluster at bulk-terminated geometry (values for the *optimized* structure in parentheses): μ_4-C_6 Pd(100), –0.13 (–0.10); μ_3-C_8 Pd (111), 0.00 (0.03); μ_2-C_{12} Pd edge, –0.10 (–0.13); μ_3-C_{24} Pd(111), –0.13(×2), 0.09 (×1) (–0.10(×2), 0.05(×1)); μ_2-C_{24} Pd(111), –0.13 (–0.10); on-top-C_{24} Pd(111), 0.09 (0.05).

terminated geometry of the cluster (Table 4.2) reflect a clear propensity of the adsorbed atomic C moieties to favor highly coordinated sites on a Pd substrate: the largest binding energy at fourfold hollow sites, followed by threefold hollow sites and bridge sites on the edges. Relaxation of the substrate cluster reduces the strength of the adsorbate-substrate interaction for all three types of sites, in line with

the results discussed in Subsection 4.1.3 A. For the moieties μ_3-C_8 and μ_2-C_{12}, the relaxation effect is very modest and quite comparable in size, 21–24 kJ mol^{-1}. Also, the pertinent Pd–C distances in these complexes are calculated to be altered by 1 pm only, compared to the corresponding complexes on the unrelaxed substrate. This is consistent with the rather small reduction of Pd–Pd distances between the cluster atoms that define the adsorption sites (and are the nearest-neighbors of the adsorbate): by 2 pm and 4 pm for μ_3- and μ_2-sites, respectively. However, the corresponding Pd–Pd distances of the μ_4 site shrink much more, 12 pm, indicative of the more pronounced relaxation-induced change of the adsorption strength on this site. Indeed, adsorbed C species over μ_4 sites of the bulk-terminated cluster, characterized by r(Pd–Pd) = 275 pm, have enough space to be accommodated in the void of the μ_4 site, only 6 pm above the plane of the Pd_4 moiety defining the site. On the relaxed cluster, C is pushed out of the void and positioned 60 pm (!) above the Pd_4 plane. This rearrangement is accompanied by a notable reduction of the adsorption energy, by ~70 kJ mol^{-1} (or 10%). Such a pronounced effect can be traced back to the very small size of the fragment (only 4 Pd atoms) that describes the (100) terrace of the Pd_{140} model. However, even for the relaxed Pd substrate, the site μ_4 is still the most favorable one and its energy preference relative to the next stable site μ_3 remains significant, ~30 kJ mol^{-1}.

Recall that experimental metal clusters (containing more than 10^3 atoms [16]), due to their size, are characterized by average nearest-neighbor Pd–Pd distances which are notably closer to the experimental bulk-terminated value than the present optimized clusters. Therefore, when aiming at studying adsorption properties of experimentally relevant model clusters, a geometry optimization of the present (still relatively small) clusters does not necessarily imply enhanced reliability of these relaxed theoretical models and, concomitantly, a higher accuracy of the corresponding calculated results. Thus, we deliberately refrained from considering optimized models in the following.

When the coverage of the Pd_{140} cluster is increased to C_{24} to accommodate three species at each of the (111) facets (keeping the high O_h symmetry), one gets an opportunity to compare regular bridge μ_2 and on-top sites with threefold hollow

sites. The latter sites can also be compared to μ_3 sites in the center of the (111) facets, studied at lower coverage, μ_3-C_8. Adsorption complexes of C at these two kinds of the μ_3 sites of bulk-terminated substrate clusters feature very similar distances, differing at most by 2 pm (Table 4.2). On the other hand, adsorbed C species of μ_3-C_{24}–Pd_{140} are calculated ~120 kJ mol^{-1} (almost 20%) weaker bound than those in the lower-coverage model μ_3-C_8–Pd_{140}.

The charge of μ_3-C moieties on palladium is likely the key for rationalizing this notable bond weakening (Table 4.2). In fact, large (in absolute value) negative potential-derived charges of the adsorbates, -1.6*e* (μ_3-C_8–Pd_{140}) and -1.0*e* (μ_3-C_{24}–Pd_{140}), are indicative of the "carbidic" nature of atomic C on Pd. For the cluster as a whole, one arrives at an overall electron density transfer of 23.7*e* from the Pd_{140} moiety to the set of eight C "ligands". Also, this dramatic redistribution of electron density can be cited to rationalize why the negative charge *per C atom* is notably smaller in the case of 24 C ligands than in μ_3-C_8–Pd_{140} with fewer ligands. Because of lateral repulsion between the three C species situated on the same (111) facet at interatomic contacts of 825 pm, along with the (significantly screened) repulsion between C species located around one (100) facet at C–C contacts of 372 and 527 pm, one expects a notably reduced C adsorption energy in μ_3-C_{24}–Pd_{140} compared to μ_3-C_8–Pd_{140}. The repulsion between C_8 species of the latter system, located at adjacent facets at 759 pm, is apparently much weaker due to the "screening" by the metal particle. On-top and bridge-bound C moieties on regular (111) sites are clearly negatively charged as well, although the charges at these positions with lower coordination numbers are smaller (by absolute value). As manifested by the charges calculated for Pd atoms, a significant part of the electron density accumulated on adsorbed C atoms is withdrawn from the metal centers in the immediate vicinity; thus, most of the influences of the electron density transfer on the cluster reactivity are expected to be sufficiently local [224,225].

Returning to the systems with 24 adsorbed C moieties on the Pd(111) facets, one can question whether a displacement of an adsorbate to the border of a facet can lead to any stabilization. In fact, in the series on-top-C_{24}–Pd_{140} → μ_3-C_{24}–Pd_{140} → μ_2-C_{24}–Pd_{140}, the C adsorbates gradually move closer to the cluster edges

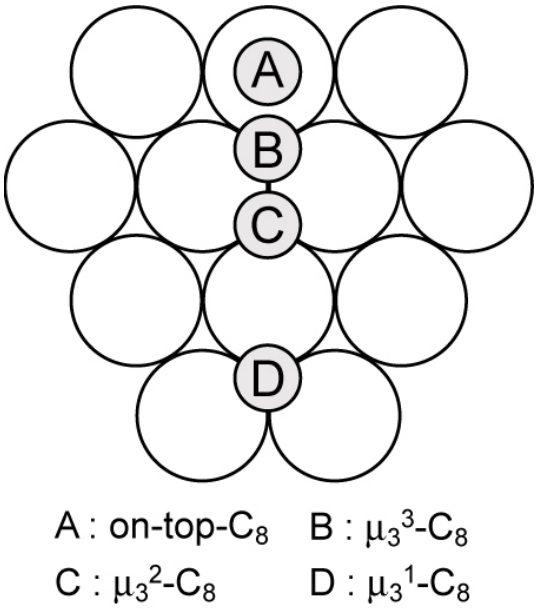

Figure 4.3. Adsorption sites of C atoms on (111) facets of the clusters Pd_{116} studied in D_{4h} symmetry (see Table 4.3).

so that the direct "through space" C–C repulsion on one (111) facet becomes weaker. (Of course, there also is repulsion between adsorbates of adjacent facets, but that is substantially screened by the substrate.) However, the alteration of the electrostatic effect appears to be less pronounced along that series than the inherent site preference of C on Pd that favors μ_3 sites over μ_2 and on-top sites. Thus, in these models, adsorbate relocation closer to the edges of the (111) facets does not seem to entail an energy gain – a mechanism which has been invoked to rationalize experimental observations [54].

The question to be answered next is how the adsorbate-substrate interaction is modified when the adsorbate-adsorbate repulsion is strongly diminished by allowing C species to appear in less-symmetric configurations on Pd nanoclusters.

C. Migration of C species on (111) facets of the cluster Pd_{116} at reduced symmetry

In the models addressed, adsorbed C atoms on each of the (111) facets were forced to stay rather close to each other (in three general positions) due to the symmetry constraints. To decrease the electrostatic repulsion between these carbidic

Table 4.3. Calculated observables for C atoms adsorbed on various sites of the cluster Pd_{116} with fixed bulk-terminated structure, treated in D_{4h} (see Figure 4.3) or O_h symmetry. r(Pd–C) – inter-atomic distances to the nearest-neighbor Pd atoms optimized at the VWN level, z(C) – height of the C atom over the (111) facet, D_e – adsorption energy per C atom, evaluated with the BP86 exchange-correlation functional and corrected for the basis set superposition error.

Observable	On-top-C_{24} O_h	On-top-C_8 D_{4h}	μ_3^1-C_8 D_{4h}	μ_3^2-C_8 D_{4h}	μ_3^3-C_8 D_{4h}
r(Pd–C) (pm)	169.7	169.0	190.0	185.0	184.3
z(C) (pm)	169.7	169.0	104.4	95.0	93.6
D_e(BP86) (kJ mol^{-1})	413	419	424	657	637

adsorbates, which must be less severe on more extended Pd clusters commonly treated experimentally [1,16,54,203–205], one has to reduce the imposed symmetry. To do so, we considered the cluster model Pd_{116} (Figure 4.1) in lower symmetry D_{4h}; like Pd_{140}, it features both (111) and (100) facets. In these D_{4h} models, each (111) facet is always occupied by only one C adsorbate. Thus, one is able to study the migration of a single C adsorbate in that plane perpendicular to a (111) facet, which comprises the median of the corresponding triangle (see Figure 4.3).

Three different μ_3 positions can be examined with the help of the D_{4h} model μ_3-C_8–Pd_{116} (Figure 4.3): (i) *hcp* μ_3^2 over the center of a facet; (ii) μ_3^3 over the nearby *fcc* site; and (iii) μ_3^1 over the next-nearest *fcc* site, adjacent to the (100) facet and resembling the sites of model μ_3-C_{24}–Pd_{140} (see preceding subsection). Furthermore, we also inspected an on-top adsorption complex with this D_{4h} model (Figure 4.3) for comparison with the higher-coverage O_h model, on-top-C_{24}–Pd_{116}.

The calculated structural parameters of the μ_3-C_8–Pd_{116} systems (Table 4.3) are rather close to those computed for the complexes μ_3-C_8–Pd_{140} and μ_3-C_{24}–Pd_{140} (Table 4.3). The only notable elongation of a Pd–C bond (~5 pm) is found in the complex μ_3^1-C_8–Pd_{116}, where also the calculated adsorption energy, 424 kJ mol^{-1}, deviates by as much as 210–230 kJ mol^{-1} from the energy values of the analogs μ_3^3-C_8–Pd_{116} and μ_3^2-C_8–Pd_{116}, 637 and 657 kJ mol^{-1}, respectively (Table 4.3); these values should be compared to the binding energy of 636 kJ mol^{-1} calculated for μ_3-

C_8–Pd_{140}. The large (relative) destabilization of the system μ_3^1-C_8–Pd_{116} probably reflects mainly the partial loss of Pd atoms in the second coordination sphere of the adsorbed C.

The adsorption energy of C on threefold hollow sites of μ_3^1-C_8–Pd_{116} is essentially equal to the value 419 kJ mol^{-1} calculated for C in on-top-C_8–Pd_{116} and just slightly larger than that of on-top-C_{24}–Pd_{116}, 413 kJ mol^{-1}. Thus, inherent structural features of perfectly ordered metal nanoparticles (i.e., edges formed at the intersection of facets) may strongly affect the adsorption propensity of nearby surface sites to the extent that the latter lose their intrinsic properties as sites on a regular metal surface. Indeed, in the above case, threefold hollow sites (which dominate C adsorption on the ideal single-crystal Pd(111) surface and on the interior of (111) facets of Pd nanoclusters) may become, when located near edges, much less attractive for C – comparable to the weakest sites of regular (111) facets, namely on-top. This is a very important result for quantifying and clarifying reactivity features of metal nanoparticles. Another pertinent example is CO adsorption on bridge-edge sites of Pd nanoparticles that became most favorable among a variety of adsorption positions of CO on Pd surfaces [61].

One can see from Table 4.2 and Table 4.3 that the complex μ_3^2-C_8–Pd_{116} with C located over the centers of the (111) facets, features the largest adsorption energy among the μ_3-C-complexes we have addressed in this section. Thus, even this more realistic cluster model C_8–Pd_{116} (D_{4h}), which allows one to essentially avoid lateral repulsion between adsorbates, does not provide evidence that migration of adsorbed carbidic C species to the edges of (111) facets of Pd nanoparticles is energetically favored. It seems justified to assume that the electrostatic C–C repulsion in the models μ_3^2-C_8–Pd_{116} and μ_3^3-C_8–Pd_{116} (Figure 4.3) is indeed minor. Therefore, the preference of atomic C adsorbates for decorating surface sites near edges of supported model Pd catalysts, which was inferred in experimental studies [54], should be rationalized in a different fashion. Then, on the basis of the present studies, one may propose that C atoms occupy μ_4 sites on Pd(100) facets adjacent to cluster edges or point defects where Pd atoms are missing, thus also allowing a high coordination of C adsorbates. The former mechanism seems less probable because

the number of Pd(100) μ_4 sites was claimed to be rather small on clusters [54]. The latter mechanism is particularly plausible in view of the preference of C adsorbates for higher-coordinated surface positions on Pd, identified in this work based on calculated adsorption energies. This mechanism deserves to be studied further with cluster model calculations.

4.1.4 CO adsorption on Pd_{140} cluster pre-covered by C deposits

After considering the bonding of atomic carbon deposits on Pd nanoclusters in the previous subsection, the next issue is the effect of such surface pre-covering by C on the reactivity of the metal particles. It will be addressed in the following by probing the surface properties of the Pd_{140} cluster modified by C with respect to CO adsorption.

A strong influence of subsurface carbon atoms, C_{sub}, in Pd nanoclusters has been found on adsorption parameters of probe CO molecules occupying positions immediately above C_{sub} [206]. For instance, it was shown that the adsorption energy of these CO molecules is reduced by a factor of two compared to that on the clean nanoclusters and, concomitantly, the C–O frequency is shifted by ~80 cm^{-1}. These findings were rationalized as a consequence of the locally withdrawn electron density by the C_{sub} impurities, which reduced the propensity of Pd substrate to strengthen the π back donation channel of the bonding with adsorbed CO [206]. Relative weakening of the CO adsorption on Pd catalysts when samples were contaminated by carbon has also been documented experimentally [226].

In contrast, STM experiments on single crystal Pd(111) terraces provide evidence that subsurface impurities (tentatively ascribed to atomic carbon) *strengthen* the interaction with CO molecules adsorbed nearby [227]. It was shown there, that at 60 K CO molecules cluster around these subsurface impurities on Pd(111), whereas in impurity-free areas CO molecules diffuse quickly under the same conditions. With regard to the above mentioned calculated and experimental data we will focus in this subsection on two particular questions: (i) whether any stabilizing effect on co-adsorbed CO molecules can also be identified for *surface* C

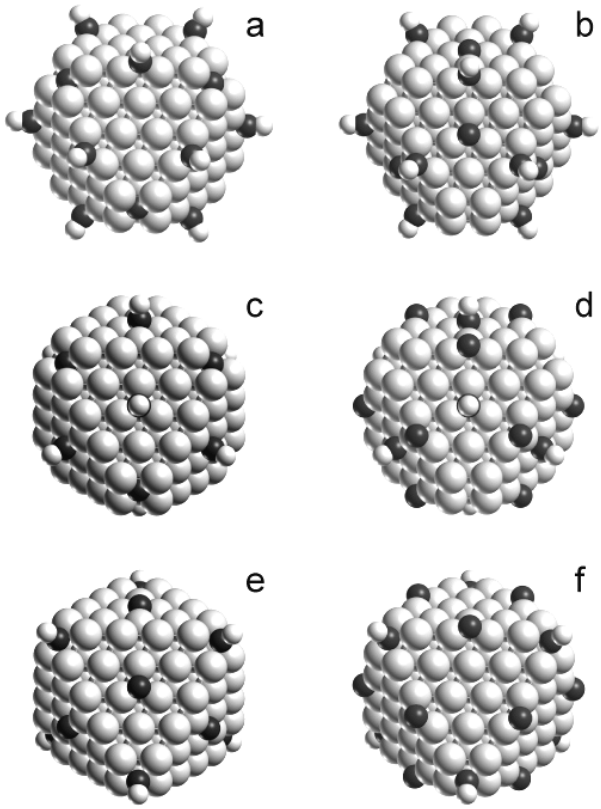

Figure 4.4. Sketches of co-adsorption complexes of C atoms and CO molecules on cuboctahedral model clusters: a – $(\mu_4\text{-C})_6Pd_{140}(\mu_2\text{-CO})_{12}$, b – $(\mu_3\text{-C})_8Pd_{140}(\mu_2\text{-CO})_{12}$, c – $(\mu_4\text{-C})_6Pd_{140}(\mu_3\text{-CO})_8$, d – $(\mu_2\text{-C})_{12}Pd_{140}(\mu_3\text{-CO})_8$, e – $(\mu_3\text{-C})_8Pd_{140}(\mu_4\text{-CO})_6$, f – $(\mu_2\text{-C})_{12}Pd_{140}(\mu_4\text{-CO})_6$.

species on Pd and (ii) how local the influence of C deposits on the surface reactivity is.

The cluster models of co-adsorbed C and CO species on Pd nanoclusters considered here (Figure 4.4) are based on the models previously dealt with in this section [55] – C_nPd_{140} systems with the lowest number n of carbon atoms. We have chosen the substrate samples with carbon atoms in the following positions: four-fold, $(\mu_4\text{-C})_6Pd_{140}$ (Figure 4.4, panels a and c), three-fold, $(\mu_3\text{-C})_8Pd_{140}$ (Figure 4.4, panels b and e) or two-fold ("bridge-on-edge"), $(\mu_2\text{-C})_{12}Pd_{140}$ (Figure 4.4, panels d and f). On each of these moieties CO molecules are adsorbed in those of the lowest-coverage symmetry-allowed μ_4, μ_3 or μ_2 (edge) sites, which were not blocked by C atoms. The calculated results are collected in Table 4.4.

Table 4.4. Calculated parameters[a] of CO probe molecules adsorbed on clean [61,62] or pre-covered by atomic carbon Pd_{140} clusters (O_h), optimized at the BP86 level with Pd–Pd distances fixed at the experimental value 275 pm for Pd bulk and positions of atomic C as described in previous subsection.

System	r(C-O), pm	r(Pd-C), pm	D_e(BP86), kJ mol^{-1}	ω_e(C-O), cm^{-1}
edge (μ_2-CO)$_{12}$				
Pd_{146}	117.5	198.2	188	1859
$(\mu_4\text{-C})_6Pd_{140}$	117.5	197.9	192	1854
$(\mu_3\text{-C})_8Pd_{140}$	117.4	198.4	186	1853
hcp (μ_3-CO)$_8$				
Pd_{140}	118.9	206.3	169	1748
$(\mu_4\text{-C})_6Pd_{140}$	118.8	206.7	186	1751
$(\mu_2\text{-C})_{12}Pd_{140}$	118.6	207.0	175	1766
(μ_4-CO)$_6$				
Pd_{140}	119.8	222.9	149	1656
$(\mu_3\text{-C})_8Pd_{140}$	119.8	223.2	169	1777
$(\mu_2\text{-C})_{12}Pd_{140}$	119.6	222.7	147	1677

[a] r(C–O) and r(Pd–C) – interatomic distances of the C atoms of carbonyl groups to the nearest neighbor O and Pd atoms, respectively, D_e – BP86 adsorption energy per CO group corrected for BSSE (~10-15 kJ mol^{-1}), ω_e – harmonic stretching frequency of adsorbed CO.

The adsorption complexes with μ_2-CO molecules on the edges of Pd nanoparticles were found to be the most stable ones in the absence of carbon impurities [61]. The presence of the latter species, either in the preferred μ_4-C form (Figure 4.4, a) or as the second-most stable μ_3-C form (Figure 4.4, b), hardly affects any of the calculated parameters of the adsorbed CO (Table 4.4). Indeed, pertinent interatomic distances change less than 1 pm and the C–O frequencies are altered by ~5 cm^{-1} only, a value which is below the inherent accuracy of the present computational approach and, thus, insignificant. The same conclusion is also valid for the negligible alteration of the CO adsorption energy. This minor effect of μ_4-C deposits on the CO co-adsorbates can probably be assigned, apart from the rather

large distance between C and CO moieties, to the fact that μ_4-C particles are well screened by the Pd_4 moiety forming the adsorption site, being a very small fragment of a (001) terrace. Despite of the notable potential-derived charge of μ_4-C on Pd_{140}, -1.08 e (Table 4.2), the corresponding charge rearrangement appears to be well localized and essentially does not affect μ_2-edge adsorption sites of CO probes. An additional argument is that bridge-edge sites also feature well-localized adsorption properties. This characteristic may also provide a tentative rationalization of barely changed calculated parameters of CO in $(\mu_3\text{-C})_8Pd_{140}(\mu_2\text{-CO})_{12}$ vs. $Pd_{140}(\mu_2\text{-CO})_{12}$.

On the regular Pd(111) terraces of both single crystals and nanoparticles, at low coverages CO molecules preferably occupy μ_3-sites. In the presence of μ_4-C or μ_2-C deposits, such μ_3-CO adsorbates on the Pd_{140} cluster are computed to be affected slightly more than the just discussed edge μ_2-CO ones (Table 4.2). Whereas the structure does not change appreciably, the C-O vibrational frequency calculated for $(\mu_2\text{-C})_{12}Pd_{140}(\mu_3\text{-CO})_8$ increases by almost 20 cm^{-1} compared to the reference $Pd_{140}(\mu_3\text{-CO})_8$. This frequency increase of the μ_3-CO species over the center of the (111) terrace might be due to a "through space" (or "solvent") effect of the nearby strongly negatively charged three edge-μ_2-C moieties [228]. More importantly, the adsorption energy of μ_3-CO species *increases* due to both edge-μ_2-C and – to a larger extent – μ_4-C deposits; in the latter case, the increment is 17 kJ mol^{-1} or 10% of the overall binding energy (Table 4.4). Therefore, one is lead to conclude that not only mechanisms for the atomic carbon deposits exist which decrease the reactivity of specific surface sites on Pd nanoparticles (as manifested by calculated CO adsorption energies on μ_3-sites above C_{sub} [206], but which also are able to increase the reactivity to some extent. Two effects are possible: the adsorption energy decreases when CO is above C_{sub} and it increases when C_{ads} is nearby – as we found here. At the moment it is difficult to clarify such a latter mechanism in detail. However, it is well known (see also Section 4.2) that the C–O vibrational frequency mainly reflects the local electronic structure of an adsorption site on a metal surface [56,62,206,219]. In fact, the frequency value for the $(\mu_4\text{-C})_6Pd_{140}(\mu_3\text{-CO})_8$ is barely changed compared to $Pd_{140}(\mu_3\text{-CO})_8$ (Table 4.4). On the other hand, adsorption

energies in many cases seem to change mainly for reasons of global (long-distance) nature; see also the discussion in Section 4.2.3.B.

Also parameters of μ_4-CO adsorbates on Pd nanoparticles, which appear to be less stable than either the edge-μ_2-CO or the μ_3-CO complexes just discussed, can be notably affected by the presence of μ_3-C deposits; there, both the CO adsorption energy and its stretching vibrational frequency are increased, by 20 kJ mol^{-1} and ~120 cm^{-1}, respectively. Curiously, the adsorption energy of μ_4-CO on $(\mu_2\text{-C})_{12}Pd_{140}$ basically coincides with that on bare Pd_{140} cluster whereas the vibrational frequency values are different by some 20 cm^{-1}. This appears to be one more indication of the different origin of the two observables under scrutiny: the local nature of vibrational properties and the global character of changes in adsorption energies, reflecting the characteristics of metal surfaces as a whole.

In summary, the results of this subsection reveal that atomic carbon impurities on the surface of Pd particles of nanometer size is able to affect parameters of co-adsorbed CO probe molecules in a limited, but certainly non-negligible fashion, even when C and CO species are sufficiently far apart. Whereas Pd–CO and C–O bond lengths remain almost unaffected by C deposits, the C–O frequency may change significantly. Most interestingly, we were able to diagnose that there exist mechanisms which stabilize CO adsorption on Pd nanoclusters to some extent when atomic C impurities are present. Such mechanisms seem to be able to overcompensate the effect of electron density withdrawal from the Pd cluster to the strongly negatively charged deposited C moieties. The latter effect is well-known to result in reduced π back donation to CO and thus in a weaker adsorption bonding, which was found, for instance, for μ_3-CO adsorbed over subsurface C species on Pd nanoparticles [206].

4.1.5 Summary and outlook

We carried out an all-electron scalar relativistic density functional study of adsorbed atomic carbon species. Such adsorbates can be formed in the course of surface reactions and decorate metal catalysts. For this purpose, we employed the novel approach based on three-dimensional metal particles of diameters exceeding 1 nm,

which were chosen as fragments of bulk Pd. Such nano-crystallites expose (111) and small (100) facets as well as edge sites. We examined which particular surface sites of these clusters are preferred for C adsorption.

The calculated energies of C adsorption on threefold hollow sites of the cluster series Pd_{79}, Pd_{85}, Pd_{116}, Pd_{140}, and Pd_{146} vary by ~20 kJ mol^{-1} or by only 3% of the overall values, about 630 kJ mol^{-1} (for the BP exchange-correlation functional). Thus, we demonstrated relatively fast convergence of calculated adsorption parameters, *including the adsorption energy* of strongly bound C moieties, with growing size of the symmetric three-dimensional nanoclusters. Moreover, we showed that the adsorption energy of C in the cluster model scheme is calculated sufficiently close to the value obtained with a periodic slab model approach, if the same exchange-correlation potential is used in both model strategies.

For a series of conceivable adsorption sites, we theoretically characterized, for the first time, C–Pd_n interactions structurally, energetically, and from the viewpoint of adsorbate-substrate charge rearrangement. C atoms were calculated to be strongly adsorbed in the form of carbidic species that bear a significant negative charge and thus experience a notable mutual electrostatic repulsion at short distances. Surface sites with fourfold coordination (the highest possible) of carbon appear to be overall favored, but a study of more μ_4 sites on Pd is required to substantiate this general conclusion; on the (111) facets, threefold hollow sites in the center are energetically preferred.

Global symmetry reduction of the nanoclusters from O_h to D_{4h} point group allowed us to study selected locally less-symmetric adsorption complexes which also feature considerably reduced intraadsorbate electrostatic repulsion. In such D_{4h} models, displacement of adsorbed C toward the facet borders was computed to be accompanied by a slight destabilization. We did not find any energy gain due to enhanced adsorbate-substrate interactions at regular sites near the boundaries (edges) of (111) facets, as anticipated in experimental studies. Our results call for another rationalization of the experimental findings.

The symmetry reduction just mentioned represents an important extension of the strategy to employ three-dimensional cluster models in studies of adsorption and reactivity. Indeed, on three-dimensional metal nanoclusters with a symmetry lower than O_h, e.g., D_{4h}, one can accommodate adsorption complexes which feature *local* C_{2v} symmetry, rather than atoms or "up-right" linear molecules as done previously. In addition, these models admit low coverage, with only one adsorbate per (111) facet. If a locally completely asymmetric adsorbate or a transition state complex is to be considered, reduction to *global* D_4 symmetry would suffice within the present nanocluster scheme. Calculations employing that latter symmetry are becoming feasible, also for heavy-element nanoparticles.

We also found that the presence of atomic carbon impurities on the surface of Pd nanoparticles of the nanometer size notably affects adsorption properties of CO molecules. Whereas the Pd–CO and C–O bond lengths remain almost unaffected by the rather distant C deposits on Pd_{140}, the C–O frequency may change significantly. We were lead to infer the existence of mechanisms which stabilize CO adsorption on Pd nanoclusters when atomic C impurities are present. Such mechanisms apparently can overcompensate the well-known destabilizing effect of the electron density withdrawal from the Pd cluster to the strongly negatively charged surface C moieties. This finding broadens the opportunities for a fine tuning of the reactivity of metal clusters by C contaminants.

4.2 Model Pd–Zn nanoclusters and their adsorption complexes with CO molecules

4.2.1 Introduction

Steam reforming of methanol over metal catalysts is an attractive process for producing in-situ H_2 as an energy carrier alternative to conventional fuels [229]. Novel efficient catalysts based on a Pd/ZnO system have been proposed for the steam reforming reaction [230,231]. The high performance of these catalysts was attributed to Pd–Zn alloy particles [232,233]. Despite the importance of Pd–Zn moieties, only very limited electronic and structural information on them at the atomic level has been available until very recently [234,235], thus preventing a detailed characterization of the active component of the catalyst and understanding its function.

This lack of structural and electronic information about the surface of bimetallic Pd–Zn species prompted our group to initiate systematic DF slab model calculations of these materials that address diverse aspects important for elucidating their stability, structure and reactivity [223,236,237]. A comparative study of surface energies of binary (1:1) PdZn alloys with CuAu-$L1_0$ structure revealed that (111) and (100) surfaces exposing stoichiometric layers are more stable than (001) and (110) surfaces which consist of alternating Pd and Zn layers; therefore, surfaces with the (111) and (100) orientations probably form preferentially under ambient experimental conditions [236]. Exploration of surface segregation of Zn and Pd in supported PdZn alloy films revealed that it depends significantly on the support; at stoichiometric surfaces of 1:1 alloy, segregation of neither Zn nor Pd was calculated favorable whereas in films rich in Zn or Pd segregation of the dominant component was found possible [237]. More recent computational slab model studies devoted to the structure and energetics of adsorption complexes relevant for methanol decomposition on the single crystal PdZn(111) surface [223].

The electronic structure investigations just outlined focused on idealized situations modeling rather extended (111) terraces of PdZn alloy catalysts with a low concentration of various defects. More realistically (see Section 4.1), active sites of supported metal catalytic materials can be represented by model catalysts [1,16] which consist of well ordered nanoscale metal particles deposited on oxide films. Such model catalysts are less complex than "real" catalysts although they feature, at variance with regular single-crystal metal surfaces, most of the irregularities inherent to real catalysts, such as edge and step sites as well as regular sites in their proximity. Recently, an efficient computational strategy for modeling extended terraces [62] as well as supported metal nanoparticles [61] that relies on symmetric three-dimensional model clusters which are terminated by low-index surfaces and contain 100 or more metal atoms were proposed.

In this section, we consider a series of model octahedral Pd–Zn nanoscale clusters $Pd_{140-n}Zn_n$ (n = 0, 8, 24, 32) and their complexes with CO molecules adsorbed on threefold hollow sites built by three Pd atoms in the center of (111) facets. To the best of our knowledge, this is the first high-level electronic structure study of *bimetallic* clusters containing over 100 heavy-element atoms and approaching the size of 2 nm. Thus, this study [56] extends the application area of the novel computational strategy to investigate surface properties of transition metal single-crystal and polycrystalline materials by employing three-dimensional cluster models. A special goal of the present work is to shed a light on the influence of Zn admixtures to Pd nanoclusters at varying concentrations (i) on the electronic structure, the segregation of the Zn component, and the stability of model Pd–Zn nanoparticles, as well as (ii) on their adsorption properties monitored by the binding energy and C–O vibrational frequency of adsorbed carbonyl molecules.

4.2.2 Computational details and models

We performed all-electron calculations using the LCGTO-FF-DF method [150] as implemented in the parallel code PARAGAUSS [151,152]. We used a scalar relativistic variant of the LCGTO-FF-DF method [155,156,238] which employs a second-order Douglas-Kroll transformation to decouple electronic and positronic

degrees of freedom of the Dirac–Kohn–Sham equation. We solved the Kohn–Sham equation self-consistently in the local density approximation (LDA; VWN parametrization [207]); subsequently, we calculated the total energy in a GGA using the self-consistent LDA electron density and the BP86 exchange-correlation functional [139,153]. This computational strategy is very economic, yet sufficiently accurate for geometric parameters, binding energies, and vibrational frequencies [208]; our benchmark self-consistent BP calculations of CO adsorption energies on Pd nanoclusters corroborated its high accuracy (within 1%) [206]. Where explicitly specified in the following, we also employed a modern GGA functional (PBEN [154]) for comparison with the BP results.

The computational parameters were chosen to be consistent with those of previous studies of our group [61,62,206]. For Pd atoms, we used an orbital basis set [209] extended to (18*s*,13*p*,9*d*) by adding one *s* exponent (0.0135), two *p* exponents (0.0904, 0.2143), and one *d* exponent (0.097); it was contracted in a generalized fashion to [7*s*,6*p*,4*d*] using relativistic VWN atomic eigenvectors. To evaluate the classical Coulomb contribution to the electron-electron interaction, the electron density was represented with the help of an auxiliary basis set [150]; for Pd it was of the size (17*s*,6r^2,5*p*,5*d*). For Zn atoms we employed a (14*s*,9*p*,5*d*) orbital basis set [209], extended by one *s* exponent (0.39748), two *p* exponents (0.11610, 0.30312), and a *d* exponent (0.16366), and contracted to [6*s*,5*p*,3*d*]; the auxiliary charge density basis set was (15s,11r^2,5*p*,5*d*). C and O atoms were described by orbital basis sets of the type (14*s*,9*p*,4*d*) [210] using the original general contraction [6*s*,5*p*,2*d*] and by auxiliary basis sets of the type (14*s*,9r^2,5*p*,5*d*). For every atom, the auxiliary basis was constructed as follows: the exponents of *s* and r^2 fitting functions were generated by scaling (all or selected) *s* and *p* orbital exponents, respectively, using a standard procedure [150]; "polarization exponents" were chosen as geometric series with factor 2.5, starting with 0.1 for *p* and 0.2 for *d* exponents.

Our benchmark calculations did not reveal open-shell configurations for the clusters $Pd_{140-n}Zn_n$. For monometallic palladium clusters, which have a potentially larger propensity to exhibit unpaired spins than PdZn clusters, spin averaging

introduces marginal errors [211]. For instance, already for Pd_{85}, this was found to hold for such a sensitive property as the cohesive energy. Furthermore, recall that spin polarization effects decrease with growing cluster size. Therefore, in the following we will discuss only results obtained in a spin-restricted fashion. We applied the technique of fractional occupation numbers [150] (with a Gaussian level broadening of 0.1 eV) to ensure convergence of the SCF process. When probing adsorption properties, we kept the geometric parameters of all bare model clusters $Pd_{140-n}Zn_n$ fixed (see below); we optimized only the positions of adsorbed CO molecules, oriented according to the symmetry group O_h. For that, we consecutively varied Pd–C and C–O distances until changes were below 0.5 pm, using BP energies. We corrected the CO adsorption energy for the basis set superposition error via the counterpoise technique (~20 kJ mol^{-1}) [159]; one quarter of these corrections were due to the incompleteness of the CO basis set. We approximated the harmonic C–O stretching vibration by the C-O internal mode, keeping the CO center of mass fixed; for this purpose, we fitted a polynomial of degree 4 to five total energy values near the minimum of the potential curve.

Designing realistic models of Pd–Zn catalysts is inherently a complicated problem. In fact, even focusing solely on the active bimetallic particles without a support [233,239], one needs to address simultaneously many aspects of the species to be represented. Among them are (i) the size range, (ii) the overall stoichiometry as well as the mutual positions of the constituting Pd and Zn atoms, (iii) the types of the facets exposed and their roughness, and finally (iv) the adsorption sites to be probed. Also, the computational effort required to treat such complex models has to remain within reasonable limits, assuring the feasibility of the calculations.

Here, we focused on Pd–Zn moieties that are sufficiently large to be approximated by clusters with metal-metal (M–M) distances corresponding to bulk samples [62]. We selected a range of relatively low Zn concentrations, up to ~25 %, in the Pd-Zn moieties. Thus, the overall structural arrangement and all M–M distances, 275 pm, of our bimetallic cluster models were chosen as measured for bulk palladium [62]. This is quite different from the CuAu ($L1_0$-type) structure with space group $P4/mmm$, that is featured by PdZn alloys with a Pd: Zn atomic ratio

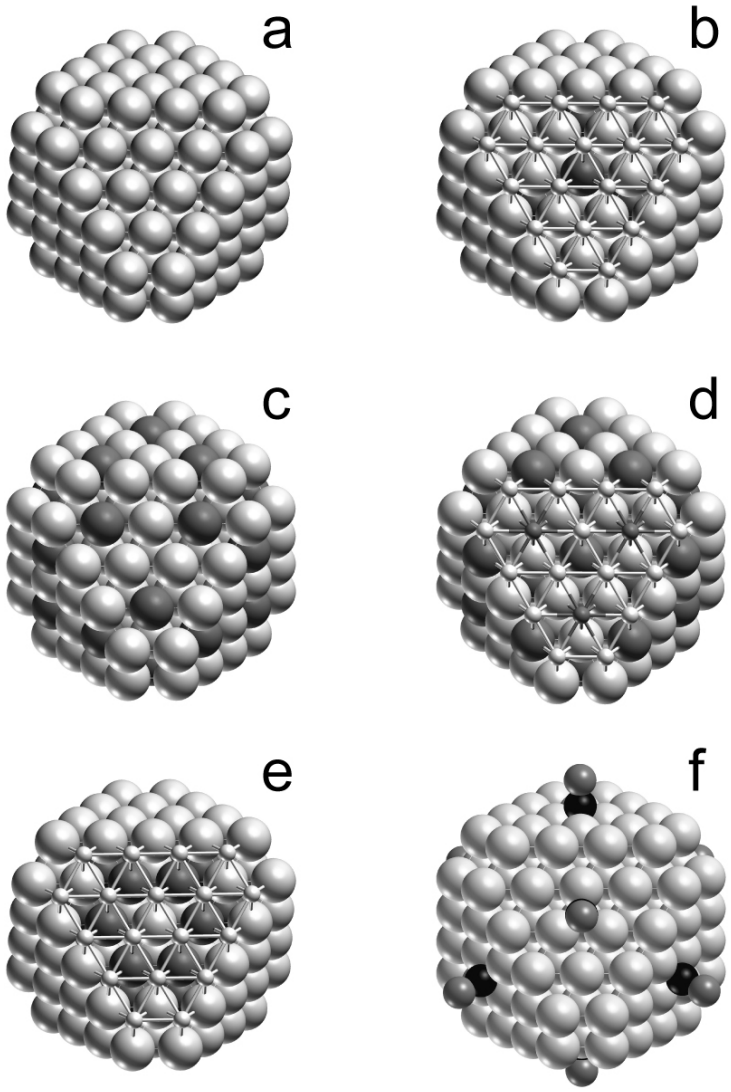

Figure 4.5. Sketches of the cuboctahedral model nanoclusters: (a) Pd_{140}, (b) $Pd_{132}Zn_8$ (0,8), (c) $Pd_{116}Zn_{24}$(24,0), (d) $Pd_{108}Zn_{32}$(24,8), (e) $Pd_{116}Zn_{24}$(0,24), (f) a representative adsorption complex $Pd_{140}(CO)_8$. The numbers of Zn atoms in the surface and subsurface layers, respectively, are given in parentheses. In panels b, d, and e, the first layer of one (111) facet is depicted as a network of bonds only to allow a better description of the subsurface region.

close to 1 [240], that appear to exhibit the highest catalytic performance in steam reforming of methanol [232,233]. For the latter bulk structure, periodic calculations with the PW91 xc potential [162] furnished optimized distances r(Pd–Pd) = 293 pm and r(Pd–Zn)=268 pm [236]. These values deviate notably and in different directions (by 18 pm and –7 pm, respectively) from the M-M bond lengths that we employed in the nanocluster models which we chose to have a significantly lower

Zn content. As mentioned above, M–M distances were kept frozen in the present model study to separate the more pronounced electronic effects and those caused by a variation of the mutual positions of Pd and Zn atoms from the modest effect of changes of M-M bond lengths [61,62,206]. (Note that the average nearest-neighbor Pd–Pd distance in the cluster model Pd_{140} optimized at the LDA-VWN level is 268.3 pm [62].) The mutual positions of Pd and Zn atoms comply with O_h symmetry which we imposed on all cluster models studied in this section.

According to the slab model calculations [236], hexagonal (111) surfaces of PdZn alloys are characterized by the lowest surface energy. Therefore, our cluster models were designed to expose preferentially (111) facets: the cuboctahedral cluster models M_{140} (Figure 4.5a) were obtained by truncating the corresponding octahedral clusters M_{146} to yield eight hexagonal (111) facets. Adsorption sites on these flat facets are rather close to edges. From experimental investigations [241,242] as well as from periodic slab model calculations [243,244], it is known that threefold hollow sites on the Pd(111) surface are energetically favored for CO adsorption at low coverage; therefore, keeping in mind the low concentration of Zn in the bimetallic moieties under investigation, we probed this site by adsorbed CO molecules. For that purpose, we kept intact the central upper-layer Pd_3 moiety on each of the eight (111) facets in all our models, but we partially substituted Zn atoms for nearby Pd atoms. The resulting series of substrate clusters comprises, beyond the reference Pd_{140} (Figure 4.5a), the following four bimetallic systems: $Pd_{132}Zn_8$(0,8), $Pd_{116}Zn_{24}$(24,0), $Pd_{108}Zn_{32}$(24,8), $Pd_{116}Zn_{24}$(0,24); here, the numbers in parentheses refer to Zn atoms in the surface and sub-surface layers, respectively (Figure 4.5b–e). In $Pd_{132}Zn_8$(0,8), eight Zn atoms are located in the second layer of the cluster, just beneath the central Pd_3 triangle of each (111) facet whereas 24 Zn atoms of $Pd_{116}Zn_{24}$(24,0) are in nearest-neighboring first-layer positions of the Pd_3 moiety. The model $Pd_{108}Zn_{32}$(24,8) combines Zn positions of the former two systems. Finally, the 24 Zn atoms of the cluster $Pd_{116}Zn_{24}$(0,24) are arranged as a cage of eight Zn_6 rings with short Zn–Zn contacts of 275 pm. These Zn atoms substitute six subsurface Pd atoms of every (111) facet that surround the position occupied by Zn in $Pd_{132}Zn_8$(0,8) particle; each of the six positions is shared by two

Table 4.5. Calculated energies [a] (in kJ mol^{-1}) for model nanoclusters $Pd_{140-n}Zn_n$ (n = 0, 8, 24, 32)

	Pd_{140}	$Pd_{132}Zn_8(0,8)$	$Pd_{116}Zn_{24}(24,0)$	$Pd_{108}Zn_{32}(24,8)$	$Pd_{116}Zn_{24}(0,24)$
E_b / 140	296	290	279	273	275
$\Delta E_b / n_{Zn}$	–	-100	-100	-101	-120
ε_F	-5.13	-5.20	-4.94	-5.00	-5.17
$\Delta\varepsilon_{Pd4d}$	-2.05	-1.99	-1.99	-1.92	-1.89
$\Delta\varepsilon_{Pd4d}(Pd_3)$	-2.07	-2.04	-1.99	-2.01	-2.04

[a] $E_b / 140 = [n \times E(Zn) + (140-n) \times E(Pd) - E(Pd_{140-n}Zn_n)] / 140$ – average binding (cohesive) energy of $Pd_{140-n}Zn_n$ per atom, where $E(X)$ is the total energy of the species X; $\Delta E_b / n_{Zn} = E(Zn) - E(Pd) + [E(Pd_{140}) - E(Pd_{140-n}Zn_n)] / n_{Zn}$ – average contribution of each of the n_{Zn} Zn atoms to the change of the overall cohesive energy $E_b(Pd_{140-n}Zn_n)$ with respect to $E_b(Pd_{140})$; $\Delta\varepsilon_{Pd4d}$ and $\Delta\varepsilon_{Pd4d}(Pd_3)$ – centers of the Pd 4*d* density of states with respect to the cluster Fermi energy ε_F, total and local (for the Pd_3 moiety in the center of (111) facets), respectively.

second-layers of the adjacent (111) facets. We monitored alterations of electronic properties and the reactivity of these bimetallic clusters as reflected by bonding and vibrations of single CO adsorbates positioned on the central *hcp* sites of their (111) facets (Figure 4.5f).

4.2.3 Results and discussion

We will first discuss calculated observables for bare bimetallic clusters $Pd_{140-n}Zn_n$ and the reference system Pd_{140} and present a comparative analysis of these data. Then, we will address the CO adsorption properties of these clusters.

A. Properties of bare Pd–Zn clusters

The mixed-metal substrate clusters $Pd_{140-n}Zn_n$ (Figure 4.5b–e) contain different numbers of Zn atoms that substitute Pd atoms of the reference cluster Pd_{140} (Figure 4.5a) in the surface layer or just beneath the surface layer or both. This "alloying" results in varying numbers of homo- and heteroatomic nearest-neighbor M–M contacts ("bonds"). The species $Pd_{132}Zn_8(0,8)$, $Pd_{116}Zn_{24}(24,0)$ and $Pd_{108}Zn_{32}(24,8)$

feature 96, 216, and 312 Pd–Zn bonds, respectively, which are formed at the expense of Pd–Pd bonds of the Pd_{140} reference. None of these clusters exhibit direct Zn–Zn contacts; however, such contacts are present in the cluster $Pd_{116}Zn_{24}(0,24)$ which features 288 new types of nearest-neighbor M–M contacts compared to Pd_{140}, 216 of type Pd–Zn and 72 of type Zn–Zn. The Zn–Zn bonds comprise a new feature which is expected to be manifested in qualitatively different properties of the particle $Pd_{116}Zn_{24}(0,24)$ compared to its $Pd_{140-n}Zn_n$ analogs.

The species $Pd_{116}Zn_{24}(0,24)$ and $Pd_{116}Zn_{24}(24,0)$ with the same number of Zn atoms but located in the subsurface layer and on the surface, respectively, can be considered as models for addressing the phenomenon of segregation, namely enrichment of one of the alloy components in the surface by exchange with subsurface atoms. Recently, we studied segregation at the surface of Pd–Zn alloys in detail by means of slab model calculation and we found this process to be very sensitive to the local and overall structure as well as to the stoichiometry of the material [237]. According to the present cluster model results, the total energy of the system $Pd_{116}Zn_{24}(24,0)$ with all Zn atoms on the surface is 19 kJ mol^{-1} per Zn atom lower than that of the system $Pd_{116}Zn_{24}(0,24)$ with all Zn atoms located in sub-surface positions. Surface positions of Zn atoms are favored as consequence of the fact that 72 new Pd–Pd bonds are formed from 72 weaker Zn–Zn bonds while the number of Pd–Zn bonds remains the same in both clusters. This finding agrees with the slab model result that in films rich in Zn [such as the subsurface layer of $Pd_{116}Zn_{24}(0,24)$] segregation of Zn can be favored [237]. The notable cohesive energy gain of 19 kJ mol^{-1} per surface Zn atom can be translated into a cluster stabilization of 7 kJ mol^{-1} per Zn–Zn bond exchanged for a Pd–Pd bond. From these values, the average cohesive energy per atom, E_b / 140 = 296 kJ mol^{-1}, of the cluster Pd_{140} (Table 4.5), and the average coordination number N_{av} = 9.09 of Pd atoms of that cluster [62], one can approximately associate each Zn–Zn and Pd–Pd contact with energy gains of 26 and 33 kJ mol^{-1}, respectively. Note that the latter estimates differ notably from the bond energies of the dimer molecules Pd_2 and Zn_2, namely 96–135 kJ mol^{-1} [40,245] and 3 kJ mol^{-1} [245], respectively. These strong

differences were not unexpected; they reflect the rather different nature of M–M interactions in bulk metals and molecular species.

For the four model clusters which do not exhibit nearest-neighbor Zn–Zn moieties, the calculated average binding (cohesive) energy per atom, $E_b / 140$, decreases when the number of Zn atoms increases (Table 4.5): Pd_{140} – 296 kJ mol^{-1}, $Pd_{132}Zn_8(0,8)$ – 290 kJ mol^{-1}, $Pd_{116}Zn_{24}(24,0)$ – 279 kJ mol^{-1}, $Pd_{108}Zn_{32}(24,8)$ – 273 kJ mol^{-1}. If one translates this reduced overall stability of the model bimetallic clusters upon substitution of Zn for Pd atoms into an alteration of the cluster cohesive energy per Zn atom, one finds a rather large and, interestingly, essentially constant value of about 101 kJ mol^{-1}, for the three bimetallic systems just mentioned which do not show nearest-neighbor Zn–Zn contacts. As discussed above, the cluster $Pd_{116}Zn_{24}(0,24)$ with its weaker Zn–Zn "bonds" features a more pronounced destabilization per Zn atom, 120 kJ mol^{-1}. Based on these results, one concludes that in Pd–Zn alloy particles *exhibiting fcc structure*, homoatomic Pd–Pd bonding interactions are stronger than heteroatomic Pd–Zn ones.

This seems to be at variance with the slab model data [237] calculated for the CuAu ($L1_0$-type) structure of Pd–Zn alloys, which correspond to considerably larger Zn concentrations [240]; the slab model results were rationalized in terms of the Pd–Zn bond strength prevailing over Pd–Pd interactions [237]. However, the alteration of the Pd–Pd and Pd–Zn bond energies in alloy moieties is caused by significantly different Pd–Pd bond lengths in the *fcc* structure of the nanoparticles and in the CuAu ($L1_0$-type) structure of slabs. Indeed, the optimized slab model distance r(Pd–Pd) = 293 pm [237] reveals considerable elongation of Pd–Pd contacts and thus, a notable *destabilization* of Pd–Pd interactions compared to those in the present cluster models, where Pd atoms are at the equilibrium Pd–Pd distance of Pd bulk, 275 pm. On the other hand, Pd–Zn interatomic spacings in the slab models (268 pm) and the cluster models (275 pm) both appear to be close to the "optimum energy" value r(Pd–Zn) ≅ 271 pm, estimated as sum of Pd and Zn atomic radii in metals, 137.6 pm (Pd) and 133.5 pm (Zn) [246]; therefore, destabilization of the Pd–Zn interaction, unlike the Pd–Pd one, is expected to be small in both the *fcc* and CuAu ($L1_0$-type) structures. These considerations indicate that the preference of

the Pd–Pd and Pd–Zn bond strengths is a very delicate property that can be affected by a mere modification of the structural arrangement of Pd–Zn alloy species due to a phase transition. Consequences of this interesting feature are important for accounting structural transformations of materials based on Pd–Zn alloys.

One of the crucial parameters characterizing the electronic structure is the cluster Fermi energy, ε_F [150]. The Fermi energies of $Pd_{140-n}Zn_n$ clusters spread over a narrow interval, from -5.20 to -4.94 eV (Table 4.5); they correlate with neither the amount nor the location of Zn atoms. The former finding is consistent with the low values of Zn admixtures. The presence of Zn atoms in the clusters slightly destabilizes the center of the Pd 4*d* band; see the energy differences $\Delta\varepsilon_{Pd4d}$ with respect to ε_F which indicate upward shifts by 0.06–0.16 eV (Table 4.5). Not unexpectedly, the relative positions $\Delta\varepsilon_{Pd4d}(Pd_3)$ of the 4*d* manifold of the three Pd atoms, which are situated in the middle of the eight hexagonal facets and form the threefold hollow adsorption site for CO probes (see Section 4.3.2), show even smaller relative upward shifts, 0.03–0.08 eV, compared to the parent cluster Pd_{140}.

Of particular interest is the charge redistribution between Pd and Zn atoms in the bimetallic clusters. However, one should keep in mind that *all* widely used approaches to assign electron density to certain atomic centers are inherently approximate, equivocal, and depend on the definition: there is no quantum mechanical observable that represents atomic charges in multinuclear moieties. In the present study, for the *qualitative* purposes, we used Mulliken charges as well as the somewhat better grounded PDCs [247] that reproduce the electrostatic field outside the clusters.

Based merely on atomic electronegativity values (Pd 1.4, Zn 1.7) [246], Zn atoms could be expected to acquire electron density. Nevertheless, Mulliken charges on Zn atoms are *positive*: 0.60 e – $Pd_{132}Zn_8$(0,8), 0.49 e – $Pd_{116}Zn_{24}$(0,24), 0.45 e – $Pd_{116}Zn_{24}$(24,0), 0.45 e for Zn(24,0) atoms and 0.64 e for Zn(0,8) atoms of $Pd_{108}Zn_{32}$(24,8). Thus, these Mulliken charges suggest electron-depleted Zn centers and this situation is corroborated by PDC values. The latter characteristics for Zn atoms are positive albeit notably smaller: 0.14 e for $Pd_{132}Zn_8$(0,8), 0.10 e for

$Pd_{116}Zn_{24}$(0,24), 0.25 e for $Pd_{116}Zn_{24}$(24,0), 0.25 e for Zn(24,0) atoms and 0.18 e for Zn(0,8) atoms of $Pd_{108}Zn_{32}$(24,8). To estimate more correctly the charge redistribution due to the introduction of Zn atoms, these PDC values should be calibrated against the charges on Pd atoms of the reference cluster Pd_{140} in the positions where Zn atoms are located. As already Pd atoms in these "Zn" positions are somewhat electronically depleted because of to the structural inequivalence of atoms in Pd_{140} [0.10 e in Zn(0,8), 0.04 e in Zn(0,24) and 0.09 e in Zn(24,0)], such a calibration results in rather modest values of the specific electron density transfer from Zn atoms in $Pd_{140-n}Zn_n$ cluster models, 0.04–0.16 e. Both Mulliken and potential-derived charges of Zn atoms are essentially defined by the position in the cluster and only slightly affected by the presence or the absence of other Zn atoms in the species.

Finally, one can try to characterize the charge state of the three Pd atoms in the center of hexagonal facets of all the moieties $Pd_{140-n}Zn_n$ which are to form the μ_3 adsorption sites. The Mulliken charges of these symmetry-equivalent Pd atoms are *negative*: –0.32 e ($4d^{8.69}5s^{1.36}5p^{0.27}$) – Pd_{140}, –0.29 e ($4d^{8.74}5s^{1.28}5p^{0.27}$) – $Pd_{132}Zn_8$(0,8), –0.33 e ($4d^{8.79}5s^{1.25}5p^{0.29}$) – $Pd_{116}Zn_{24}$(0,24), –0.45 e ($4d^{8.84}5s^{1.27}5p^{0.34}$) – $Pd_{116}Zn_{24}$(24,0), –0.42 e ($4d^{8.88}5s^{1.21}5p^{0.33}$) – $Pd_{108}Zn_{32}$(24,8). Again, PDC values support this direction of charge redistribution, although they feature significantly reduced "charging" of the Pd_3 atoms; it ranges from only –0.2 e in $Pd_{132}Zn_8$ to –0.07 e in $Pd_{116}Zn_{24}$(24,0).

B. Adsorption properties of Pd–Zn clusters

The adsorption properties of mixed-metal Pd–Zn nanoparticles and, in particular, their reactivity can be understood in terms of their electronic structure parameters. A very simplified view is that by mixing d^{10} (Pd) and $d^{10}s^2$ (Zn) atoms one obtains a material with an "average" electron configuration close to $d^{10}s^1$, i.e. the electron configuration of a Cu atom. Notwithstanding the obvious simplicity of such an argument, it helped to bridge the close similarity in the electronic structure of 1:1 Pd–Zn alloys and metallic Cu; slab model calculations had shown a similar surface reactivity of these two materials [223,236,237].

Table 4.6. Calculated characteristics[a] of adsorption complexes of model nanoclusters $Pd_{140-n}Zn_n$ with eight CO molecules on the central *hcp* Pd_3 sites of the (111) facets

Observable	Pd_{140}[b]	$Pd_{132}Zn_8$(0,8)	$Pd_{116}Zn_{24}$(24,0)	$Pd_{108}Zn_{32}$(24,8)	$Pd_{116}Zn_{24}$(0,24)
r(Pd–C), pm	206.3	207.3	207.4	206.3	203.1
r(C–O), pm	118.9	118.6	118.9	118.9	118.9
D_e, kJ mol^{-1}	169	155	169	157	121
D_e,[c] kJ mol^{-1}	142	127	142	131	91
ω(C–O), cm^{-1}	1748	1758	1751	1745	1755
ε_F, eV	-5.31	-5.38	-5.14	-5.19	-5.30
$\Delta\varepsilon_{Pd4d}$, eV	-2.09	-2.02	-2.05	-1.98	-2.01
$\Delta\varepsilon_{Pd4d}(Pd_3)$, eV	-2.44	-2.42	-2.39	-2.44	-2.67

[a] BP86 level: r(Pd–C), r(C–O) – interatomic distances, D_e – adsorption energy per CO molecule corrected for the basis set superposition error, ω(C–O) – harmonic frequency of the C–O vibration; other notations as defined in Table 4.5.

[b] Ref. 62.

[c] PBEN adsorption energy calculated for the geometry optimized at the BP level (PBEN//BP86).

Trends of the surface reactivity were illustrated, for instance, by the calculated adsorption energy of probe CO molecules at threefold-hollow sites Pd_2Zn of PdZn(111) surface, 1.0 eV (obtained with the PW91 xc potential [162]); this value is close to that on the Cu(111) surface, ~0.9 eV, but differs considerably from the energy of μ_3-CO adsorbed on the Pd(111) surface, ~1.9 eV [236]. The finding that CO binds weaker to the surface of PdZn alloy than to monometallic Pd agrees with experimental observations for PdZn and Pd polycrystalline samples [234]. Thus, on Pd–Zn particles that manifest local and overall concentrations Pd:Zn higher than 1:1 it is also reasonable to expect a notable reduction of CO adsorption energies compared to those on the corresponding adsorption sites of monometallic Pd particles. In this sense, results described in the following paragraph were unexpected and deserve special remarks.

Before starting the present computational work on highly symmetric nanoparticle models, we had carried out a series of BP86 calculations on conventional ("planar") three-layer cluster models $Pd_{28-n}Zn_n$ (C_{3v} symmetry) with 12, 10 and 6 atoms in the first, second and third layer, respectively. We considered adsorption of a single CO molecule at the *hcp* site of the cluster models Pd_{28}, $Pd_{27}Zn_1(0,1)$, $Pd_{25}Zn_3(3,0)$, $Pd_{24}Zn_4(3,1)$ and $Pd_{22}Zn_8(0,6)$, where the central Pd_3 unit of the upper layer was kept throughout. Quite unexpectedly, substitution of Pd by Zn resulted in an increase of the CO adsorption energy with respect to the value of 151 kJ mol^{-1} computed for the monometallic cluster Pd_{28}. We had studied three Pd–Zn models: (i) Zn substitution underneath the *hcp* site, $Pd_{27}Zn_1(0,1)$, (ii) in the upper layer nearby the central Pd_3 moiety, $Pd_{25}Zn_3(3,0)$, as well as (iii) in the both positions, $Pd_{24}Zn_4(3,1)$. The calculated CO adsorption energies were 6 kJ mol^{-1}, 23 kJ mol^{-1}, and 49 kJ mol^{-1}, larger than on the reference model CO/Pd_{28}. Only for the model $Pd_{22}Zn_6(0,6)$, the adsorption energy of CO was calculated slightly, by 9 kJ mol^{-1}, smaller than for the reference. Our attempts to rationalize these counterintuitive results in terms of varying donation/back-donation propensity of the model systems $Pd_{28-n}Zn_n$ failed. Finally, we attributed the adsorption energy behavior to the cluster size effects [219] which appeared to be still significant even for these moderately large metal substrate particles [62]. Actually, this latter observation was one of the important motivations to introduce and employ highly-symmetric three-dimensional cluster models which are essentially free of size effects even for the most critical observable, namely the adsorption energy [61,62,206].

The calculated characteristics of μ_3-CO adsorption complexes with three-dimensional nanocluster models $Pd_{140-n}Zn_n$ are displayed in Table 4.6.

The calculated bond distances exhibit only a limited variation over the series of adsorption complexes under investigation. The computed C–O distance, ~119 pm, is very stable and varies less than 1 pm. Due to σ donation and π^* back-donation interactions with the substrate, it is elongated by 5 pm and 6 pm compared to the calculated [62] and experimental [248] values for free CO molecules, respectively. (A detailed experimental and theoretical analysis actually allows one

to discriminate three-orbital interactions in the σ as well as the π channels [249].) The Pd–C distance, 206-207 pm, is also quite stable throughout, except for the model $(CO)_8/Pd_{116}Zn_{24}(0,24)$, 203 pm, which features Zn–Zn nearest-neighbor contacts that are absent in all other models inspected.

Adsorption energies were calculated for CO geometries optimized with the BP86 xc potential at both the BP86 and the PBEN levels (see Subsection 4.2.2); in passing we note that we had found the PBEN energetics for CO adsorption on Pd to be most accurate, in a quantitative agreement with experiment [62]. For the cluster $Pd_{132}Zn_8(0,8)$ with eight Zn atoms located in the subsurface region, just beneath the central Pd_3 moiety on each hexagonal facet (Figure 4.5b), the CO adsorption energy decreased by about 10 % compared to the reference $(CO)_8/Pd_{140}$. Interestingly, the CO adsorption energy remains essentially unchanged when three more Zn atoms substitute Pd atoms on every hexagonal facet, resulting in the cluster $Pd_{108}Zn_{32}(24,8)$ (Figure 4.5d): 157 kJ mol^{-1} vs. 155 kJ mol^{-1} (BP86) and 127 kJ mol^{-1} vs. 131 kJ mol^{-1} (PBEN). Apparently, Zn atoms in the upper layer [in the configuration (24,0)] at larger distances from the central Pd_3 unit exert only a minor effect on the CO adsorption energetics. This finding is corroborated by the equal CO binding energies on the cluster models $Pd_{116}Zn_{24}(24,0)$ and Pd_{140}, 169 kJ mol^{-1} (BP86) and 142 kJ mol^{-1} (BPEN); these two models differ only by $Zn_{24}(24,0)$ atoms. Short Zn–Zn contacts, the new feature of the cluster $Pd_{116}Zn_{24}(0,24)$, affect the adsorption propensity of CO molecules most noticeably, as anticipated: the binding energy values, 121 kJ mol^{-1} (BP86) or 91 kJ mol^{-1} (PBEN), are 48 kJ mol^{-1} smaller.

One can see from Table 4.6 that calculated C–O vibrational frequencies on various substrate clusters $Pd_{140-n}Zn_n$ spread over a rather narrow interval 1752±7 cm^{-1}. Such a range of C–O frequencies considerably shifted down from the value of gas-phase CO molecules (with a calculated harmonic frequency of 2113 cm^{-1}) is typical for CO species adsorbed on transition metals and is attributed to back-donation interaction from metal *d*-orbitals to the antibonding π* orbital of CO [62,219]. Our results reflect the local character of the C–O vibrations and of the back-donation. This vibrational mode is hardly sensitive to the more distant

environment of the metal substrate; recall that the moiety Pd_3–CO is common to all models considered here, only surrounding Pd atoms are substituted by Zn. This local nature of the vibrational properties is the main reason why already small cluster models usually suffice for an accurate simulation of molecular vibrations at transition metal surfaces [250] and why this kind of observables do not exhibit a substantial cluster size dependence. At variance, the adsorption energy is a property that reflects the characteristics of metal surfaces in a global fashion [62,206,219]. This inherent difference allows one to understand why calculated CO adsorption energies and C–O stretching frequencies on $Pd_{140-n}Zn_n$ clusters do not show any correlation (Table 4.6).

Two types of mechanisms come to mind that influence the adsorption properties of bimetallic systems: geometric (ensemble, site, or dilution) factors and electronic effects, also known as ligand effects, which originate from alloying [251]. By keeping the Pd_3 moiety at the adsorption site, in immediate vicinity of the CO adsorbate, unchanged we suppressed structural factors and focused on electronic effects.

The adsorption-induced alteration of the electronic structure of $Pd_{140-n}Zn_n$ nanoparticles is best reflected in the stabilization of the Fermi energy ε_F in all the species investigated. This change is indicative of the electron density acquired by CO molecules via π^* back-donation which prevails over σ donation [249]. The stabilization is essentially the same, 0.18–0.20 eV, for all the adsorption systems except $(CO)_8/Pd_{116}Zn_{24}(0,24)$, which again deviates and furnishes a notably smaller stabilization of ε_F, 0.13 eV (Table 4.5 and 4.5). This reduced downward shift of ε_F is in line with notably weaker adsorption bonds in $(CO)_8/Pd_{116}Zn_{24}(0,24)$ than in other analogs (Table 4.6). Indeed, this finding can be rationalized by relating the adsorption energy of CO to the amount of electron density back-donated to its π^* orbitals from the metal substrate; all other conditions being equal (as is the case in the present situation), smaller back-donation is accompanied by weaker metal–CO interaction; in turn, a reduced amount of electron density withdrawn from the metal species implies a smaller adsorbate-induced stabilization of the Fermi energy ε_F.

The somewhat exceptional electronic structure properties of the system $(CO)_8/Pd_{116}Zn_{24}(0,24)$ are corroborated by the relative positions of the total Pd 4*d* band center $\Delta\varepsilon_{Pd4d}$, 0.12 eV vs. 0.03-0.06 eV, and the Pd 4*d* center $\Delta\varepsilon_{Pd4d}(Pd_3)$ of the three Pd atoms defining the μ_3 adsorption site, 0.63 eV vs. 0.37-0.43 eV (Table 4.5 and Table 4.6).

4.2.4 Conclusions

In the present section, we extended the modeling strategy based on high-level electronic structure calculations of three-dimensional metal nanoparticles to investigate bimetallic Pd–Zn species with low Zn atom concentrations varying up to ~25 %. We studied the influence of the number of Zn atoms and their location on the electronic structure and stability of $Pd_{140-n}Zn_n$ clusters with the structural arrangement derived from the bulk of *fcc* metals. The calculated average cluster cohesive energy decreases gradually with increasing number of Zn atoms: each Zn atom destabilizes the cluster by ~1 eV. We also found that Zn atoms preferentially occupy positions in the surface layer of the model clusters and we identified a small transfer of electron density from Zn to Pd atoms.

For complexes with CO molecules adsorbed at threefold hollow Pd_3 sites of the hexagonal cluster facets, we explored how adsorption properties of bimetallic models change with respect to those of the reference cluster Pd_{140}. Calculated CO adsorption energies manifest a weakening of adsorbate-substrate interactions when Zn atoms are located in the subsurface layer of $Pd_{140-n}Zn_n$ clusters; on the other hand, Zn atoms in the surface layer seem to affect the CO adsorption energy only marginally. The absence of a correlation between calculated CO adsorption energies and vibrational C–O frequencies is assigned to the different nature of these properties: the former are *global* characteristics of adsorption systems whereas the latter are mainly due to *local* effects.

Chapter 5

Summary and Prospects

We performed theoretical studies of structure and properties of *d*-metal species, covering the range from monatomic supported particles to clusters of nanometer size. To this end, we employed an accurate all-electron density functional method, using a scalar-relativistic variant for transition metals from the second row onward. Calculations were carried out at the GGA level using the BP86 and PBEN exchange-correlation functionals. For MgO(001)-supported particles, we employed a novel, advanced scheme of cluster embedding in an elastic polarizable environment (EPE) (Chapter 3). These particles included single *d*-metal atoms as well as dimers, trimers and tetramers of Cu, Ag and Au on regular and oxygen vacancy sites of MgO(001). We quantified structural and energetic parameters of these adsorption complexes and we elucidated their propensity regarding the cluster growth on various sites. We predicted ionization potentials to connect the modeling with experiments. Pd_n (n = 79–146) and $Pd_{140-n}Zn_n$ (n = 0–32) nanoparticles with the dimensions exceeding 1 nm were described as symmetric three-dimensional models (Chapter 4). Their adsorption properties were examined by interactions with CO probes on the bare clusters and those pre-covered by atomic C impurities featuring a carbidic nature.

In Chapter 3 metal atom adsorption has been studied on regular O^{2-} sites as well as on F_s and F_s^+ defects of relaxed surface terraces of MgO(001). 17 single *d*-

metal adatoms of the third, fourth, and fifth rows of the periodic table were considered: Cr, Mo, W; Mn, Re; Fe, Ru, Os; Co, Rh, Ir; Ni, Pd, Pt; Cu, Ag, Au. The EPE embedding method used treats both the central quantum mechanical region of the oxide clusters under study and their classical environment variationally, without artificial constraints for geometry optimization. Even on a rigid substrate such as ideal MgO(001), adsorbate-induced relaxation noticeably affects structure and stability of surface complexes. For more reliable estimates, we calculated adsorption energies with two different gradient-corrected exchange-correlation functionals, BP86 and PBEN. More than one electron configuration was considered for metal atoms adsorption complexes with exhibiting high-spin states.

The calculated results corroborate the general picture of the interactions with regular sites and oxygen vacancies on MgO terraces derived from earlier studies of selected metal atoms. The adsorption bonds of single metal atoms with O^{2-} sites can be described as metal polarization accompanied by (some) orbital mixing, but without noticeable adsorbate-substrate charge transfer.

With few exceptions, interactions with oxygen vacancies are significantly stronger than with regular sites and they are accompanied by a notable transfer of electron density from an F_s site to a *d*-metal adsorbate. In most groups, 4*d*-atoms are adsorbed stronger than 3*d*-atoms, but weaker than 5*d*-atoms, on both kinds of defects studied. This is at variance with the trend in binding energies within each group, $4d < 3d < 5d$, established for M/O^{2-} complexes. As for the energy variation along the period, in both F_s and F_s^+ complexes, atoms of group 7 are slightly destabilized with respect to their group 6 analogs. Then, within a period, the binding energy increases gradually up to group 10 species and finally it decreases again for group 11, most prominently on F_s sites. These trends appear to be governed by the negative charge on adsorbed atoms and their concomitant electrostatic interactions with the vacancy sites of MgO(001) terraces.

The bonding in M/F_s^+ complexes is in general notably weaker than in their M/F_s analogs. We attribute this difference mainly to electrostatic stabilization of the latter species as a consequence of significant accumulation of electron density on the adsorbed atoms M, donated by the F_s vacancy. Covalent interactions may

counteract this electrostatic stabilization and even alter the trend, making some M/F_s^+ complexes favored over their M/F_s congeners, as is the case for M = Cu, Ag and Au.

XPS core-level shifts of adsorbed metal atoms on MgO(001), approximated as differences of Kohn-Sham eigenvalues, revealed a characteristic dependence on the adsorption site. In combination with experimental XPS data, these calculated data open a way to distinguish between the M/F_s and M/F_s^+ structures on (001) terraces of MgO.

An extension of this work on single deposited metal atoms on MgO(001) should be a detailed study of interactions with neutral and positively charged oxygen vacancies at lower coordinated surface sites of MgO, e.g. at steps, edges and corners, where the formation of vacancies is more justified thermodynamically. The important question is, whether these low-coordinated color centers are stronger traps for single metal atoms than the vacancies on (001) terrace.

Next, we studied the adsorption of small coinage metal aggregates M_n (M = Cu, Ag, Au; n = 2, 3, 4) on the ideal MgO(001) as well as on oxygen vacancies, F_s and F_s^+ using the same computational approach as for the atomic adsorbates. We identified most favorable adsorption geometries and compared the three congeners of the Cu subgroup. In the same way as single adsorbed atoms, metal moieties on regular O^{2-} surface sites are polarized and interact mainly by electrostatic attraction, counteracted by Pauli repulsion. Binding to oxygen vacancies, to F_s sites in particular, is notably stronger than to regular O^{2-} sites, for two reasons. Pauli repulsion is reduced and the electron density of the adsorbate as well as that of a vacancy are easier to polarize. Furthermore, at neutral defect sites, a notable transfer of electron density from the vacancy to the adsorbed metal species contributes to stronger binding. The adsorption energy per atom decreases from dimers to trimers in line with the fact that metal-metal cohesion dominates over metal-oxide interaction. Based on calculated interaction energies, we conclude that dimerization of adsorbed coinage atoms on F_s sites is not particularly favored compared to dimerization on flat terraces. Dimerization on F_s^+ sites, which has not been considered theoretically before, is clearly unfavorable.

The adsorption properties of deposited Cu_4, Ag_4 and Au_4 species were studied only at the regular MgO(001) surface. In the gas phase, all three tetramers were calculated to exhibit a planar rhombic structure with closed electronic shells. Geometries of the supported tetramers were found to be similar to those in the gas phase, i.e. the rhombus structure experiences only minor distortions due to interactions with the surface. All three tetramers favor the same type of adsorption complex, namely upright orientation of the metal particle, perpendicular to the surface, with two metal centers attached to surface oxygen anions. Such an upright adsorption mode can be rationalized by the fact that the interaction of coinage metal particles on regular sites of the ionic oxide is primarily of polarization character. Similarly to dimer and trimer complexes, Au_4 exhibits the strongest adsorption interaction on MgO(001), followed by Cu_4 and Ag_4. The propensity of small supported metal particles to dimerize, giving adsorbed tetramers, has been quantified and rationalized.

In general, cluster growth on oxide supports is a complicated phenomenon, significantly affected by the type of metal as well as of the type of sites on the oxide surface involved in the very first stage of the metal nucleation on supports. Therefore, high-level electronic structure calculations of adequate models are of special importance for providing and unraveling (often unique) information on the surface-mediated metal dimerization and further steps of the growing processes.

Do describe large particles of model catalysts, we studied mono- and bimetallic clusters with diameters of about 1 nm or more (Chapter 4).

Adsorbed atomic C species can be formed in the course of surface reactions and commonly decorate metal catalysts. We addressed C adsorption on nanoclusters Pd_{55}, Pd_{79}, Pd_{85}, Pd_{116}, Pd_{140} and Pd_{146} chosen as fragments of bulk Pd in the form of three-dimensional octahedral or cuboctahedral crystallites, which expose (111) and (100) facets as well as edge sites. These cluster models were shown to yield size-converged adsorption energies of carbon atoms. We examined which surface sites of these clusters are preferentially occupied by adsorbed C. Surface C atoms form strongly adsorbed carbide species, with calculated adsorption energies of more than 600 kJ mol^{-1}, bearing a significant negative charge. Surface sites allowing high, 4-

fold coordination of carbon were found to be favored overall. To avoid effects of adsorbate-adsorbate interaction in the cluster models for carbon species in the vicinity of cluster edges, we reduced the *local* symmetry of selected adsorption complexes on the nanoclusters by lowering the *global* symmetry of the nanocluster models from point group O_h to D_{4h}. On (111) facets, 3-fold hollow sites in the center are energetically preferred; adsorbed C was calculated to be slightly less stable when displaced to the facet borders. We did not find any energy gain due to enhanced adsorbate-substrate interactions at regular sites near the boundaries (edges) of (111) facets, as anticipated in experimental studies. Our results call for another rationalization of the experimental findings.

The symmetry reduction just mentioned represents an important extension of the novel strategy to employ three-dimensional cluster models in studies of adsorption and reactivity. Indeed, on three-dimensional metal nanoclusters with symmetry lower than O_h, e.g. D_{4h}, one can accommodate adsorption complexes which feature *local* C_{2v} symmetry, rather than atoms or "up-right" linear molecules as done previously. In addition, these models admit low coverage, with only one adsorbate per (111) facet. If a locally completely asymmetric adsorbate or a transition state complex is to be considered, reduction to *global* D_4 symmetry would suffice within the present nanocluster scheme. Such lower-symmetry studies of the reactivity of 3D nanoparticles are feasible with the help of the contemporary computer hard- and software and they will certainly soon comprise an important extension of the work described in this thesis.

Finally, we studied bimetallic cuboctahedral nanoscale clusters $Pd_{140-n}Zn_n$ (n = 0, 8, 24, 32) as local models of the active component of novel Pd/ZnO catalysts for methanol steam reforming. Such compact model clusters can provide a quantitatively accurate description of adsorption properties of single crystal metal surfaces as well as supported metal particles. By this work we extended the modeling strategy based on high-level electronic structure calculations of three-dimensional metal nanoparticles to investigate bimetallic Pd-Zn species with low concentrations of Zn atoms. The calculated average cluster cohesive energy decreases gradually when the number of Zn atoms increases: each of them

introduces a destabilization by ~1 eV. Zn atoms preferentially occupy positions in the surface layer of the clusters. A small transfer of electron density from Zn to Pd atoms was found. To probe how adsorption properties of bimetallic species change relative to those of the reference cluster Pd_{140}, we studied complexes with CO molecules adsorbed on threefold hollow Pd_3 sites of (111) cluster facets. CO adsorption energies were calculated notably smaller when Zn atoms are located in the subsurface layer of the clusters; on the other hand, Zn atoms in the surface layer affected the CO adsorption energy only slightly. Calculated CO adsorption energies and vibrational C–O frequencies do not correlate, reflecting the different origin of these properties: the former are *global* characteristics of adsorption systems whereas the latter are mainly due to *local* effects.

Bibliography

[1] H.-J. Freund, Surf. Sci. 500 (2002) 271.

[2] W. Eberhardt, Surf. Sci. 500 (2002) 242.

[3] G. Ertl, H. Knözinger, J. Weitkamp (Eds.), Environmental Catalysis; Wiley-VCH: Weinheim, 1999.

[4] G. Ertl, H. Knözinger, J. Weitkamp (Eds.), Handbook of Hetrogenoeous Catalysis, Vol. 4; Wiley-VCH Verlagsgesellschaft mbH: Weinheim, 1997.

[5] J.M. Thomas, W.J. Thomas, Principle and Practice of Heterogenous Catalysis; Wiley-VCH: Weinheim, 1997.

[6] A.M. Doyle, S.K. Shaikhutdinov, S.D. Jackson, H.-J. Freund, Angew. Chem. Int. Ed. 42 (2003) 5240.

[7] J. Libuda, M. Frank, A. Sandell, S. Andersson, P.A. Brühwiler, M. Bäumer, N. Martensson, H.-J. Freund, Surf. Sci. 384 (1997) 106.

[8] N. Magg, S. Giorgio, M. Frank, B. Immaraporn, T. Schröder, M. Bäumer, H.-J. Freund, J. Am. Chem. Soc. 126 (2004) 3616.

[9] M. Heemeier, A.F. Carlsson, N. Naschitzki, M. Schmal, M. Bäumer, H.-J. Freund, Angew. Chem. Int. Ed. 41 (2002) 4073.

[10] A. Carlsson, N. Naschitzki, M. Bäumer, H.-J. Freund, J. Chem. Phys. 119 (2003) 10885.

[11] S. Shaikhutdinov, M. Frank, M. Bäumer, S.D. Jackson, R. Oldman, J.C. Hemminger, H.-J. Freund, Catal. Lett. 80 (2002) 115.

[12] Sensors Update, H. Baltes, W. Gospel, J. Hesse (Eds.), Sensor Technology Applications–Markets, Vol. 1; Wiley-VCH Verlagsgesellschaft mbH: Weinheim, 1996.

[13] H. Ulmer, J. Mitrovics, G. Noetzel, U. Weimar, W. Göpel, Sens. Actuators B 43 (1997) 24.

[14] I. Lundström, Sens. Actuators A 56 (1996) 75.

[15] First Toyota Workshop on Magnetism and Magnetic Materials for High Density Information Storage, Toyota Institute of Technology, J. Magn. Magn. Mater., Vol. 175; Elsevier: Brussels, Belgium, 1997.

[16] M. Bäumer, H.-J. Freund, Prog. Surf. Sci. 61 (1999) 127.

[17] A.K. Santra, D.W. Goodman, J. Phys. Condens. Matter. 14 (2002) R31.

[18] C.R. Henry, Surf. Sci. Rep. 31 (1998) 231.

[19] V.P. Zhdanov, B. Kasemo, Surf. Sci. Rep. 39 (2000) 25.

[20] D.W. Goodman, J. Catal. 216 (2003) 213.

[21] R.M. Jaeger, H. Kuhlenbeck, H.-J. Freund, M. Wuttig, W. Hoffmann, R. Franchy, H. Ibach, Surf. Sci. 259 (1991) 235.

[22] W. Weiss, W. Ranke, Prog. Surf. Sci. 70 (2002) 1.

[23] C.C. Chusuei, X. Lai, K. Luo, D.W. Goodman, Top. Catal. 14 (2001) 71.

[24] R.M. Lambert, G. Pacchioni (Eds.), Chemisorption and Reactivity on Supported Clusters and Thin Films; NATO ASI Series E, Vol. 331; Kluwer: Dordrecht, 1997.

[25] N. Rösch, V.A. Nasluzov, K.M. Neyman, G. Pacchioni, G.N. Vayssilov, Computational Material Science, Theoretical and Computational Chemistry, Vol. 15; J. Leszczynski (Eds.); Elsevier: Amsterdam, 2004.

[26] I.V. Yudanov, G. Pacchioni, K.M. Neyman, N. Rösch, J. Phys. Chem. B 101 (1997) 2786.

[27] H. Grönbeck, P. Broqvist, J. Chem. Phys. 119 (2003) 3896.

[28] A. Markovits, J.C. Paniagua, N. Lopez, C. Minot, F. Illas, Phys. Rev. B 67 (2003) 115417.

[29] Yu.F. Zhukovskii, E.A. Kotomin, G. Borstel, Vacuum 74 (2004) 235.

[30] A.V. Matveev, K.M. Neyman, I.V. Yudanov, N. Rösch, Surf. Sci. 426 (1999) 123.

[31] A.M. Ferrari, G. Pacchioni, J. Phys. Chem. 100 (1996) 9032.

[32] L.N. Kantorovich, A.L. Shluger, P.V. Sushko, J. Gunster, P. Stracke, D.W. Goodman, V. Kempter, Faraday Discuss. 114 (1999) 173.

[33] A. Bogicevic, D.R. Jennison, Surf. Sci. 437 (1999) L741.

[34] V.A. Nasluzov, V.V. Rivanenkov, A.B. Gordienko, K.M. Neyman, U. Birkenheuer, N. Rösch, J. Chem. Phys. 115 (2001) 8157.

[35] Z.X. Yang, R.Q. Wu, Q.M. Zhang, D.W. Goodman, Phys. Rev. B 65 (2002) 155407.

[36] A. Bogicevic, D.R. Jennison, Surf. Sci. 515 (2002) L481.

[37] K.M. Neyman, C. Inntam, A.V. Matveev, V.A. Nasluzov, N. Rösch, J. Am. Chem. Soc. 127 (2005) 11652.

[38] K.M. Neyman, C. Inntam, V.A. Nasluzov, R. Kosarev, N. Rösch, Appl. Phys. A 78 (2004) 823.

[39] C. Inntam, L.V. Moskaleva, K.M. Neyman, V.A. Nasluzov, N. Rösch, Appl. Phys. A

(2005), DOI: 10.1007/s00339-005-3352-8.

[40] A.M. Ferrari, C. Xiao, K.M. Neyman, G. Pacchioni, N. Rösch, Phys. Chem. Chem. Phys. 1 (1999) 4655.

[41] M. Moseler, H. Häkkinen, U. Landman, Phys. Rev. Lett. 89 (2002) 176103.

[42] L. Giordano, C. Di Valentin, J. Goniakowski, G. Pacchioni, Phys. Rev. Lett. 92 (2004) 096105.

[43] A. Del Vitto, C. Sousa, F. Illas, G. Pacchioni, J. Chem. Phys. 121 (2004) 7457.

[44] Ž. Šljivančanin, A. Pasquarello, Phys. Rev. Lett. 90 (2003) 247202.

[45] V. Musolino, A. Selloni, R. Car, J. Chem. Phys. 108 (1998) 5044.

[46] V. Musolino, A. Selloni, R. Car, Phys. Rev. Lett. 83 (1999) 3242.

[47] G. Haas, A. Menck, H. Brune, J.V. Barth, J.A. Venables, K. Kern, Phys. Rev. B 61 (2000) 11105.

[48] I. Alstrup, P.J. Møller, Appl. Surf. Sci. 33-34 (1988) 143.

[49] M. Meunier, C.R. Henry, Surf. Sci. 307-309 (1994) 514.

[50] M. Bäumer, M. Frank, M. Heemeier, R. Kühnemuth, S. Stempel, H.-J. Freund, Surf. Sci. 454-456 (2000) 957.

[51] V.A. Nasluzov, E.A. Ivanova, A.M. Shor, G.N. Vayssilov, U. Birkenheuer, N. Rösch, J. Phys. Chem. B 107 (2003) 2228.

[52] H.-J. Freund, Faraday Discuss. 114 (1999) 1.

[53] J. Libuda, S. Schauermann, M. Laurin, T. Schalow, H.-J. Freund, Monat. Chem. 136 (2005) 59.

[54] S. Schauermann, J. Hoffmann, V. Johánek, J. Hartmann, J. Libuda, H.-J. Freund, Angew. Chem. Int. Ed. Engl. 41 (2002) 2532.

[55] K.M. Neyman, C. Inntam, A.B. Gordienko, I.V. Yudanov, N. Rösch, J. Chem. Phys. 122 (2005) 174705, 1-9.

[56] K.M. Neyman, R. Sahnoun, C. Inntam, S. Hengrasmee, N. Rösch, J. Phys. Chem. B 108 (2004) 5424.

[57] N. Takezawa, N. Iwasa, Catal. Today 36 (1997) 45.

[58] M.L. Cubeiro, J.L.G. Fierro, J. Catal. 179 (1998) 150.

[59] J.A. Rodriguez, J. Phys. Chem. 98 (1994) 5758.

[60] J.A. Rodriguez, M. Kuhn, J. Phys. Chem. 100 (1996) 381.

[61] I.V. Yudanov, R. Sahnoun, K.M. Neyman, N. Rösch, J. Hoffmann, S. Schauermann, V. Johánek, H. Unterhalt, G. Rupprechter, J. Libuda, H.-J. Freund, J. Phys. Chem. B

107 (2003) 255.

[62] I.V. Yudanov, R. Sahnoun, K.M. Neyman, N. Rösch, J. Chem. Phys. 117 (2002) 9887.

[63] V.E. Henrich, P.A. Cox, The Surface Science of Metal Oxides, Cambridge Univ. Press: Cambridge, UK, 1994.

[64] C. Noguera, Physics and Chemistry of Oxide Surfaces, Cambridge Univ. Press: Cambridge, UK, 1996.

[65] C. Claeys, C.R. Henry, C. Chapon, Meas. Sci. Technol. 2 (1991) 81.

[66] H.-J. Freund, H. Kuhlenbeck, V. Staemmler, Rep. Progr. Phys. 59 (1996) 283.

[67] A.P. Janssen, R.C. Schoonmaker, A. Chambers, Surf. Sci. 49 (1975) 143.

[68] C. Duriez, C. Chapon, C.R. Henry, J.M. Rickard, Surf. Sci. 230 (1990) 123.

[69] D. Abriou, F. Creuzet, J. Jupille, Surf. Sci. 352-354 (1996) 499.

[70] S. Coluccia, A.J. Tench, R.L. Segall, J. Chem. Soc. Faraday Trans. I 75 (1979) 1769.

[71] J.W. He, P.J. Möller, Surf. Sci. 178 (1986) 934.

[72] A. Pojani, E. Finocchi, J. Goniakowski, C. Noguera, Surf. Sci. 387 (1997) 354.

[73] C.A. Ventrice, Th. Bertrams, H. Hannemann, A. Brodde, H. Neddermeyer, Phys. Rev. B 49 (1994) 5773.

[74] C.T. Campbell, A. Ludviksson, J. Vac. Sci. Technol. A 12 (1994) 1825.

[75] M. Sambi, G. Granozzi, G. Rizzi, M. Casarin, E. Tondello, Surf. Sci. 319 (1994) 149.

[76] E.E. Wasserman, K.A. Polacek, Surf. Sci. 28 (1971) 77.

[77] H. Jacobs, W. Mokwa, D. Kohl, G. Heiland, Surf. Sci. 160 (1985) 217.

[78] E. Gillet, B. Ealet, Surf. Sci. 273 (1992) 427.

[79] M. Gautier, G. Renaud, L. Pham Van, B. Villette, M. Pollak, N. Thromat, E. Joliet, J.P. Duraud, J. Am. Ceram. 77 (1994) 323.

[80] H. Poppa, Ultramicroscopy 11 (1983) 105.

[81] H. Poppa, C.A. Papageorgopoulos, E. Marks, E. Bauer, Z. Phys. D 3 (1986) 279.

[82] G. Renaud, B. Villette, I. Vilfan, A. Bourret, Phys. Rev. Lett. 73 (1994) 1825.

[83] M.C. Wu, P.J. Möller, Surf. Sci. 224 (1989) 250.

[84] C.C. Kao, S.C. Tsai, Y.W. Chung, J. Catal. 73 (1982) 136.

[85] S. Bourgeois, P. le Seigneur, M. Perdereau, Surf. Sci. 328 (1995) 105.

[86] A. Szabo, T. Engel, Surf. Sci. 329 (1995) 241.

[87] H. Onishi, T. Aruga, C. Egawa, Y. Iwasawa, Surf. Sci. 233 (1990) 261.

[88] O. Madelung (Eds.), Semiconductors: Physics of II-VI and I-VII Compounds, Semimagnetic Semiconductors, Landoldt Bornstein New Series III, 17b, Springer-Verlag, Berlin, 1972.

[89] A.K. Santra, D.W. Goodman, J. Phys. Condens. Matter. 14 (2002) R31.

[90] Z.M. Jarzebski, J.P. Marton, J. Electrochem. Soc. 123 (1976) 299C.

[91] R. Souda, T. Dizava, Y. Ishezava, C. Oshima, J. Vac. Sci. Technol. A 8 (1990) 3218.

[92] N. Ikemiya, A. Kitamura, S. Hara, J. Cryst. Growth 160 (1996) 104.

[93] S.S. Perry, P.B. Merrill, Surf. Sci. 383 (1997) 268.

[94] P.M. Thibado, G.S. Rohrer, D.A. Bonnell, Surf. Sci. 318 (1994) 379.

[95] D.W. Goodman, J. Vac. Sci. Technol. A 14 (1996) 1526.

[96] H.-J. Freund, B. Billmann, D. Ehrlich, M. Hassel, R.M. Jaeger, K. Kuhlenbeck, C.A. Ventrice Jr., E. Winkelmann, S. Wohlrab, C. Xu, Th. Bertrams, H. Brodde, H. Neddermeyer, J. Mol. Catal. 82 (1993) 143.

[97] C.R. Henry, H. Poppa, Thin Solid Films 189 (1990) 303.

[98] S. Giorgio, H. Graoui, C. Chapon, C.R. Henry, Mater. Sci. Eng. A 229 (1997) 169.

[99] C.R. Henry, H. Poppa, J. Vac. Sci. Technol. A 6 (1988) 1113.

[100] C. Chapon, C.R. Henry, A. Chemam, Surf. Sci. 162 (1985) 747.

[101] M.C. Wu, J.S. Corneille, C.A. Estrada, J.W. He, D.W. Goodman, Chem. Phys. Lett. 182 (1991) 472.

[102] C.M. Truong, M.C. Wu, D.W. Goodman, J. Chem. Phys. 97 (1992) 9447.

[103] M.C. Gallagher, M.S. Fyfield, J.P. Cowin, S.A. Joyce, Surf. Sci. 339 (1995) L909.

[104] J.G. Chen, J.E. Crowell, J.T. Yates, Surf. Sci. 187 (1987) 243.

[105] R.M. Jaeger, H. Kuhlenbeck, H.-J. Freund, M. Wuttig, W. Hoffmann, R. Franchy, H. Ibach, Surf. Sci. 259 (1991) 235.

[106] X.D. Peng, M.A. Barteau, Appl. Surf. Sci. 44 (1990) 87.

[107] J.G. Chen, J.E. Crowell, J.T. Yates, Surf. Sci. 185 (1987) 373.

[108] G. Pacchioni, ChemPhysChem 4 (2003) 1041.

[109] S. Coluccia, S. Lavagnino, L. Marchese, Mater. Chem. Phys. 18 (1998) 445.

[110] A.M. Ferrari, G. Pacchioni, J. Phys. Chem. 99 (1995) 17010.

[111] A.M. Ferrari, G. Pacchioni, J. Phys. Chem. 100 (1996) 9032.

[112] L.G.M. Pettersson, G. Pacchioni, Chem. Phys. Lett. 219 (1994) 107.

[113] R. Schaub, E. Wahlström, A. Rønnau, E. Laegsgaard, I. Stensgaard, F. Besenbacher, Science 299 (2003) 377.

[114] C.T. Campbell, D.E. Sterr, J. Am. Chem. Soc. 124 (2002) 9212.

[115] J. Evans, B.E. Hayden, M.A. Newton, Surf. Sci. 462 (2000) 169.

[116] A.M. Argo, B.C. Gates, J. Phys. Chem. B 107 (2003) 5519.

[117] U. Heiz, E.L. Bullock, J. Mater. Chem. 14 (2004) 564.

[118] K. Judai, S. Abbet, A.S. Worz, U. Heiz, C.R. Henry, J. Am. Chem. Soc. 126 (2004) 2732.

[119] M. Gustavsson, H. Fredriksson, B. Kasemo, Z. Jusys, J. Kaiser, C. Jun, R.J. Behm, J. Electroanal. Chem. 568 (2004) 371.

[120] B. Kasemo, S. Johansson, H. Persson, P. Thormählen, V.P. Zhdanov, Top. Catal. 2000 (2000) 43.

[121] K. Wong, S. Johansson, B. Kasemo, Faraday Discuss. 105 (1996) 237.

[122] Th. Hill, M. Mozaffari-Afshar, J. Schmidt, Th. Risse, S. Stempel, M. Heemeier, H.-J. Freund, Chem. Phys. Lett. 292 (1998) 524.

[123] C.T. Campbell, Surf. Sci. Rep. 27 (1997) 1.

[124] J.A. Venables, G.D.T. Spiller, M. HanbuÈcken, Rep. Prog. Phys. 47 (1984) 399.

[125] C.R. Henry, C. Chapon, S. Giorgio, C. Goyhenex, Chemisorption and Reactivity on Supported Clusters and Thin Films, NATO ASI Series E, Vol. 331; R.M. Lambert, G. Pacchioni (Eds.); Kluwer: Dordrecht, 1997.

[126] M. Zinke-Allmang, L.C. Feldman, M.H. Grabow, Surf. Sci. Rep. 16 (1992) 377.

[127] E. Bauer, Z. Kristallogr. 110 (1958) 372.

[128] S.H. Overbury, P.A. Bertrand, G.A. Somorjai, Chem. Rev. 75 (1975) 547.

[129] D.W. Goodman, Surf. Rev. Lett 2 (1995) 9.

[130] R. Persaud, T.E. Madey, Growth and Properties of Ultra thin Epitaxial Layers, D.A. King, D.P. Woodruff (Eds.); Elsevier: Amsterdam, 1997.

[131] M. Bäumer, J. Libuda, H.-J. Freund, Chemisorption and Reactivity on Supported Clusters and Thin Films, NATO ASI Series E, Vol. 331; R.M. Lambert, G. Pacchioni (Eds.); Kluwer: Dordrecht, 1997.

[132] D. Chatain, L. Coudurier, N. Eustathopoulos, Rev. Phys. Appl. 23 (1988) 1055.

[133] G. Rupprechter, K. Hayek, L. Rendon, M.J. Yacaman, Thin Solid Films 260 (1995) 148.

[134] C.R. Henry, C. Chapon, C. Duriez, S. Giorgio, Surf. Sci. 253 (1991) 177.

[135] P.M. Ajayan, L.D. Marks, Phys. Rev. Lett. 63 (1989) 279.

[136] G. Schmid, M. Bäumle, M. Geerkens, I. Heim, C. Osemann, T. Sawitowski, Chem. Soc. Rev. 28 (1999) 179.

[137] U. Heiz, W.D. Schneider, Crit. Rev. Solid State Mat. Sci. 26 (2001) 251.

[138] G. Renaud, Surf. Sci. Rep. 32 (1998) 1.

[139] A.D. Becke, Phys. Rev. A 38 (1988) 3098.

[140] C. Lee, W. Yang, R.G. Parr, Phys. Rev. B 37 (1988) 785.

[141] B. Miehlich, A. Savin, H. Stoll, H. Preuss, Chem. Phys. Lett. 157 (1989) 200.

[142] N. López, F. Illas, J. Phys. Chem. B 102 (1998) 1430.

[143] N. López, F. Illas, N. Rösch, G. Pacchioni, J. Chem. Phys. 110 (1999) 4873.

[144] S. Abbet, E. Riedo, H. Brune, U. Heiz, A.M. Ferrari, L. Giordano, G. Pacchioni, J. Am. Chem. Soc. 123 (2001) 6172.

[145] N. López, J.C. Paniagua, F. Illas, J. Chem. Phys. 117 (2002) 9445.

[146] A. Markovits, M.K. Skalli, C. Minot, G. Pacchioni, N. López, F. Illas, J. Chem. Phys. 115 (2001) 8172.

[147] V. Musolino, A. Selloni, R. Car, Surf. Sci. 402-404 (1998) 413.

[148] A. Bogicevic, D.R. Jennison, Surf. Sci. 515 (2002) L481.

[149] I.V. Yudanov, V.A. Nasluzov, K.M. Neyman, N. Rösch, Int. J. Quantum Chem. 65 (1997) 975.

[150] B.I. Dunlap, N. Rösch, Adv. Quantum Chem. 21 (1990) 317.

[151] T. Belling, T. Grauschopf, S. Krüger, M. Mayer, F. Nörtemann, M. Staufer, C. Zenger, N. Rösch, High Performance Scientific and Engineering Computing, Lecture Notes in Computational Science and Engineering, Vol. 8; H.-J. Bungartz, F. Durst, C. Zenger (Eds.); Springer: Heidelberg, 1999.

[152] T. Belling, T. Grauschopf, S. Krüger, F. Nörtemann, M. Staufer, M. Mayer, V.A. Nasluzov, U. Birkenheuer, A. Hu, A.V. Matveev, A.M. Shor, M.S.K. Fuchs-Rohr, K.M. Neyman, D.I. Ganyushin, T. Kerdcharoen, A. Woiterski, A.B. Gordienko, S. Majumder, N. Rösch, ParaGauss, Version 3.0, Technische Universität München, 2004.

[153] J.P. Perdew, Phys. Rev. B 33 (1986) 8822; Phys. Rev. B 34 (1986) 7406.

[154] B. Hammer, L.B. Hansen, J.K. Nørskov, Phys. Rev. B 59 (1999) 7413.

[155] N. Rösch, S. Krüger, M. Mayer, V.A. Naslusov, Recent Developments and Applications of Modern Density Functional Theory, J. Seminario (Eds.); Elsevier: Amsterdam, 1996.

[156] N. Rösch, A. Matveev, V.A. Nasluzov, K.M. Neyman, L. Moskaleva, S. Krüger, Relativistic Electronic Structure Theory. Part II: Applications, Theoretical and Computational Chemistry Series, Vol. 14; P. Schwerdtfeger (Eds.); Elsevier: Amsterdam, 2004.

[157] D.R. Hamann, Phys. Rev. B 40 (1989) 2980.

[158] C.R.A. Catlow, W.C. Mackrodt, Computer Simulation of Solids, Lecture Notes in Physics, Vol. 166; C.R.A. Catlow, W.C. Mackrodt (Eds.); Springer: Berlin, 1982.

[159] S.F. Boys, F. Bernardi, Mol. Phys. 19 (1970) 553.

[160] C.E. Moore, Atomic Energy Levels; U.S. Natl. Bur. Stand. Circ. No. 467; Government Printing Office: Washington, DC, 1952.

[161] R.G. Parr, W.Yang, Density Functional Theory for Atoms and Molecules, Oxford University: Oxford, 1989.

[162] J.P. Perdew, J.A. Chevary, S.H. Vosko, K.A. Jackson, M.R. Pederson, D.J. Singh, C. Fiolhais, Phys. Rev. B 46 (1992) 6671.

[163] V.V. Rivanenkov, V.A. Nasluzov, A.M. Shor, K.M. Neyman, N. Rösch, Surf. Sci. 525 (2003) 173.

[164] L.E. Chirlian, M.M. Francl, J. Comp. Chem. 8 (1987) 894.

[165] As mentioned in Section 3.1.3, the adsorption energy for the complex Co/MgO was calculated with respect to the atomic energy of the DF ground state configuration d^8s^1 computed to be 0.63 eV more stable than the experimental ground state configuration d^7s^2. Using the latter experimental atomic configuration as reference would result in a binding energy of 1.85 eV for a Co adatom; this value is in the range of the binding energies for the "neighboring" Ni/MgO and Fe/MgO systems. See also the discussion elsewhere on the reliability of DF atomic references [145,146].

[166] A.M. Ferrari, L. Giordano, N. Rösch, U. Heiz, S. Abbet, A. Sanchez, G. Pacchioni, J. Phys. Chem. B 104 (2000) 10612.

[167] L. Giordano, J. Goniakowski, G. Pacchioni, Phys. Rev. B 64 (2001) 75417.

[168] L. Giordano, A. Del Vitto, G. Pacchioni, A.M. Ferrari, Surf. Sci. 540 (2003) 63.

[169] P. Fuentealba, L.V. Szentpaly, M. Preuss, M. Stoll, J. Phys. B 18 (1985) 1287.

[170] B.H. Besler, K.M. Merz, P.A. Kollman, J. Comp. Chem. 11 (1990) 431.

[171] J.E. Sansonetti, W.C. Martin, S.L. Young, Handbook of Basic Atomic Spectroscopic Data; National Institute of Standards and Technology: Gaithersburg, MD, 2004; Online version 1.1 (http://physics.nist.gov/Handbook).

[172] G. Pacchioni, N. Rösch, Acc. Chem. Res. 28 (1995) 390.

[173] S.-C. Chung, S. Krüger, S.Ph. Ruzankin, G. Pacchioni, N. Rösch, Chem. Phys. Lett. 248 (1996) 109.

[174] J.E. Huheey, E.A. Keiter, R.L. Keiter, Inorganic Chemistry: Principles of Structure and Reactivity, 4th ed., HarperCollins: New York, 1993.

[175] A.D. Becke, J. Chem. Phys. 98 (1993) 5648.

[176] S. Lee, C. Fan, T. Wu, S.L. Anderson, Surf. Sci. 578 (2005) 5.

[177] U. Diebold, Surf. Sci. Rep. 48 (2003) 53.

[178] P.S. Bagus, K. Hermann, C.W. Bauschlicher Jr., J. Chem. Phys. 80 (1984) 4378.

[179] K.M. Neyman, S.Ph. Ruzankin, N. Rösch, Chem. Phys. Lett. 246 (1995) 546.

[180] G. Pacchioni, P. Pescarmona, Surf. Sci. 412 (1998) 657.

[181] For instance, see Ref. 168 and references therein.

[182] M. Bowker, Nature Mater. 1 (2002) 205.

[183] H.-J. Freund, Angew. Chem. Int. Ed. 36 (1997) 452.

[184] C.H. Bartholomew, Appl. Catal. A 212 (2001) 17.

[185] O.D. Häberlen, N. Rösch, Chem. Phys. Lett. 199 (1992) 491.

[186] M.D. Morse, Chem. Rev. 86 (1986) 1049.

[187] B. Simard, P.A. Hackett, A.M. James, P.R.R. Langriedge-Smith, Chem. Phys. Lett. 186 (1991) 415.

[188] H.G. Krämer, V. Beutel, K. Weyers, W. Demtröder, Chem. Phys. Lett. 193 (1992) 331.

[189] A. Görling, S.B. Trickey, P. Gisdakis, N. Rösch, Topics in Organometallic Chemistry, Vol. 4; J. Brown, P. Hofmann (Eds.); Springer: Heidelberg, 1999.

[190] S.P. Walch, B.C. Laskowski, J. Chem. Phys. 84 (1986) 2734.

[191] P. Calaminici, A.M. Köster, N. Russo, D.R. Salahub, J. Chem. Phys. 105 (1996) 9546.

[192] V. Bonačić-Koutecký, L. Češpiva, P. Fantucci, J. Koutecký, J. Chem. Phys. 98 (1993) 7981.

[193] H.M. Lee, M. Ge, B.R. Sahu, P. Tarakeshwar, K.S. Kim, J. Phys. Chem. B 107 (2003) 9994.

[194] J. Wang, G. Wang, J. Zhao, Phys. Rev. B 66 (2002) 035418.

[195] H. Häkkinen, U. Landman, Phys. Rev. B 62 (2000) R2287.

[196] W. Weltner Jr., R.J. Van Zee, Annu. Rev. Phys. Chem. 35 (1984) 291.

[197] V. Bonačić-Koutecký, J. Pittner, M. Boiron, P. Fantucci, J. Chem. Phys. 110 (1999) 3867.

[198] H. Häkkinen, B. Yoon, U. Landman, X. Li, H.-J. Zhai, L.-S. Wang, J. Chem. Phys. A 107 (2003) 6168.

[199] V. Bonačić-Koutecký, J. Burda, R. Mitrić, M. Ge, G. Zampella, P. Fantucci, J. Chem. Phys. 117 (2002) 3120.

[200] K.A. Jackson, Phys. Rev. B 47 (1993) 9715.

[201] A.V. Matveev, K.M. Neyman, G. Pacchioni, N. Rösch, Chem. Phys. Lett. 299 (1999) 603.

[202] R.P. Holroyd, M. Bowker, Surf. Sci. 377 (1997) 786.

[203] T. Dellwig, G. Rupprechter, H.-J. Freund, Phys. Rev. Lett. 85 (2000) 776.

[204] M. Frank, M. Bäumer, Phys. Chem. Chem. Phys. 2 (2000) 3723.

[205] J. Libuda, I. Meusel, J. Hoffmann, J. Hartmann, L. Piccolo, C.R. Henry, H.-J. Freund, J. Chem. Phys. 114 (2001) 4669.

[206] I.V. Yudanov, K.M. Neyman, N. Rösch, Phys. Chem. Chem. Phys. 6 (2004) 116.

[207] S.H. Vosko, L. Wilk, M. Nusair, Can. J. Phys. 58 (1980) 1200.

[208] L. Fan and T. Ziegler, J. Chem. Phys. 94 (1991) 6057.

[209] S. Huzinaga, J. Chem. Phys. 66 (1977) 4245.

[210] P.-O. Widmark, P.-A. Malmqvist, B.O. Roos, Theor. Chim. Acta, 77 (1990) 291.

[211] P. Nava, M. Sierka, R. Ahlrichs, Phys. Chem. Chem. Phys. 5 (2003) 3372.

[212] CRC Handbook of Chemistry and Physics, 77th Edition, D.R. Lide, (Eds.); CRC Press: Boca Raton, 1996.

[213] V.A. Nasluzov, N. Rösch, Chem. Phys. 210 (1996) 413.

[214] F. Nörtemann, Dissertation, Technische Universität München, 1998.

[215] T. Ziegler, Chem. Rev. 91 (1991) 651.

[216] S. Krüger, S. Vent, N. Rösch, Ber. Bunsenges. Phys. Chemie 101 (1997) 1640.

[217] S. Krüger, S. Vent, F. Nörtemann, M. Staufer, N. Rösch, J. Chem. Phys. 115 (2001) 2082.

[218] Cluster Models for Surface and Bulk Phenomena; G. Pacchioni, P.S. Bagus, F. Parmigiani, (Eds.); NATO ASI Series B, Vol. 283; Plenum: New York, 1992.

[219] J.L. Whitten, H. Yang, Surf. Sci. Rep. 24 (1996) 59.

[220] A.V. Matveev, M. Staufer, M. Mayer, N. Rösch, Int. J. Quantum Chem. 75 (1999) 863.

[221] R.A. Olsen, P.H.T. Philipsen, E.J. Baerends, J. Chem. Phys. 119 (2003) 4522.

[222] K. H. Lim, N. Rösch, unpublished. Single-point VASP calculations of C atoms on the threefold hollow fcc and hcp sites of a 4-layer Pd(111) slab at r(Pd–C) = 185.5 pm with all substrate atoms kept at experimental truncated-bulk geometry positions, determined by the nearest-neighbor Pd–Pd distance of 275 pm. For computational details, see Ref. 223.

[223] Z.X. Chen, K.M. Neyman, K.H. Lim, N. Rösch, Langmuir, 20 (2004) 8068.

[224] K.H. Lim, K.M. Neyman, N. Rösch, to be published.

[225] K.M. Neyman, C. Inntam, N. Rösch, to be published.

[226] N. Krishnankutty, M.A. Vannice, J. Catal. 155 (1995) 312.

[227] M.K. Rose, A. Borg, T. Mitsui, D.F. Ogletree, M. Salmeron, J. Chem. Phys. 115 (2001) 10927.

[228] K.M. Neyman, N. Rösch, Ber. Bunsenges. Phys. Chem. 96 (1992) 1711.

[229] J.M. Ogden, Annu. Rev. Energy Environ. 24 (1999) 227.

[230] D.L. Trimm, Z.L. Önsan, Catal. Rev. 43 (2001) 31.

[231] N. Iwasa, S. Kudo, H. Takahshi, S. Masuda, N. Takezawa, Catal. Lett. 19 (1993) 211.

[232] N. Takezawa, N. Iwasa, Catal. Today 36 (1997) 45.

[233] M.L. Cubeiro, J.L.G. Fierro, J. Catal. 179 (1998) 150.

[234] J.A. Rodriguez, J. Phys. Chem. 98 (1994) 5758.

[235] J.A. Rodriguez, M. Kuhn, J. Phys. Chem. 100 (1996) 381.

[236] Z. Chen, K.M. Neyman, A.B. Gordienko, N. Rösch, Phys. Rev. B 68 (2003) 075417.

[237] Z. Chen, K.M. Neyman, N. Rösch, Surf. Sci. 548 (2004) 291.

[238] O.D. Häberlen, N. Rösch, Chem. Phys. Lett. 199 (1992) 491.

[239] N. Iwasa, N. Ogawa, S. Masuda, N. Takezawa, Bull. Chem. Soc. Jap. 71 (1998) 1451.

[240] M. Hansen, Constitution of Binary Alloys, 2nd ed., McGraw Hill: New York, 1958.

[241] A.M. Bradshaw, F.M. Hoffmann, Surf. Sci. 72 (1978) 513.

[242] X. Guo, J.T. Yates Jr., J. Chem. Phys. 90 (1989) 6761.

[243] D. Loffreda, D. Simon, P. Sautet, Surf. Sci. 1999 (68) 425.

[244] N. López, J.K. Nørskov, Surf. Sci. 477 (2001) 59.

[245] A.I. Boldyrev, J. Simons, Periodic Tables of Diatomic Molecules, Wiley: Chichester, 1997.

[246] Periodensystem der Elemente, VCH: Weinheim, 1995.

[247] L.E. Chirlian, M.M. Francl, J. Comp. Chem. 8 (1987) 894.

[248] K.P. Huber, G. Herzberg, Molecular Spectra and Molecular Structure. Constants of Diatomic Molecules; Vol. IV; Reinhold: New York, 1979.

[249] A. Föhlisch, M. Nyberg, P. Bennich, L. Triguero, J. Hasselström, O. Karis, L.G. Pettersson, A. Nilsson, J. Chem. Phys. 112 (2000) 1946.

[250] a) K.M. Neyman, N. Rösch, K.L. Kostov, P. Jakob, D. Menzel, J. Chem. Phys. 100 (1994) 2310; b) K.M. Neyman, N. Rösch; Surf. Sci. 307 (1994) 1193; c) M. Staufer, K.M. Neyman, P. Jakob, V.A. Nasluzov, D. Menzel, N. Rösch, Surf. Sci. 369 (1996) 300; d) K.M. Neyman, M. Staufer, V.A. Nasluzov, N. Rösch, J. Mol. Cat. 119 (1997) 245.

[251] B.E. Nieuwenhuys, Surf. Rev. Lett. 3 (1996) 1869.